



ANALYSIS OF NON-UNIFORM GAIN FOR CONTROL OF A DEFORMABLE MIRROR  
IN AN ADAPTIVE-OPTICS SYSTEM

THESIS

Kevin P. Vitayaudom, Second Lieutenant, USAF

AFIT/GE/ENG/08-35

DEPARTMENT OF THE AIR FORCE  
AIR UNIVERSITY

**AIR FORCE INSTITUTE OF TECHNOLOGY**

Wright-Patterson Air Force Base, Ohio

APPROVED FOR PUBLIC RELEASE; DISTRIBUTION UNLIMITED.

The views expressed in this thesis are those of the author and do not reflect the official policy or position of the United States Air Force, Department of Defense, or United States Government.

AFIT/GE/ENG/08-35

ANALYSIS OF NON-UNIFORM GAIN FOR CONTROL OF A  
DEFORMABLE MIRROR  
IN AN ADAPTIVE-OPTICS SYSTEM

THESIS

Presented to the Faculty  
Department of Electrical and Computer Engineering  
Graduate School of Engineering and Management  
Air Force Institute of Technology  
Air University  
Air Education and Training Command  
In Partial Fulfillment of the Requirements for the  
Degree of Master of Science in Electrical Engineering

Kevin P. Vitayaudom, B.S.E.E.  
Second Lieutenant, USAF

March 2008

APPROVED FOR PUBLIC RELEASE; DISTRIBUTION UNLIMITED.

ANALYSIS OF NON-UNIFORM GAIN FOR CONTROL OF A  
DEFORMABLE MIRROR  
IN AN ADAPTIVE-OPTICS SYSTEM

Kevin P. Vitayaudom, B.S.E.E.  
Second Lieutenant, USAF

Approved:

/signed/	27 Mar 2008
_____ Capt Jason D. Schmidt, PhD (Chairman)	_____ date
/signed/	27 Mar 2008
_____ Dr. Juan R. Vasquez (Member)	_____ date
/signed/	27 Mar 2008
_____ Maj Michael J. Veth, PhD (Member)	_____ date

*Abstract*

The Air Force Research Laboratory's Sodium Guidestar Adaptive Optics for Space Situational Awareness program (NGAS) has sponsored research on spatially non-uniform gain for the servo-loop controller of an adaptive optics (AO) system. The edge subapertures of a Shack-Hartmann wavefront sensor have lower signal-to-noise ratios and are more susceptible to measurement errors than fully illuminated center subapertures. These measurement errors produce errant commands over the corresponding edge actuators and can induce instabilities over these regions in strong turbulence conditions. The objective of this research was to develop and experimentally verify the use of spatially varying gain maps on the servo-loop controller of a deformable mirror for improvements in the performance of an adaptive optics system and the mitigation of instabilities that can occur over the edge actuators of a deformable mirror. Spatially varying gain maps were developed to compensate for edge effects by having lower filter gains  $b$  designated for the edge subapertures. This lowered the bandwidth over the edge actuators which are the most susceptible to the edge effects. A gain map with a ring of lower filter gains  $b$  over just the outer actuators was experimentally shown to increase the overall Strehl ratio of the AO system in all of the tested turbulence conditions. Specifically, the non-uniform gain maps provide the largest increase of Strehl ratio over the AO system in low signal-to-noise ratio and high turbulent scenarios. Experiments were also conducted in regimes where instabilities formed over the edge actuators of the deformable mirror. Gaussian gain maps are shown to significantly reduce the overall residual phase variance over the edge actuators thereby reducing the formation of the instabilities.

## *Acknowledgements*

I would like to express my sincere gratitude to my advisor, Capt Jason Schmidt who not only guided me academically, but taught me a great deal about professionalism as an officer. His detailed explanations of some of my most random questions and patience with me during every meeting as I spent an inordinate amount of time looking through my disorganized piles of papers gives me an excellent model to aspire towards. I would also like to thank my thesis committee members, Lt Col Juan Vasquez, ret. and Maj Michael Veth, for spending time out of their busy schedules to provide insights into control theory for this thesis. Additionally, I would like to give a special thanks to the people in the ASALT lab, Lt Tony Vincent, Dr. Darryl Sanchez, Dr. Denis Oesch, Mala Mateen, and Chip Beckner. Without them, none of the experiments for this thesis would have been possible. And finally I would like to thank my family who have always been supportive of me throughout my life and drive me to do the best I can in whatever I do.

Kevin P. Vitayaudom

# Table of Contents

	Page
Abstract . . . . .	iv
Acknowledgements . . . . .	v
List of Figures . . . . .	ix
List of Tables . . . . .	xi
List of Abbreviations . . . . .	xii
I. Introduction . . . . .	1
1.1 Problem Statement . . . . .	2
1.2 Detailed Research Goals . . . . .	2
1.3 Thesis Overview . . . . .	3
II. Background and Related Research . . . . .	5
2.1 Atmospheric Distortion of Light . . . . .	5
2.1.1 Atmospheric Turbulence . . . . .	6
2.1.2 Atmospheric Condition Characterizations . . . . .	8
2.2 Conventional Adaptive Optics . . . . .	9
2.2.1 Starfire Optical Range 3.5-meter Telescope . . . . .	11
2.2.2 AO Metrics of Performance . . . . .	13
2.3 Deformable Mirror . . . . .	15
2.3.1 Influence Function . . . . .	17
2.4 Shack-Hartmann Wavefront Sensor . . . . .	17
2.4.1 Energy Imbalance Equation . . . . .	19
2.4.2 Shack-Hartmann WFS Measurement Errors . . . . .	20
2.5 Reconstruction of Phase . . . . .	26
2.5.1 Fried Geometry . . . . .	26
2.5.2 Least-Squares Estimation . . . . .	28
2.6 Servo-Controller . . . . .	29
2.6.1 Digital Filter Model . . . . .	29
2.6.2 Rejection Functions . . . . .	31
2.7 Stability . . . . .	34
2.7.1 Lyapunov Stability . . . . .	34
2.7.2 Slaving Considerations . . . . .	36
2.7.3 Waffle Mode . . . . .	37

	Page
III. ASALT Laboratory Setup and Experiment Methodology . . . . .	39
3.1 ASALT Laboratory . . . . .	39
3.1.1 Laboratory Overview . . . . .	39
3.1.2 Unique Components . . . . .	40
3.1.3 ASALT Initialization and Calibration . . . . .	45
3.1.4 Control Console Layout . . . . .	45
3.1.5 Primary AO Experimental Layout . . . . .	46
3.2 Lyapunov Stability Bounds . . . . .	48
3.2.1 Production of Reconstructor and Geometry Matrix . . . . .	49
3.2.2 Filter Gain Bounds . . . . .	50
3.3 Slope Measurement Sensitivity Experiment . . . . .	50
3.3.1 Motivation . . . . .	50
3.3.2 Slope Measurement Experiment Design . . . . .	51
3.4 Analysis of Slaving Effects Experiment . . . . .	53
3.4.1 Motivation . . . . .	53
3.4.2 Slaving Experiment Design . . . . .	53
3.5 Non-Uniform Gain Experiment . . . . .	55
3.5.1 Motivation . . . . .	55
3.5.2 Gain Map Design and Turbulence Conditions . . . . .	55
3.5.3 NUGE Experiment Design . . . . .	61
3.5.4 Low SNR Experiment Design . . . . .	63
IV. Results and Data Analysis . . . . .	66
4.1 SH WFS Slope Measurement Sensitivity Results and Analysis . . . . .	66
4.1.1 Summary of the SH WFS measurement experiment . . . . .	68
4.2 Slaving vs Non-Slaving Results and Analysis . . . . .	71
4.2.1 Summary of the Slaving vs. Non-slaving experiment . . . . .	72
4.3 NUGE Results and Analysis . . . . .	73
4.3.1 Spatially Varying Gain Maps . . . . .	75
4.3.2 Low SNR . . . . .	79
4.3.3 Mitigation of Instabilities . . . . .	81
4.3.4 Summary of Spatial Varying Gain Maps . . . . .	86
V. Conclusions . . . . .	87
5.1 Summary . . . . .	87
5.2 Key Results . . . . .	88
5.3 Recommendations . . . . .	89



	Page
Appendix A. Matlab Code . . . . .	91
A.1 Hdf5 reader code . . . . .	91
A.2 Strehl ratio code . . . . .	97
A.3 Error rejection function code . . . . .	103
A.4 Lyapunov stability code . . . . .	107
A.5 NUGE DM Filter . . . . .	108
A.6 NUGE DM Filter AMC code . . . . .	111
Bibliography . . . . .	114
Vita . . . . .	116

*List of Figures*

Figure		Page
2.1.	Wavefront distortion due to turbulence. . . . .	5
2.2.	Basic AO diagram. . . . .	10
2.3.	SOR 3.5 meter telescope. . . . .	12
2.4.	Segmented and continuous DMs. . . . .	16
2.5.	One-dimensional depiction of SH WFS Sensor. . . . .	18
2.6.	$24 \times 24$ SH WFS subapertures. . . . .	19
2.7.	Quad cell and slope measurements. . . . .	20
2.8.	Focal spots over SH WFS with on-axis reference beam. . . . .	22
2.9.	Asymmetrical centroid slope measurements. . . . .	24
2.10.	Partially illuminated edge subapertures. . . . .	25
2.11.	Reconstructed phase from gradient measurements. . . . .	26
2.12.	Fried geometry. . . . .	27
2.13.	Example of atmospheric and noise PSD. . . . .	33
2.14.	Example of ERF and NRF. . . . .	33
2.15.	Direct and linearly extrapolated slaving. . . . .	37
2.16.	Waffle mode over a DM. . . . .	38
3.1.	ASALT laboratory's optical table layout in SRI-2. . . . .	41
3.2.	ASALT laboratory DM. . . . .	42
3.3.	ATS phase wheels. . . . .	43
3.4.	ASALT laboratory control computers. . . . .	44
3.5.	ASALT layout and control system data display. . . . .	46
3.6.	Primary layout. . . . .	47
3.7.	AOTools subaperture dialog. . . . .	49
3.8.	Error propagator. . . . .	50
3.9.	SH WFS measurement layout. . . . .	51

Figure		Page
3.10.	Example of frequency response of $F(z)$ . . . . .	57
3.11.	SNR over a SH WFS detector array. . . . .	58
3.12.	Non-uniform gain maps. . . . .	59
3.13.	NUGE control software layout. . . . .	62
3.14.	Laser attenuator. . . . .	64
4.1.	Center vs. middle $x$ -gradient response. . . . .	68
4.2.	Center vs. middle $y$ -gradient response. . . . .	69
4.3.	Center vs. edge $x$ -gradient response. . . . .	69
4.4.	Center vs. edge $y$ -gradient response. . . . .	70
4.5.	Slaving vs. non-slaving AO system performance comparison. . .	71
4.6.	All turbulence conditions AO system performance comparison.	74
4.7.	Gain Map 1 Strehl ratio improvement, Turb 1. . . . .	76
4.8.	Gain Map 1 Strehl ratio improvement, Turb 2. . . . .	76
4.9.	Gain Map 1 Strehl ratio improvement, Turb 3. . . . .	77
4.10.	ERF comparison of uniform gain and gain map 1, Turb 3. . . .	78
4.11.	Low SNR and high SNR AO performance comparison, Turb 2.	79
4.12.	Low SNR and high SNR plot over subapertures. . . . .	80
4.13.	Low SNR Strehl ratio, Turb 1. . . . .	81
4.14.	Residual phase variance taken in open loop, Turb 3. . . . .	82
4.15.	Residual phase variance taken in closed loop with uniform gain, Turb 3. . . . .	83
4.16.	Residual phase variance taken in closed loop with gain map 3, Turb 3. . . . .	83
4.17.	Interferograms of DM waffle mode mitigation. . . . .	84
4.18.	Aperture averaged residual phase variance taken in closed loop, Turb 3 . . . . .	84
4.19.	Spatial regions. . . . .	85
4.20.	Spatial regions AO system performance comparison, Turb 3. . .	85

*List of Tables*

Table		Page
3.1.	SMSE system parameters. . . . .	52
3.2.	SM oscillator component parameters. . . . .	53
3.3.	ASEE system parameters. . . . .	54
3.4.	ASEE turbulence condition. . . . .	55
3.5.	Table of slaving experiments. . . . .	55
3.6.	NUGE turbulence conditions. . . . .	61
3.7.	Table of baseline uniform gain experiments. . . . .	62
3.8.	NUGE system parameters. . . . .	63
3.9.	Table of NUGE experiments. . . . .	63
3.10.	Low SNR system parameters. . . . .	65
3.11.	Table of low SNR experiments. . . . .	65
4.1.	SH WFS slope measurement results. . . . .	70
4.2.	Slaving vs. non-slaving filter gains with the least residual phase variance. . . . .	72
4.3.	Baseline uniform gain results. . . . .	74
4.4.	Baseline uniform gain versus NUGE Strehl results. . . . .	77

## *List of Abbreviations*

Abbreviation		Page
AO	adaptive optics . . . . .	1
NGAS	Sodium Guidestar AO for Space Situational Awareness . .	1
SOR	Starfire Optical Range . . . . .	1
DM	deformable mirror . . . . .	1
WFS	wavefront sensor . . . . .	1
LS	least-squares . . . . .	1
SH	Shack-Hartmann . . . . .	2
ERF	error rejection function . . . . .	3
ASALT	Atmospheric Simulation and AO Laboratory Testbed . . .	3
PSD	power spectral density . . . . .	7
SM	steering mirror . . . . .	11
LGS	laser guidestar . . . . .	11
<i>SR</i>	Strehl ratio . . . . .	15
PSF	point spread function . . . . .	15
PDF	probability density function . . . . .	21
SNR	signal-to-noise ratio . . . . .	24
SISO	single-input single-output . . . . .	29
PID	proportional-integral-derivative . . . . .	31
NRF	noise rejection function . . . . .	32
WCE	Wavefront Control Experiment . . . . .	38
SMST	Slope Measurement Sensitivity Test . . . . .	39
ASEE	Analysis of Slaving Effects Experiment . . . . .	39
API	application programming interface . . . . .	39
ATS	atmospheric turbulence simulator . . . . .	40
SRI	self-referencing interferometer . . . . .	40

Abbreviation		Page
RTR	real-time reconstructor . . . . .	45
GUI	graphical user interface . . . . .	45
HDF	hierarchical data format . . . . .	46
NUGE	Non-Uniform Gain Experiment . . . . .	55

ANALYSIS OF NON-UNIFORM GAIN FOR CONTROL OF A  
DEFORMABLE MIRROR  
IN AN ADAPTIVE-OPTICS SYSTEM

## I. Introduction

The Air Force Research Laboratory's Sodium Guidestar Adaptive Optics (AO) for Space Situational Awareness (NGAS) program at the Starfire Optical Range (SOR) at Kirtland Air Force Base has sponsored research on spatially non-uniform gain for the servo-loop controller of an AO system. A conventional AO system controls a deformable mirror (DM) which adjusts its surface in order to correct for high-order phase variations found in an aberrated wavefront. The DM's surface is dynamically reshaped by individual actuators that are controlled by a servo-loop controller which produces its commands from the residual phase that is sensed from the wavefront sensor (WFS). Current servo-loop controllers use the same filter gains over all of the actuators, thereby enacting the same control authority over the entire surface of the DM. Observations at the SOR's 3.5 meter telescope have found that in some situations instabilities begin to form over the DM, beginning along the edge actuators. If not mitigated, the instabilities that form over the edges of the DM can spread over the entire surface. The edge instabilities can be attributed to slaving effects over the DM, explained in Section 2.7.2, and low illumination levels over the edges of the WFS, which in turn produce commands to the edge actuators which are more sensitive to noise and prone to errors. Adjusting the filter gains to change the bandwidth over these specific regions can be applied using spatially varying gain maps on the DM filter. Also using the weighted least-squares (LS) technique in the reconstructor matrix can give due consideration to the edge effects. Yet, adjusting the reconstructor in real time is much more computationally complex as compared to adjusting the filter gains in the DM filter. The low computational complexity of adjusting the filter

gains is a primary reason this approach is being explored. Therefore, this research is concentrating on using spatially varying gain maps.

### ***1.1 Problem Statement***

The objectives of this research are to produce and study spatially varying gain maps in the servo-loop controller of an AO system in order to apply a lower bandwidth to the commands of the edge actuators. This mitigates noise and measurement error effects that are found to occur over the edge subapertures and edge actuators of the Shack-Hartmann (SH) WFS and DM, respectively. Experiments have been conducted with varied DM controller parameters over different turbulence conditions and illumination levels to examine and compare the performance and instability mitigation of the AO system using spatially varying gain maps.

### ***1.2 Detailed Research Goals***

This research has explored the edge effects of the SH WFS and DM that cause performance degradation and instabilities in conventional AO systems. Spatially varying gain maps over the servo-loop controller are used to mitigate these effects. More specifically, the specific goals of this research are:

- to determine the differences in the gradient measurements of a SH WFS between its center and edge subapertures,
- to compare the performance of an AO system with and without slaving the edge actuators,
- to develop non-uniform gain maps that address the edge effects of the WFS and DM,
- to experimentally show performance improvement of an AO system using non-uniform gain maps with the servo-loop controller under different turbulence conditions and illumination levels,



- and to experimentally show that non-uniform gain maps with the servo-loop controller can mitigate instabilities that occur along the edges of the DM.

Each of the goals were achieved with definitive results. The analysis from this research shows that the application of spatially varying gain to the servo-loop controller can improve the performance of a conventional AO system without added computational complexity and can be used to mitigate instabilities that form along the edges of the DM.

### ***1.3 Thesis Overview***

Chapter II gives an overview of atmospheric turbulence, conventional AO, a detailed discussion of each individual component in the AO system, and an overview of control theory, particularly error rejection functions (ERF). Atmospheric turbulence is described with specific emphasis on how it distorts a wavefront and the metrics that are used to characterize its strength. The section on conventional AO discusses how a DM uses the principle of phase conjugation to compensate for turbulence along with a brief discussion of the AO system on the SOR's 3.5 meter telescope. Each primary component of the AO system is then described with its function and contribution to edge effects. Lastly, the AO system is discussed in terms of control theory and how ERFs are used to define over what frequencies the system is rejecting turbulence.

Chapter III presents the setup and methodology of the experiments conducted in the Atmospheric Simulation and AO Laboratory Testbed (ASALT) at the SOR. A description of the equipment and the setup of the apparatus is given with a particular emphasis on how the layouts are used in a control console to configure each experiment. Then the experiments exploring the edge effects of the SH WFS and DM are presented. The development of the spatially varying gain maps and experiments used to mitigate the edge effects is then described. Lastly, the varied controller parameters, turbulence conditions, and illumination levels are discussed for each experiment using the non-uniform gain maps.

Chapter IV presents the analysis and results of the data taken from the exper-

iments in Chapter III. The results of each experiment are represented through plots using characteristics of residual phase variance, Strehl ratio, and ERFs. Using these plots, improvements in the performance of the AO system and mitigation of instabilities is shown.

Chapter V contains the final conclusions of the results taken from Chapter IV and discusses the benefits gained from the research. Recommendations for future work are then discussed, addressing further analysis of different gain maps and condition parameters that can be explored.

## II. Background and Related Research

### 2.1 Atmospheric Distortion of Light

Light from distant objects such as stars travels through millions of miles of space unperturbed, yet as it finally reaches us the Earth's turbulent atmosphere distorts the light at the end of its journey causing what many know as the 'twinkling' of the stars. The differential heating and cooling of the Earth caused by sunlight and the diurnal cycle, result in temperature variations that cause large scale inhomogeneities in the temperature of the air. [10] These large scale inhomogeneities naturally break down into smaller inhomogeneities by the movement of air, which causes wind. The random nature of this process causes the turbulent wind motion, forming small pockets of air known as 'eddies.' Each of the eddies act like tiny lenses because the temperature variations alter the index of refraction of the air. [13] Therefore the incoming light from a distant source that is propagating through the atmosphere gets refocused and directed through each of these 'lenses' causing the original wavefront to be distorted, as shown in Figure 2.1.

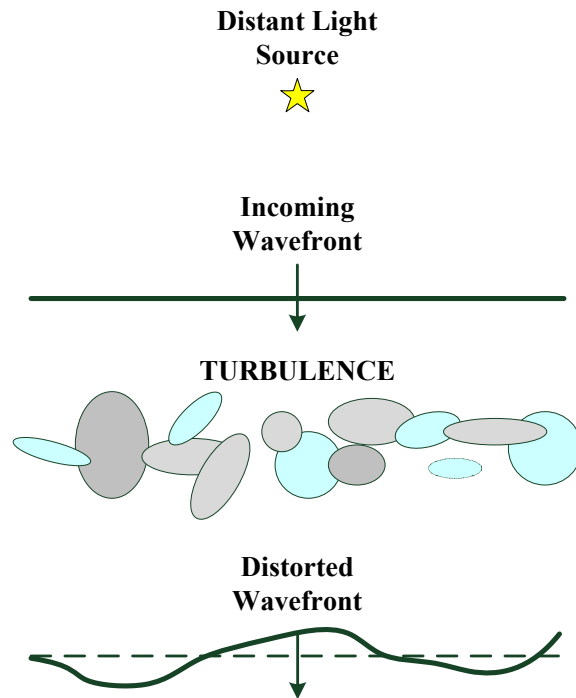


Figure 2.1: Wavefront distortion due to turbulence.

The optical field of the wavefront can be represented with two main components which include amplitude  $A$  and phase  $\varphi$ . [14] The mathematical representation is shown as an electric field  $A \exp(-j\varphi)$ . It should be noted that the phase retains the most amount of information when imaging and is the greatest concern in the AO community when compensating for a disturbance. Therefore, the analysis will not be concerned with the fluctuations in the amplitude component. A two-dimensional incident plane wave with an undisturbed phase can be expressed by  $A \exp(-j\varphi^{ideal})$ . When this plane wave propagates through turbulence the phase becomes distorted. The change in the phase due to the turbulence is represented by an additive phase term  $\varphi^{turb}$  resulting in a outgoing field that has propagated through the atmosphere  $A \exp(-j(\varphi^{ideal} + \varphi^{turb}))$ .

*2.1.1 Atmospheric Turbulence.* The ever-changing movement of the air causes the temporal and spatial fluctuations of the index of refraction in the atmosphere. Because the index of refraction is so sensitive to temperature variations in the atmosphere, the index is random and can be considered to be a stochastic process. The atmosphere's index of refraction  $n(\mathbf{r}, t)$  can be represented as the sum of the mean index of refraction  $n_0$  and a randomly varying portion  $n_1(\mathbf{r}, t)$  [10]

$$n(\mathbf{r}, t) = n_0 + n_1(\mathbf{r}, t), \quad (2.1)$$

where  $\mathbf{r}$  is a three-dimensional position vector, and  $t$  is time.

The fluctuations in the index of refraction depend upon the temperature and pressure, and at visible and infrared wavelengths they are given by [1]

$$n_1(\mathbf{r}, t) = 77.6 \times 10^{-6} (1 + 7.52 \times 10^{-3} \lambda^{-2}) \frac{P(\mathbf{r}, t)}{T(\mathbf{r}, t)}, \quad (2.2)$$

where the temperature of the air  $T$  is in Kelvins, and pressure  $P$  is in millibars. The wavelength  $\lambda$  can be considered to be negligible when working in the optical range. Thus setting  $\lambda \sim 0.5 \mu\text{m}$ ,  $n_1(\mathbf{r}, t)$  can be approximated to get a simplified model given

by

$$n_1(\mathbf{r}, t) = 79 \times 10^{-6} \frac{P(\mathbf{r}, t)}{T(\mathbf{r}, t)}. \quad (2.3)$$

These fluctuations of the index of refraction are mainly due to the changes in the temperature because the pressure fluctuates little. The abundance of eddies that cause these index of refraction fluctuations  $n_1(\mathbf{r})$  can be represented by the spatial power spectral density (PSD), which is denoted by  $\Phi_n(\kappa)$ . The spatial vector wavenumber  $\kappa$  describes the scalar size of the eddies in the orthogonal components composed of  $\kappa_x, \kappa_y$ , and  $\kappa_z$ . The scalar size of the eddies are related to the spatial vector wavenumber by,  $l = 2\pi/\kappa$ . The fluctuations are assumed to be locally homogeneous and spatially isotropic, which means that statistical moments of  $n_1$  are invariant to translation and rotation. [5]

Kolmogorov theory presents a mathematical representation of  $\Phi_n(\kappa)$ , yet is only valid in a particular regime that is determined by the size of the eddies. This regime of turbulence is defined by the inner scale,  $l_0$ , and the outer scale,  $L_0$ . The inner scale represents the size at which the eddies begin to disappear, and the remaining energy left in the fluid motion dissipates as heat. When the eddies are this small, Kolmogorov theory can no longer predict  $\Phi_n(\kappa)$ . The outer scale is the size of the largest eddy at which you can no longer assume it to be homogeneous and isotropic, therefore Kolmogorov theory no longer holds in this regime. Yet Kolmogorov theory can predict the spatial PSD of the index of refraction in the regime where  $2\pi/L_0 \leq \kappa \leq 2\pi/l_0$ , as shown by

$$\Phi_n^K(\kappa) = 0.033C_n^2\kappa^{-11/3}, \quad (2.4)$$

where  $C_n^2$  is the structure parameter of the fluctuations of the index of refraction and is in units of  $\text{m}^{-2/3}$ . This represents the strength of these fluctuations and is actually a function of the altitude  $h$ . This structure parameter varies with the time of the day and geographic location. Therefore, there are different models to represent these specific conditions. The  $C_n^2$  model used in this research is the Hufnagel-Valley

turbulence model as represented by

$$C_n^2(h) = 5.94 \times 10^{-53}(v/27)^2 h^{10} \exp(-h/1000) + 2.7 \times 10^{-16} \exp(-h/1500) + A_g \exp(-h/100), \quad (2.5)$$

where  $v$  represents the high altitude wind speed and  $A_g$  is the strength of the turbulence on the ground. There are other models that can be used to represent the atmosphere, but they are beyond the scope of this research. [1, 10, 13].

*2.1.2 Atmospheric Condition Characterizations.* The AO community uses multiple metrics to describe the conditions of the atmosphere at different sites in the world, such as the Fried parameter and Greenwood frequency described below.

*2.1.2.1 Fried Parameter.* The Fried parameter  $r_0$  is one of the more common metrics used to give the level of turbulence at a particular location. Under turbulence, this parameter defines how large a diameter of a collector can be before the atmosphere seriously limits the performance, given by [14]

$$r_0 = \left[ 0.423 k^2 \sec \zeta \int_{Path} C_n^2(h) dh \right]^{-3/5}, \quad (2.6)$$

where  $k = 2\pi/\lambda$ ,  $\zeta$  is the zenith angle ( $\zeta = 0$  degrees corresponds to viewing directly overhead), and  $C_n^2(h)$  given by Eq. (2.5) is integrated over the path the light takes through the atmosphere. The Fried parameter normally varies from about 5 cm (poor seeing) to 20 cm (good seeing).

*2.1.2.2 Greenwood Frequency.* The Greenwood frequency  $f_G$  is a characteristic temporal correlation frequency of the atmosphere and is used to determine how fast an AO system must operate at in order to adequately reject the turbulence.

Using the flat-Earth assumption, the Greenwood frequency is given by [13]

$$f_G = 2.32\lambda^{-6/5} \left[ \sec \zeta \int_{Path} C_n^2(h) v_W(h)^{5/3} dh \right]^{3/5}, \quad (2.7)$$

where  $v_W$  is the wind speed as a function of the altitude. When Kolmogorov turbulence is used, the residual phase due to finite control bandwidth  $\sigma_{Temp}^2$  of an AO system can be estimated by the closed-loop 3dB bandwidth of the system  $f_{3dB}$  and the Greenwood frequency: [14]

$$\sigma_{Temp}^2 = \left( \frac{f_G}{f_{3dB}} \right)^{5/3}. \quad (2.8)$$

As a rule of thumb,  $f_{3dB}$  should be at least ten times larger than the Greenwood frequency in order to for the system to remain stable and compensate for the turbulence. [14]

## 2.2 Conventional Adaptive Optics

An AO system's primary objective is to sense and compensate for the distortion of a wavefront in real-time. The core principle behind an AO system's capability to correct for a disturbance is phase conjugation. As a wavefront  $A \exp(-j\varphi^{ideal})$  propagates through turbulence its phase gets distorted. The change in phase due to the turbulence is represented as an additive term  $\varphi^{turb}$  which causes the outgoing field to become  $A \exp(-j(\varphi^{ideal} + \varphi^{turb}))$ . An AO system senses the disturbance in the phase  $\varphi^{turb}$  and applies the opposite of the distorted phase  $-\varphi^{turb}$  to the wavefront so that the original field is restored  $A \exp(-j\varphi^{ideal})$ .

The detection and correction of the aberrations in the phase are accomplished through the following main components: WFS(s), tip/tilt mirror(s), DM(s), and controller(s). Figure 2.2 is a simplified diagram of the AO process without the tilt control loop depicted because this research is concentrated on the high-order aberration compensation with the DM. Though the process with a tilt-removal system starts when

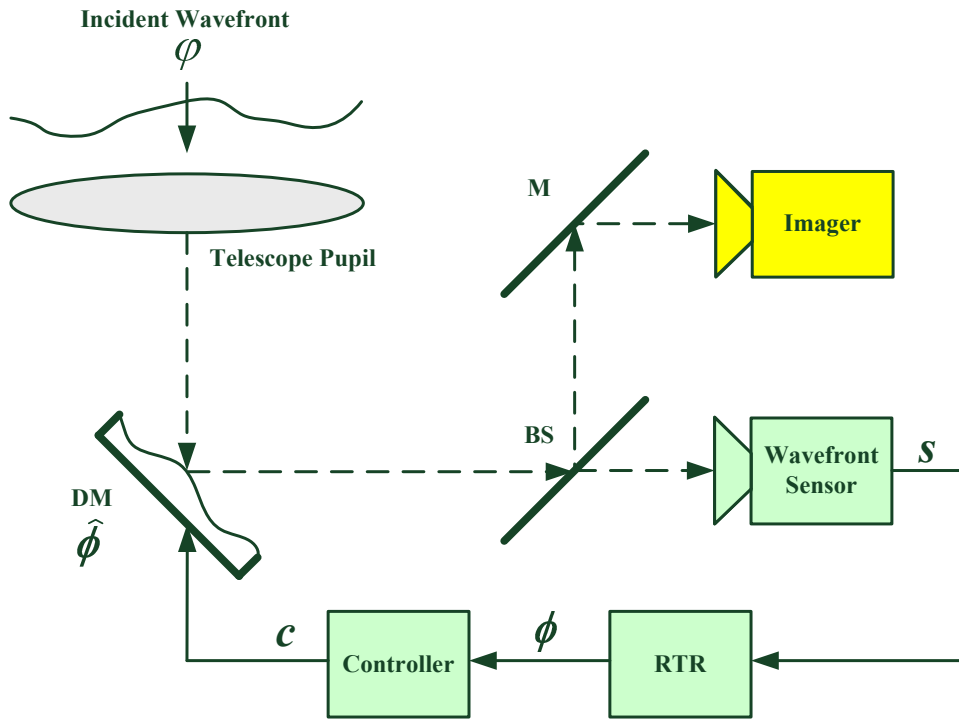


Figure 2.2: Basic AO diagram. The incident wavefront  $\phi$  is collected through the telescope pupil and reflected off the deformable mirror surface whose phase is represented by  $\hat{\phi}$  (assuming tilt-removed phase). The light is then divided with a beamsplitter, with one path going to the imager and the other path going to the WFS. The WFS then senses the relative slope  $s$  which then is processed by the reconstructor to piece together the phase  $\phi$ . The controller then takes the phase measurements and computes commands  $c$  to adjust the deformable mirror surface for phase conjugation of the incident wavefront.



the aberrated light first enters the AO system through a telescope and is then reflected off a steering mirror (SM) which corrects for the tip and tilt aberrations in the phase of the incoming wavefront. The tip and tilt aberrations can account for 87% of the power in the wavefront phase fluctuations. [10] The light is then reflected off the DM's surface which is pushed and pulled by actuators to deform the shape of its surface so that it conjugates the high-order phase of the turbulence. A beamsplitter is then used to separate the light between an imaging system and a WFS. The WFS is used to detect the aberrations in the phase so that the controllers can produce commands to operate the tip and tilt and DM. This whole process must be quick enough to follow the time evolving of the phase errors induced by the turbulence in order to correct for them. [10]

In order to measure the aberrated phase, a reference must be used. Artificial laser guidestars (LGS), natural stars, and reflections from the target are often used as the reference sources. These beacons must be significantly far away so that it can be treated as a point source. An undisturbed point source's phase is relatively flat after travelling a long distance. Though due to the turbulence, the phase is not flat and those aberrations in the phase are how the turbulence is characterized. The beacon must be travelling from nearly the same direction as the target so that the measured phase is highly correlated with the object's phase. Sometimes a natural guide star is unavailable or the target is not illuminated well enough. These cases require a projected artificial laser guidestar within the telescope's field-of-view. The two most common guidestars are the Rayleigh LGS which uses Rayleigh scattering in the stratosphere to produce a point source at about 10-20 kilometers into the atmosphere, and the sodium LGS which produces a beacon by resonant scattering of sodium atoms in the mesosphere at about 90 kilometers.

*2.2.1 Starfire Optical Range 3.5-meter Telescope.* The SOR is operated by the United States Air Force Research Laboratory and is located at Kirtland AFB, New Mexico. This facility has an AO system which utilizes a 3.5-meter telescope

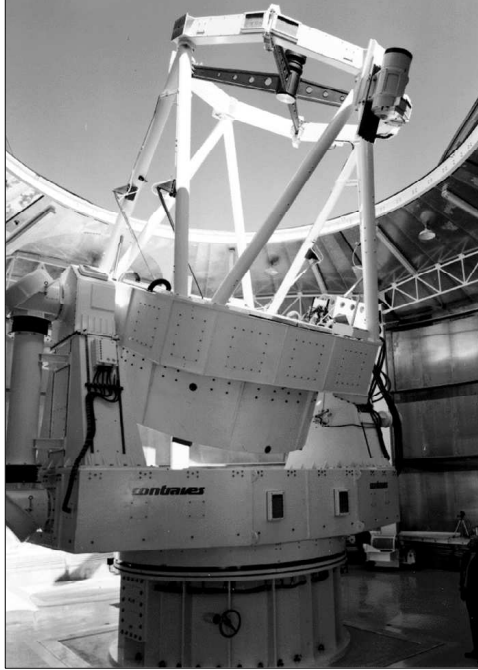


Figure 2.3: SOR 3.5 meter telescope.

with primary missions that include but are not limited to high resolution imaging of space objects and satellite tracking. The SOR was the first site to demonstrate an operational closed-loop AO system utilizing an artificial guidestar.

*2.2.1.1 SOR Brief Description of Components.* The SOR utilizes a 3.5 meter Cassegrain telescope that has a retractable dome which allows the telescope to be completely exposed to the surrounding atmosphere, as shown in Figure 2.3. This is vital for tracking fast slewing targets which require the telescope to move quickly and not be impeded by the massive dome. The system utilizes a DM for high-order wavefront aberrations that conjugate to the telescope pupil and has a diameter of 21 cm with 30 actuators spaced across that length. There are 941 DM actuator locations with 756 of them being actively controlled. For its particular geometry (discussed in Section 2.5.1) there are 684 illuminated subapertures which are spatially defined by a  $2 \times 2$  square configuration of the actuators. A SH WFS is used with a lenslet array in the pupil plane to sense the incident wavefront. Each lenslet focuses light in a portion of the aperture to a focus on a detector array. The spots are magnified so that there

is one spot corresponding to a  $2 \times 2$  region of the array. The energy imbalance is used to compute the average tilt over the subaperture. When sampled together, they form a sampled version of the wavefront. [12]

*2.2.1.2 SOR Control System.* The SOR's AO control system requires an extensive amount of computational power to process all of the necessary DM commands. The wavefront reconstructor alone processes 2048 gradient measurements from the WFS per frame, which is composed of eight engine modules. These modules each have 128 digital signal processors which are assigned to individual DM actuators and auxiliary output channels. The engine modules apply the matrix multiplication computation that is required for phase reconstruction of the gradient measurements and applies the control algorithm. [12]

The control algorithm for the DM is defined by the reconstruction matrix coefficients and the control filter constants. A least-squares solution is derived from the alignment geometry of the actuators and subapertures in order to develop the reconstruction matrices. Through testing of the system, it was found that a reconstruction matrix set for 688 actively controlled actuators with three rings of slaved actuators produces the best results. The physical dimensions of the aperture would appear to be best suited for 756 actuators with two outer rings of actuators slaved to active actuators, yet the performance degrades and is unstable unless the control loop bandwidth is set to unacceptable low levels. The discrepancy between the actual physical dimensions and the model used for the reconstructor matrix was hypothesized to be due to measurement errors in the partially illuminated subapertures on the edges of the WFS. Currently the SOR uses the same filter gain on the servo-loop controller at each actuator position, which does not address the measurement errors on the edge subapertures.

*2.2.2 AO Metrics of Performance.* The performance of an AO system can only be measured by quantifying metrics which are representative of a desired objective because AO is used in many different applications. The mean-square residual

phase, residual phase variance, and Strehl ratio are commonly used in the field of imaging and are described below.

*2.2.2.1 Residual Phase.* The primary objective of an AO system is to correct for an aberrated wavefront with a phase  $\varphi(\mathbf{x})$  by deforming the surface of a mirror such that the wavefront correction  $\hat{\phi}(\mathbf{x})$  is the conjugate of the aberration. The residual phase is the resultant phase of the wavefront after it is reflected off the DM, as shown by

$$\varepsilon(\mathbf{x}) = \varphi(\mathbf{x}) - \hat{\phi}(\mathbf{x}), \quad (2.9)$$

where  $\mathbf{x}$  is the 2-D spatial position coordinate in the pupil plane and  $\varepsilon(\mathbf{x})$  is the residual phase. When the residual phase is minimized, the DM is compensating well for the aberrations. Thus the objective of an AO system is to drive the residual phase to zero in order to fully correct for the disturbance in the phase. This assumes that the aberrations occur near the aperture of the AO system where the phase effects are dominate over amplitude and scintillation effects. [10] This assumption can be made for most astronomical imaging and satellite imaging scenarios. The mean-square residual phase  $\varepsilon^2$  is the residual phase squared and averaged over the frames. Another often-used performance metric is the residual phase variance which is the second central moment, given by

$$\text{VAR}(\varepsilon) = \mathbf{E}[(\varepsilon - \mathbf{E}[\varepsilon])^2]. \quad (2.10)$$

There are many effects that contribute to  $\text{VAR}(\varepsilon)$ , such as finite control bandwidth as discussed in Section 2.1.2.2.

Both can be used as a single-valued metric that is indicative of the performance of the AO system's ability to compensate for the turbulence. The smaller the magnitude of these metrics, the more the system is compensating for the disturbance. Though the mean-square residual phase and residual phase variance are not always

adequate to fully understand how the AO system is performing in its entirety, they are easily accessible metrics and are commonly used.

*2.2.2.2 Strehl Ratio.* The Strehl ratio ( $SR$ ) is a measure of the imaging resolution of the AO system and is determined using the point spread function (PSF). The PSF is the spatial impulse response of imaging a point source. A more narrow PSF corresponds to a higher resolution in the AO imaging system, while aberrations cause the PSF to be wider with poorer resolution. The  $SR$  is given by

$$SR = \frac{\text{PSF}(\mathbf{x}_i = 0)}{\text{PSF}_{dl}(\mathbf{x}_i = 0)}, \quad (2.11)$$

where  $\mathbf{x}_i$  is the spatial vector in the image plane. The  $SR$  can also be approximated by the mean-square residual phase from Section 2.2.2.1 when  $\varepsilon^2 < (2\pi/10)^2 \text{rad}^2$  as shown by

$$SR \approx \exp(-\varepsilon^2). \quad (2.12)$$

### 2.3 Deformable Mirror

The DM is the active physical component of an AO system used to correct for the wavefront aberrations. This device has the ability to physically alter its figure to compensate aberrated light after reflecting off its surface. If an incident aberrated optical field represented by  $A \exp(j\phi(\mathbf{x}, t))$  is reflected off the surface of the DM, the resulting residual wavefront after reflection  $A \exp(j\varepsilon(\mathbf{x}, t))$  can be shown by [10]

$$A \exp(j\varepsilon(\mathbf{x}, t)) = A \exp[j\phi(\mathbf{x}, t)] \exp[-j\hat{\phi}(\mathbf{x}, t)], \quad (2.13)$$

$$= A \exp[j(\phi(\mathbf{x}, t) - \hat{\phi}(\mathbf{x}, t))], \quad (2.14)$$

where  $t$  is time,  $\phi(\mathbf{x}, t)$  is the piston-removed perturbed wavefront phase,  $\hat{\phi}(\mathbf{x}, t)$  is the piston removed surface of the DM, and  $\varepsilon(\mathbf{x}, t)$  is the residual phase of the wavefront after reflection. Piston is the mean value or bias of the wavefront across the pupil of the optical system. An ideal DM would be able to exactly conjugate aberrated

wavefronts so that the residual phase is zero. There are many factors that hinder the DM from physically realizing a perfect conjugate of the wavefront. The DM has limited degrees of freedom based on its number of actuators. Increasing the number of actuators in a DM allows for a better matching with the incident wavefront, but this comes at the price of added cost and complexity to the system. The two main classes of DMs as shown in Figure 2.4 are classified by their surface: segmented and continuous.

Segmented mirror surfaces, also known as a face plates, are divided into partial sections which can be independently controlled. The primary benefits of a segmented mirror are the modularity and simplicity of the components. A segmented mirror allows for easier repair of individual segments because they can be taken out and replaced without affecting neighboring segments. The modularity of each segment also

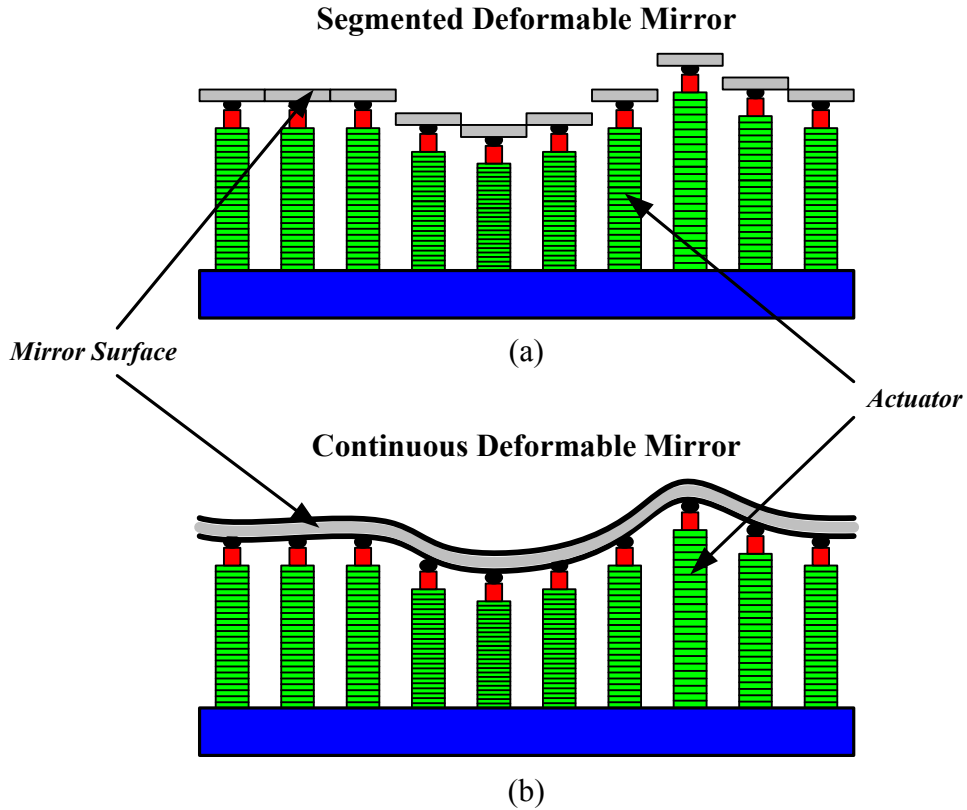


Figure 2.4: Segmented and continuous DMs. (a) Cross-section of a segmented face plate DM. (b) Cross-section of a continuous face plate DM

allows for simpler control algorithms because there is no coupling between actuators. Although there are disadvantages of segmented mirrors which can include difficulty with inter-actuator alignment and diffraction effects due to the segment edges.

Continuous face plates address the diffraction effects associated with the segmented mirrors. Actuators push and pull a thin surface which can be made of a variety of materials such as low expansion glass or single-crystal silicon. The essential characteristics of the surface are that it is flexible, hard enough to be polishable, and strong enough to avoid deformation. The diffraction effects seen in the segmented mirror are avoided by use of a continuous face plate. However, using a continuous faceplate enacts coupling between actuators which can complicate the development of a control algorithm. Also, repairing individual actuators becomes more difficult due to the actuators being coupled together by the continuous face plate.

*2.3.1 Influence Function.* The influence function is a model used to represent how the surface shape of the DM responds to an actuator command. These functions are needed for AO system performance modeling/analysis and can be incorporated in the development of the geometry matrix seen later in Section 2.5.1. The influence function is usually measured by commanding each actuator individually and measuring the response of the wavefront sensor. The most common relationships that are used to describe the influence function of an actuator in a continuous faceplate DM are of cubic and Gaussian form to express the coupling between actuators which normally ranges from 5-15%. [14] Segmented DMs have influence functions that are localized to their particular segment.

## ***2.4 Shack-Hartmann Wavefront Sensor***

SH WFSs are the most commonly used WFS in AO. The SH WFS was originally developed in the 1970s and is based upon the Hartmann test, which was used to determine the quality of large optics for astronomical purposes. The Hartmann test

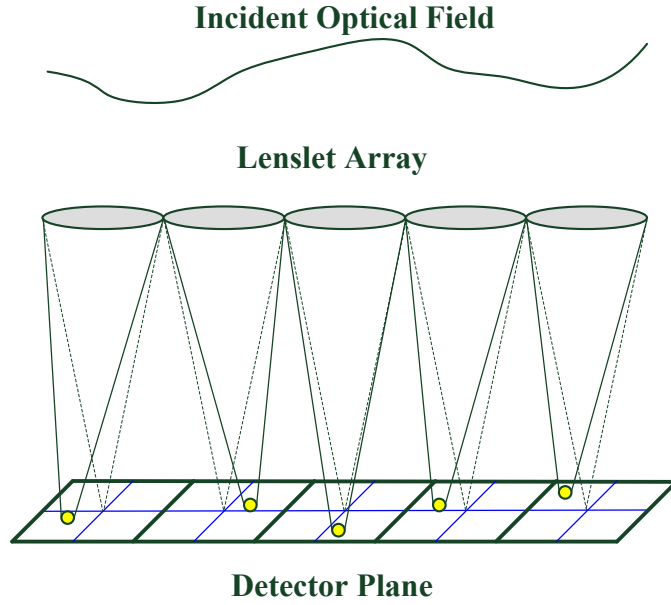


Figure 2.5: One-dimensional depiction of SH WFS. The incident wavefront is spatially divided with the lenslet array and focused on to a quadcell corresponding to each individual lenslet. The local slope of the wavefront is then determined by where the focal spot is focused within each individual quadcell.

uses an opaque mask with holes placed behind the optical element being tested. Because light propagating through the optical element should be converging, each of the holes should produce a PSF in the same location. Due to aberrations, each spot location indicates the local tilt corresponding to the spatial portion of the tested optical element. The SH WFS sensor is based upon this principle but rather than using an opaque mask with holes to produce spots, a lenslet array is used, giving the benefit of more accurate measurements, as shown in Figure 2.5. [13]

The lenslets produce focal spots on the photodetectors where each spot corresponds to a subaperture that calculates the local gradient of the wavefront using the energy imbalance equation found in Section 2.4.1. Figure 2.6 is a configuration of 24 subapertures across a circular aperture in the Fried geometry, which is discussed later in Section 2.5.1. The output is a map of local tilts that are later used in the reconstructor to estimate the wavefront. In order to obtain ideal measurements close to the diffraction limit, the lenslets should be imaged in the plane of the aperture so that they are roughly the size of  $r_0$ . [11].



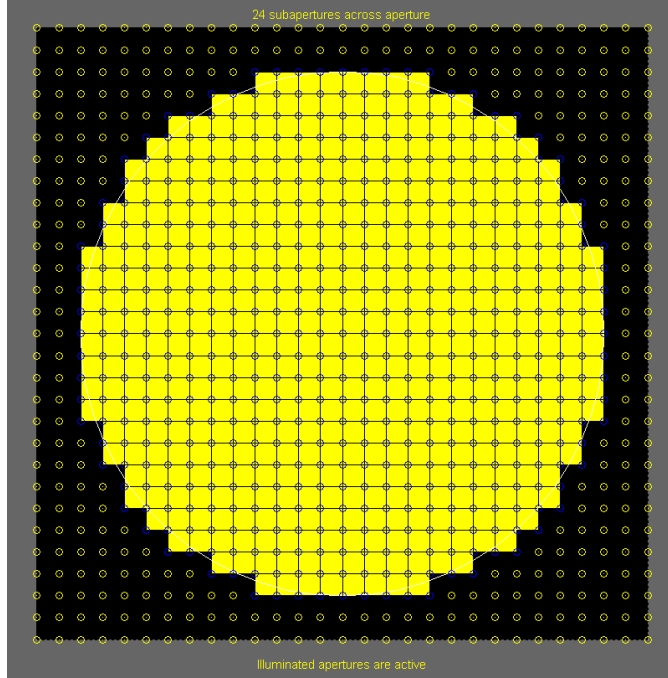


Figure 2.6:  $24 \times 24$  SH WFS subapertures. This configuration has 24 subapertures across the circular aperture. Each square subaperture is spatially defined by four actuators at the corners.

While the SH WFS is great for many applications, it is not the only high-order WFS and has specific advantages and disadvantages to consider. An advantage with using the SH WFS is that its method of collecting light and computing for tilts allows it to work with broadband, incoherent sources. The popularity of SH WFSs is also due to their fast speed, simplicity, small size, and mechanical stability. Although, one key drawback with the way the SH WFS measures the local tilts is that it cannot measure phase discontinuities resulting from dim spots in the pupil. These dim spots cause branch points which are normally only a factor in high scintillation conditions.

*2.4.1 Energy Imbalance Equation.* The energy imbalance equation is used in the calculation of the local tilt of the wavefront for each subaperture in the SH WFS. The quadcells of the sensor are composed of four separate pixels A,B,C, and D that correspondingly measure the intensities  $I_A$ ,  $I_B$ ,  $I_C$ , and  $I_D$  as shown in Figure 2.7. The local wavefront tilt in the subaperture is then computed using the energy imbalance

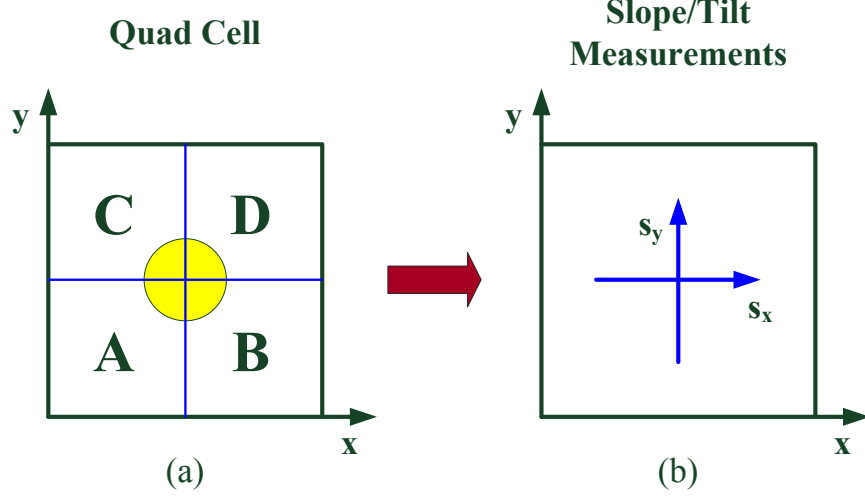


Figure 2.7: Quad cell and slope measurements. (a) Quad cell with centered focal spot. (b) Calculated slopes.

equation as given by

$$s_x = \frac{(I_B - I_A) + (I_D - I_C)}{(I_A + I_B + I_C + I_D)}, \quad (2.15)$$

$$s_y = \frac{(I_C - I_A) + (I_D - I_B)}{(I_A + I_B + I_C + I_D)}, \quad (2.16)$$

where  $s_x$  and  $s_y$  are the transverse slopes. These slopes are multiplied by a calibration factor which takes into account local measured biases.

*2.4.2 Shack-Hartmann WFS Measurement Errors.* The SH WFS is quite accurate at measuring a wavefront under controlled conditions, yet there are multiple factors associated with the sensor that can contribute errors into the measurements.

*2.4.2.1 Dynamic Range of Measurable Tilt.* The measurable tilt over a subaperture is largely dependent upon the width of the spot focused onto the quad-cell. The dynamic range of measurable tilt per subaperture is limited by focal spot size because large spots have little available displacement before moving into an adjacent subaperture. [7] The effects of a large spot size can be reduced by buffering neighboring subapertures from each other with additional pixels. Yet on the other

hand, the spot size should not be too small because it can decrease the sensitivity of the sensor. Spots need to be fully incident on all four quadrants of the quadcell in order to properly measure the gradient correctly, which is another limit to the dynamic range. Increasing the resolution of the detector array can help mitigate some of these detrimental effects, but this comes at the cost of increasing the read out time and noise effects due to the electronics. Due to the constraints on the spot size, the linear dynamic range of the SH WFS is approximately  $\pm\frac{1}{2}$  waves of tilt, which is normally acceptable in closed-loop operation.

*2.4.2.2 Electronic Crosstalk.* The detector array in a SH WFS is subject to electronic crosstalk between adjacent pixels, and subsequently neighboring subapertures. Pennington [6] evaluated the performance of Generation III WFSs at the SOR and looked at the electronic crosstalk between pixels of the sensor. Electronic crosstalk occurs when a photon hits a particular pixel but get registered in another. Each pixel’s crosstalk potential can be represented by a probability density function (PDF) describing the likelihood of crosstalk with another pixel given the position of where the photon hits in the cell. The region of crosstalk is where two adjacent pixels’ PDFs overlap. The width of the PSF of the lenslet has a direct relationship to the effects of electronic crosstalk. By making the size of the PSF larger than the region of crosstalk, Pennington was able to increase the sensitivity of the WFS. Each subaperture was designated a  $4 \times 4$  region of pixels to register the focal spot of a lenslet. The center  $2 \times 2$  pixels were used for the calculation of the energy imbalance equation, while the outer region of pixels was used as a guardband to prevent crosstalk between subapertures. Measuring larger gradients is subject to even more error depending upon the size of the quadcell and PSF. Increasing the size of the PSF and using a guardband of pixels decreased crosstalk which subsequently increased the loop stability of the AO system by improving the sensitivity of the WFS, and hence decreasing noise sensitivity.

### 2.4.2.3 Non-Uniform Focal Spot.

Sometimes SH WFS focal spots become elongated for a variety of reasons. Beckers [3] examined how the spot elongation varied in a SH WFS depending on its location in the pupil and the perspective elongation effect due to the placement of a laser-launching system for a laser guide star. The spots farthest from the LGS launching system showed the most elongated focal spots. Becker found that if the laser launching system is located over 3 meters from the telescope aperture, the elongations become larger than 1 arcsec which can negatively affect the sensitivity of the SH WFS. Figure 2.8 shows the focal spots of a SH WFS with an on-axis reference beam. The figure shows how the focal spots at the center subapertures near the on-axis reference are more uniform and circular, while the edge focal spots are more oblong due to the position of the reference.

The focal spot is also affected by the resonant scattering cone of an LGS, whether it be a sodium or Rayleigh guide star. When a LGS is created in the atmosphere it is not a perfect point source. With respect to the sodium guidestar, the beacon has a finite angular extent due to the thickness of the sodium layer and can

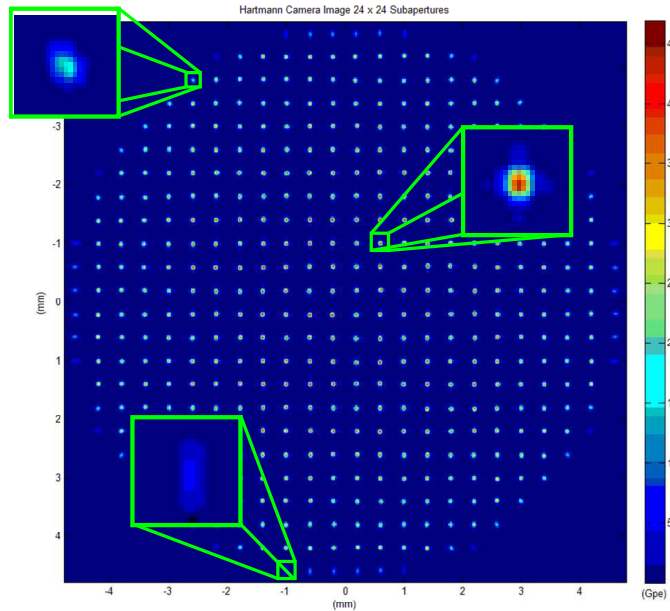


Figure 2.8: Focal spots over SH WFS with on-axis reference beam. Center subapertures near the on-axis reference beam have symmetrical focal spots. Edge subapertures that are farther from the center are elongated.

induce elongation in SH WFS focal spots if the laser is launched from the side of the telescope. Viard [15] found that the elongation of the focal spot with respect to a sodium guidestar effects the accuracy of the SH WFS by about 3-5% in open-loop, yet when the AO system is in closed-loop, the effects are negligible. Rayleigh scattering produces a cone of light when propagating a beacon. The intensity of the Rayleigh scattering is a function of the distance the telescope is from the launching of the laser beacon. Viard simulated an 8 meter telescope with a 5 W laser launched from a 1.5 meter auxiliary telescope. When the laser launcher was placed at 0.5 meters from the 8 meter telescope the light coming from the reference beacon spot in the atmosphere was saturated by the cone of the beam being projected, inducing 10% more light, because it is so close to the aperture. At 10% the focal spot becomes highly pertubated which adds error to the sensitivity of the WFS measurements. Though it was found that the relative intensity of the Rayleigh scattering exponentially decreases as the laser launcher is moved away from the primary telescope. The sensor is not significantly affected by the Rayleigh scattering if the cone only pertubates the beacon by 2% of the total intensity. After moving the laser launcher beyond 0.5 meters, the Rayleigh scattering of the cone is below 2% of the effective intensity and becomes negligible with respect to the SH WFS measurements.

The shape of the focal spot is ideally an Airy pattern in order to have the same dynamic range in the  $x$ - and  $y$ -components of measurable tilt. Asymmetric focal spots that can arise have different amounts of dynamic range of measurable tilt with respect to the energy imbalance equation that is used for the SH WFS. Figure 2.9 shows an example of an elliptical focal spot that would have a distinctly different  $y$ -slope dynamic range as compared to the  $x$ -slope because of how the focal spot is illuminated in the quadcell. The  $y$ -component of the spot is elongated which can cause errors if it supercedes the outer guard pixels and enters another subaperture. The smaller  $x$ -component would have decreased measurement sensitivity because no additional tilt can be determined if the entire focal spot has entered one of the sections of two cells because the intensity would not be changed in the energy imbalance equation.

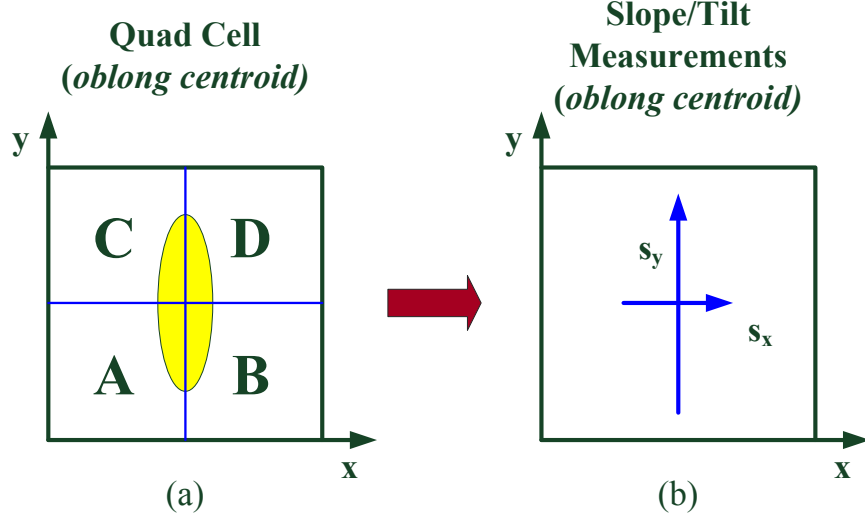


Figure 2.9: Asymmetrical centroid slope measurements. (a) Quad Cell with asymmetrical focal spot. (b) Calculated slopes are no longer uniform causing errors in the measurements.

Overall, the discrepancy in how the  $x$ - and  $y$ -components measure tilt causes errors in the determination of the resultant slope.

*2.4.2.4 Camera Noise Threshold.* Wavefront measurements with low intensities have induced errors due to camera noise. Plett [7] found that there was a sharp upswing in the error of the measurements when the spot intensity was near the level of the noise in the camera. At low intensities of the signal, the noise drowns out the accuracy of the measurements. Rather than compensating for errors in the wavefront, the AO system begins to follow the noise. The most susceptible area on a SH WFS for low intensity illumination is the edge subapertures. The illumination of a beam profile is circular and does not fully match the square geometry of how the subapertures are defined. Therefore some of the edge subapertures are not fully illuminated, which is a cause for lower illumination levels, as shown in Figure 2.10.

The most common metric used to define the correspondence between the level of noise as compared to the signal is known as the signal-to-noise ratio (SNR). There are multiple renditions of how to calculate the SNR, but in the case of this research

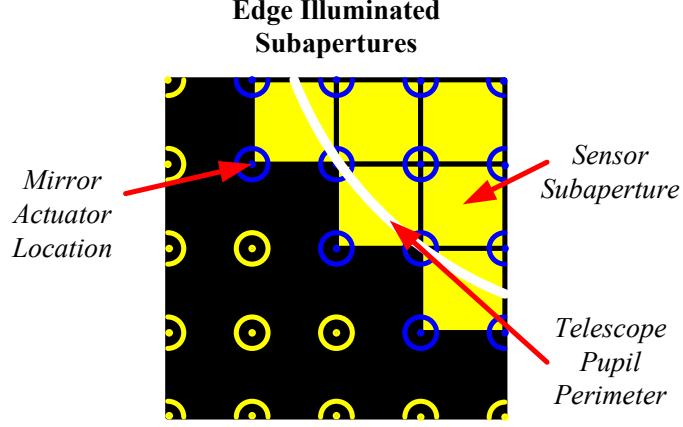


Figure 2.10: Partially illuminated edge subapertures. Due to the square geometry of the subapertures, the WFS does not fully match the circular profile of the aperture. This causes the edge subapertures to have lower illumination levels, making them more sensitive to noise effects.

the SNR will be calculated over a detector array as given by [14]

$$SNR = \frac{n_p}{\left\{ n_p + N_D \left[ n_B^2 + \left( \frac{e_n}{G} \right)^2 \right] \right\}^{1/2}}, \quad (2.17)$$

where  $n_p$  is the sum of the detected photoelectrons over the entire subaperture;  $N_D$  refers to number of pixels in a subaperture (e.g. for a quadcell  $N_D = 4$ );  $n_B$  is the number of background photoelectrons detected over the subaperture;  $e_n$  is the number of electrons due to the read noise over a subaperture and  $G$  is the gain over the array.

The sensor error of a SH WFS depends on multiple contributing factors besides the SNR, such as the size of the subapertures  $d$ , error due to the gaps between pixels in the focal plane of the detector  $K_g$ , coherence length of the atmosphere  $r_0$ , and angular size of the reference source  $\theta_r$ . These contributions are related to the measured rms wavefront error (radians) over a subaperture by [14]

$$\sigma_\phi = \frac{\pi^2 K_g}{4 SNR} \left[ \left( \frac{3}{2} \right)^2 + \left( \frac{\theta_r d}{\lambda} \right)^2 \right]^{1/2}, \quad r_0 > d, \quad (2.18)$$

$$\sigma_\phi = \frac{\pi^2 K_g}{4 SNR} \left[ \left( \frac{3d}{2r_0} \right)^2 + \left( \frac{\theta_r d}{\lambda} \right)^2 \right]^{1/2}, \quad r_0 < d. \quad (2.19)$$

Therefore, Eqs. (2.18) and (2.19) show that as the SNR decreases, the rms wavefront error of the SH WFS increases, and vice versa. The wavefront error is another factor that contributes to Eq. 2.10.

## 2.5 Reconstruction of Phase

SH WFSs cannot measure phase directly. Instead, it measures wavefront gradients over each subaperture. Therefore the gradients from the SH WFS are used to piece together a map of the phase so that it can be used with the servo-controller for the DM, as shown in Figure 2.11. The spatial frequency of the reconstructed phase is a factor of the number of subapertures used. [9] There are multiple alignment geometries that give the registration between the actuators and the WFS subapertures such as the Hudgin geometry, Southwell geometry, and Fried geometry. Each of the geometries has its own characteristics that affect the stability of the control system, but for this research the Fried geometry is used in the ASALT lab.

*2.5.1 Fried Geometry.* The Fried geometry is a common choice in many AO systems because of the low computational complexity and its relation to square detector arrays. The Fried geometry defines the relationship between the relative slopes over each subaperture measured by the SH WFS and the phase of the actuators at the corners of the subaperture. Figure 2.12 is a depiction of the Fried geometry over

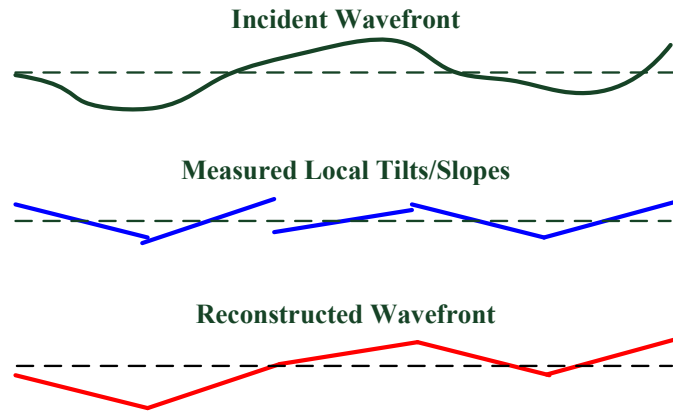


Figure 2.11: Reconstructed phase from gradient measurements.



## Fried Geometry

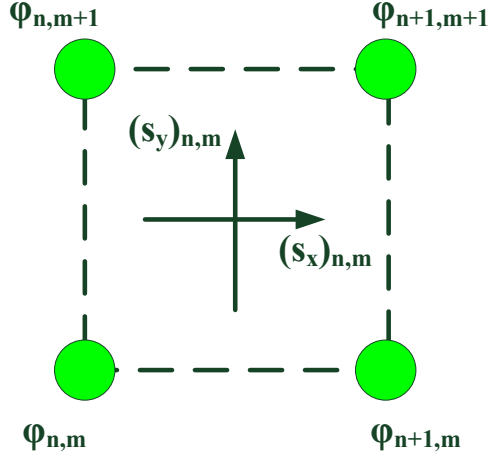


Figure 2.12: Fried geometry. The slope measurements over the subaperture are used to estimate the phase at the corner actuator positions.

a subaperture where  $\varphi_{n,m}$ ,  $\varphi_{n+1,m}$ ,  $\varphi_{n,m+1}$ , and  $\varphi_{n+1,m+1}$  are the phases of the actuators and the subscripts  $(n, m)$  designate a specific actuator position.

The Fried Geometry gives a direct relationship between the measured  $x$  and  $y$  slopes of the subaperture  $(s_x)_{n,m}$  and  $(s_y)_{n,m}$ , and phase at the actuator locations given by

$$(s_x)_{n,m} = \frac{1}{2}(\varphi_{n+1,m} - \varphi_{n,m}) + \frac{1}{2}(\varphi_{n+1,m+1} - \varphi_{n,m+1}), \quad (2.20)$$

$$(s_y)_{n,m} = \frac{1}{2}(\varphi_{n,m+1} - \varphi_{n,m}) + \frac{1}{2}(\varphi_{n+1,m+1} - \varphi_{n+1,m}). \quad (2.21)$$

The factor of  $1/2$  in Eqs. (2.20) and (2.21) is due to the correction system, or DM, being reflective. When a reflective corrector is moved by an actuator a distance  $d$ , the optical path that the light travels is  $2d$ , which then needs the  $1/2$  factor to represent the effect in the actuator commands. [11] Due to the magnitude of actuators that are used, Eqs. (2.20) and (2.21) can be represented over all of the actuators in matrix form,

$$\mathbf{s} = \mathbf{A}\varphi, \quad (2.22)$$

where  $\mathbf{s}$  represents the measured slopes over each subaperture,  $\mathbf{A}$  is the Fried geometry's mathematical relationships, and  $\varphi$  represents the phase of the wavefront over the actuators. The influence function mentioned in Section 2.3.1 can be incorporated in the development of the geometry matrix, which takes into account the inter-actuator coupling effects.

*2.5.2 Least-Squares Estimation.* In order to produce an estimate of  $\varphi$ , designated as  $\phi$ , from the slope measurements  $\mathbf{s}$ , a relationship must be defined such that

$$\phi = \mathbf{M}\mathbf{s}, \quad (2.23)$$

where  $\mathbf{M}$  is referred to as the reconstructor matrix. Noting that in Eq. (2.22), the geometry matrix  $\mathbf{A}$  defines the relationship between the measured slopes and the phase, an inversion of  $\mathbf{A}$  is used to produce an estimate of  $\mathbf{M}$ . LS estimation is the most common technique due to its minimal complexity performing a pseudoinverse of  $\mathbf{A}$  as shown by

$$\phi = \mathbf{A}^+\mathbf{s}, \quad (2.24)$$

$$\phi = (\mathbf{A}^T\mathbf{A})^{-1}\mathbf{A}^T\mathbf{s}, \quad (2.25)$$

$$\phi = \mathbf{M}\mathbf{s}. \quad (2.26)$$

It should be noted that there are other more optimal techniques to develop  $\mathbf{M}$  rather than the LS estimate, which incorporate noise statistics and/or *a priori* information about the atmospheric characteristics and various servo-loop considerations. The LS estimate is actually a reduction of the maximum *a posteriori* estimation which utilizes the noise variance of the measurement models and the control signal covariance matrix. Yet in the case of the LS estimation, the noise variance is set to zero, implying that no errors were induced from misregistration. Assuming a noiseless system allows the LS estimator to satisfy the condition that  $\phi = \varphi$ , implying that  $\mathbf{M}\mathbf{A} = \mathbf{I}$ . Not all estimators satisfy this condition. [20] Including the noise effects allows the

production of a weighted LS estimator that is really only useful when accounting for the illumination effects over the subaperture. Therefore an illumination fraction could be used such that a fully illuminated subaperture would be weighted with unity, while a completely unilluminated subaperture would be designated as zero. However, computing a weighted LS estimator in real time is not feasible due to rapid intensity fluctuations and the large computational burden. [16]

## 2.6 Servo-Controller

The servo-controller takes the wavefront sensor measurements and maps them to the actuator control signals in order to command the DM such that  $\phi(\mathbf{x}, t) \approx \hat{\phi}(\mathbf{x}, t)$  is achieved. A discrete-time interval is used in the modeling of the servo-controller because it better characterizes the integration time of the WFS and the spatial subapertures. The servo-loop model introduces a temporal response developed by Wild [16] which shows how the updates are distributed to the DM by a first-order difference equation, as given by

$$\phi(t_{i+1}) = a\phi(t_i) + b\mathbf{M}[\mathbf{s}(t_{i+1}) - \mathbf{A}\phi(t_i)], \quad (2.27)$$

where  $\phi(t_{i+1})$  is the next mirror update to the DM,  $\phi(t_i)$  is the current mirror update,  $a$  is the lossy integrator gain,  $b$  is the filter gain, and  $\mathbf{M}[\mathbf{s}(t_{i+1}) - \mathbf{A}\phi(t_i)]$  is the reconstructed slope error from the residual phase reflected off the shape of DM during the prior time interval.

*2.6.1 Digital Filter Model.* Another realization of the servo-loop difference equation by Barchers [2] can be utilized to give a model that is more conducive to conceptually understanding the difference equation as a discrete digital filter in terms of control theory. This filter is modeled as a single-input single-output (SISO) system and corresponds to a single actuator position. Currently, the gains of this model are the same over all of the actuators across the DM, yet later in Section 3.5.2.3 the gains

are dependent on the spatial location of the actuator. The discrete digital filter for the DM as shown by Barchers is [2]

$$c_{k+1} = ac_k + (1 - a)K_{DC}e_{k+1}, \quad (2.28)$$

where  $c_{k+1}$  is the next command to the DM,  $c_k$  is the current command,  $a$  is still the lossy integrator gain,  $K_{DC}$  is the DC gain of the filter, and  $e_{k+1}$  is the reconstructed residual phase off the DM. As can be shown, Eq. (2.27) and Eq. (2.28) have the same structure. Each of the mirror updates  $\phi(t_i)$  are representable as DM commands denoted by  $c_k$ , and the filter gain  $b$  is shown as  $(1 - a)K_{DC}$ . Also the reconstructed residual phase from the second term of Eq. (2.27) is shortened to  $e_k$ . The lossy integrator  $a$  is related to the cutoff frequency  $f_0$  and the sampling period of the system  $T_s$ , by  $a = \exp(-2\pi f_0 T_s)$ . The two parameters  $K_{DC}$  and  $f_0$  are often referred together by AO operators with the phrases such as “90 and 1” where  $K_{DC} = 90$  and the cutoff frequency  $f_0 = 1$ . These terms may be used by an operator adjusting the gains of the digital filter while watching over the performance of the DM with respect to rejection of disturbances. Eq. (2.28) can be further simplified for the purpose of brevity in this research as shown by

$$c_{k+1} = ac_k + be_{k+1}, \quad (2.29)$$

where  $b = (1 - a)K_{DC}$ .

Because the processes in an AO system are discretized for computational purposes and assuming that the system is linear and time-invariant,  $z$ -transforms can be used to simplify the representation of the system in the complex frequency domain. For a given discrete sequence  $f_k$ , the  $z$ -transform can be shown as

$$f(z) = Z(f_k) = \sum_{k=0}^{\infty} f_k z^{-k}, \quad (2.30)$$

where  $z = \exp(j2\pi T_s f)$  in this AO analysis. With the given representation of  $z$ ,  $T_s$  is the sampling time of the AO system in seconds,  $f$  is the frequency in Hertz, and  $f(z)$  is the  $z$ -transform of the sequence  $f_k$ .  $Z$ -transforms are particularly useful for reducing sequences of data in difference equations, into transfer functions. Therefore utilizing  $z$ -transforms, Eq. (2.29) can be represented as a transfer function  $F(z)$  shown as

$$c(z)z = ac(z) + be(z)z \implies F(z) = \frac{e(z)}{c(z)} = \frac{bz}{z - a}. \quad (2.31)$$

Transfer functions give the mapping between the input sequence such as  $c(z)$  and the output sequence such as  $e(z)$ , in this case. Looking at the digital filter  $F(z)$ , shows that it is in the form of a proportional-integral-derivative (PID) controller.

*2.6.2 Rejection Functions.* Rejection functions are useful tools often used in control theory for analyzing a system's response to disturbances in the frequency domain. For the application of AO, the incoming aberrated phase can be considered the disturbance and the residual phase off the DM is considered the system's response.

When considering how the closed-loop AO system rejects turbulence, the ERF  $S(z)$  also known as the sensitivity transfer function, can be utilized to describe how the reconstructed residual phase  $e(z)$  corresponds to the disturbance  $d(z)$ , representing the aberrated phase  $\phi$ , as shown by

$$S(z) = \frac{e(z)}{d(z)} = \frac{1}{1 + L(z)}, \quad (2.32)$$

where  $L(z)$  represents the loop transfer function. The loop transfer function would be the mathematical model of the open loop system relating the actuator positions of the DM  $h(z)$  to the measured residual phase  $e(z)$ , where  $L(z) = h(z)/e(z)$ . Therefore the loop transfer function would include the DM Filter  $F(z)$ . The modulus of the error rejection function,  $|S(z)|$  can then be plotted in order to find the ERF bandwidth  $f_{3dB}$ . The  $f_{3dB}$  refers to the frequency where the ERF is at a magnitude of -3dB. The AO community commonly refers to the  $f_{3dB}$  of the ERF as the bandwidth of the

system. [2]

Another important rejection function that is intrinsically linked to the ERF is the noise rejection function (NRF), also known as the complementary sensitive transfer function. The noise rejection function  $T(z)$  shows how the closed-loop AO system rejects the measurement noise  $n(z)$ , with respect to the reconstructed residual phase  $e(z)$  as shown by

$$T(z) = \frac{e(z)}{n(z)} = \frac{L(z)}{1 + L(z)}. \quad (2.33)$$

The NRF illuminates over what frequencies the AO system rejects noise, which can be a vital tool to use for mitigation techniques.

An important property of the ERF and NRF are that they are the complement of one another sharing the relationship,

$$S(z) + T(z) = 1. \quad (2.34)$$

The digital filter described in Eq. (2.28) can be used to adjust the bandwidth of the ERF and NRF. Specifically, the  $a$  and  $b$  gains are two adjustable servo-loop parameters that determine how the AO system responds to different disturbances, hence they are used in the controller. Varying these two parameters adjusts the pole-zero placement of the AO system which then alters the temporal response and therefore changes the bandwidths over the ERF and NRF.

As an example, the NRF and ERF should be adjusted accordingly with respect to what disturbance is being rejected. Figure 2.13 depicts a PSD of an atmospheric disturbance along with the PSD of the noise which is practically uniform over all frequencies. In order to effectively reject the disturbance, the ERF should be adjusted with the servo-loop parameters  $a$  and  $b$ , as shown in Figure 2.14. The modulus square of the ERF is basically the inverse of the atmospheric PSD, which means that where the PSD of the atmosphere has the most power is where the sensitivity to the disturbance is lowest. This implies that the system is rejecting the disturbance (or compensating) in the frequency region that the atmosphere is most distributed.

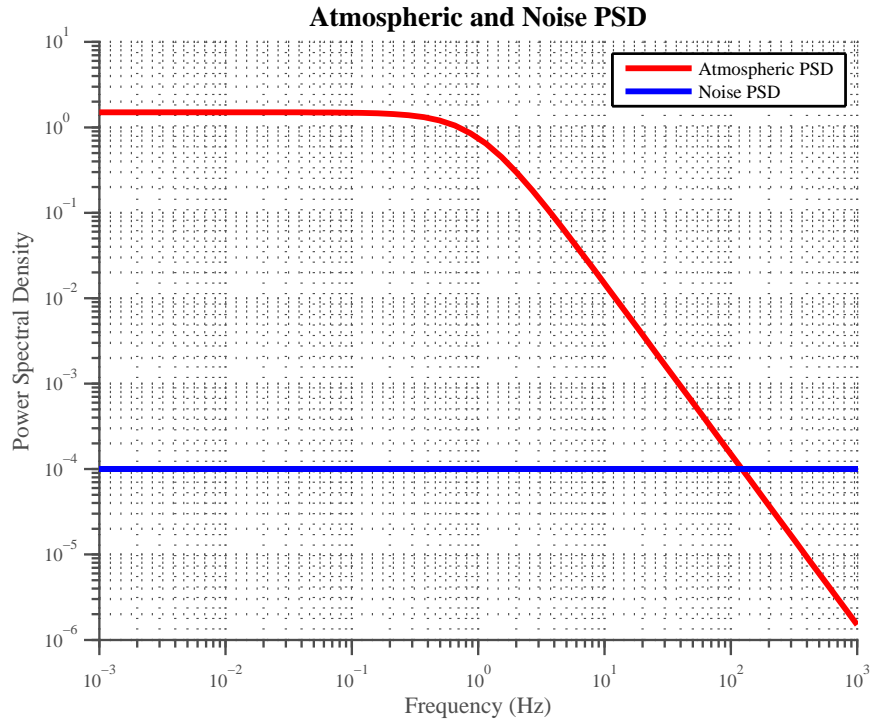


Figure 2.13: Example of atmospheric and noise PSD.

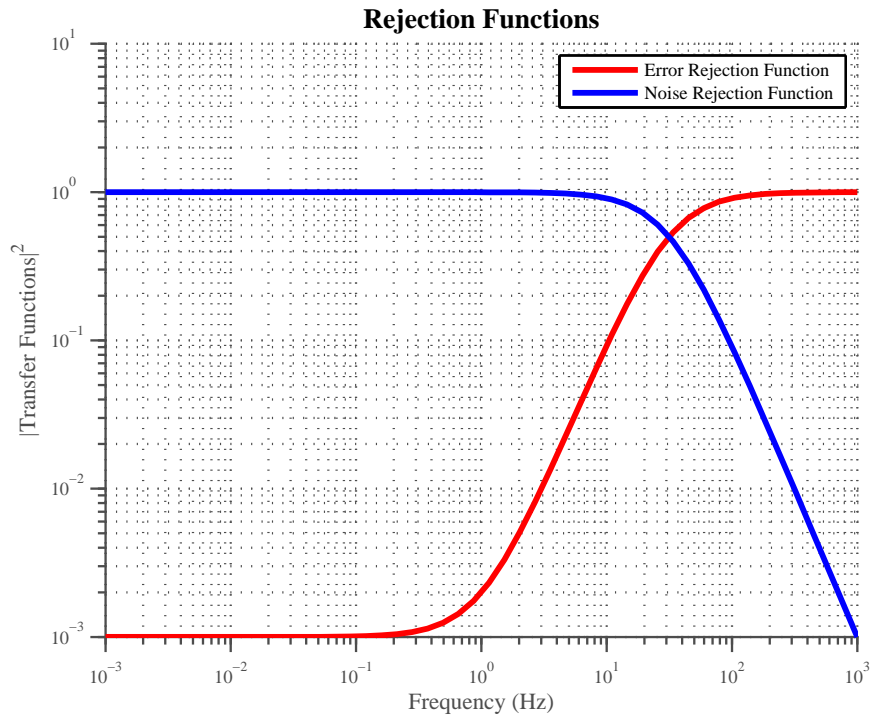


Figure 2.14: Example of ERF and NRF..

Conveniently the NRF is small when the sensitivity to the disturbance is large at high frequencies, implying that noise is being attenuated. [2]

## 2.7 Stability

The ‘stability’ of an AO system can be considered to be a relative term that is often used in a variety of situations. The stability of an AO system is often linked to the performance of the DM with respect to how it compensates for a disturbance. Though just because the performance is degraded and the DM may be oscillating erratically, does not mean to imply that the system is unstable in terms of mathematical solutions of the dynamical system. Lyapunov stability is a mathematical construct of determining the stability of a dynamical system, while erratic behavior of the DM with effects such as the waffle mode on a DM are instability indicators coined off of experience and the performance of the AO system.

*2.7.1 Lyapunov Stability.* Wild [18] investigated conditions that would make an AO system go unstable with respect to the servo-loop gain and reconstructor matrix. Lyapunov theory indicates the conditions where the phase-space trajectories of a system begin to diverge from an initial condition. In the specific case being examined here the phase-space trajectory is the phase. For the Lyapunov stability analysis, Wild’s model Eq. (2.27) will be used though there is an equivalent correspondence to Barcher’s digital filter model Eq. (2.28). Using Wild’s servo-loop model with the redefined filter gain  $b$  and lossy integrator gain  $a$  which determines the DM updates given in Section 2.6 is shown as [20]

$$\phi(t_{i+1}) = a\phi(t_i) + b\mathbf{M}[\mathbf{s}(t_{i+1}) - \mathbf{A}\phi(t_i)], \quad (2.35)$$

$$= b\mathbf{M}\mathbf{s}(t_{i+1}) + \mathbf{F}\phi(t_i), \quad (2.36)$$

where  $a$  is the lossy integrator,  $b$  is the servo-loop filter gain,  $\mathbf{M}$  is the reconstructor,  $\mathbf{F} = a\mathbf{I} - b\mathbf{M}\mathbf{A}$ , and  $\mathbf{I}$  is the identity matrix. As shown in Section 2.5.1 the geometry



matrix  $\mathbf{A}$  determines the relationship between the WFS measurements of the slopes  $\mathbf{S}$  and the phase  $\phi$  at the actuators by  $\mathbf{s} = \mathbf{A}\phi$ .

For a continuous time-invariant dynamic system, the Lyapunov stability criteria states that a system is asymptotically stable if there exists a differentiable scalar function  $V(x)$  such that along the system trajectories  $V(x) > 0$ ,  $V(0) = 0$ , and  $dV/dt < 0$ , for  $x = x(t)$ . [20] Though with respect to the discrete-time linear system shown in Eq. (2.36),  $V(x)$  can be represented in quadratic form

$$V\phi(t_i) \equiv \phi(t_i)^T \mathbf{P}\phi(t_i), \quad (2.37)$$

where  $\mathbf{P}$  is a positive-definite matrix.

The stability of the closed-loop system can be analyzed by examining the error propagation equation  $g_n$ , also known as the noise gain. The error propagator equation is shown explicitly in summation form as shown by [18]

$$g_n = \frac{b^2}{N_a} \text{tr} \left\{ \lim_{\Omega \rightarrow \infty} \sum_{j'=0}^{\Omega} \sum_{j''=0}^{\Omega} \mathbf{F}^{\Omega-j'} \mathbf{M} \mathbf{M}^T (\mathbf{F}^T)^{\Omega-j''} \right\}, \quad (2.38)$$

where the number of controlled actuators in the pupil is shown as  $N_a$ , and the number of steps that are required to evaluate the error propagator is shown as  $\Omega$ . A closed-form expression of the error propagator can be formed by commuting matrices within the trace of Eq. (2.38) and making the following assumption

$$\sum_k (\mathbf{F}^T \mathbf{F})^k \approx \sum_k (\mathbf{F}^T)^k \mathbf{F}^k. \quad (2.39)$$

By making the assumption of Eq. (2.39) the closed-form expression can be given as

$$g_n = \frac{b^2}{N_a} \text{tr} [I - \mathbf{F}^T \mathbf{F}]^{-1} \mathbf{M} \mathbf{M}^T, \quad (2.40)$$

which can be used in order to determine the stability of the closed-loop system. Therefore the conditions dictated by  $g_n$  can indicate when the system goes unstable due to the sensitivity of the buildup of noise on the DM. When the error propagator equation  $g_n$  diverges, the system is deemed to be unstable because the solution of  $\mathbf{P}$  no longer remains positive-definite which is a requirement for stability. The error propagator equation  $g_n$  reveals the importance of how  $\mathbf{M}$ ,  $\mathbf{A}$ , and  $b$  contribute to the overall stability of the closed-loop system in AO.

*2.7.2 Slaving Considerations.* Actuators that lie outside of the pupil region of the DM are not sensed by the wavefront sensor, but have a direct relationship to the outer sensed actuators due to the coupling effects of a continuous face plate DM. Without enacting control over these outside actuators, errors can occur due to the overcompensation of the coupled edge actuators inside the pupil region during closed-loop feedback of the system. Therefore slaving the outside actuators to the edge actuators inside the DM is commonly practiced to address the ridging that occurs between controlled and non-controlled actuators and can be implemented in the wavefront estimator,  $\mathbf{M}$ . There are two ad hoc slaving methods that are commonly used, direct slaving and linear extrapolation slaving. [17] Direct slaving applies the same control voltage to each of the given actuators, while linear extrapolated slaving takes the two actuators that are in the pupil and produces a linear extrapolation of the control signal for the actuators they are slaved to as shown in Figure 2.15.

The slaving of actuators are applied in order to improve performance of the AO system, but have also been known to be the cause of instabilities. Though the slaving may make intuitive sense, it has no statistical bearing to the atmosphere and can cause unnatural ridging within the DM. Due to the partial illumination of subapertures which causes lower SNR and noisy slope measurements on the controlled edge subapertures, error can propagate through the system. The errors in the system have been found to propagate either proportionally or linearly into the region of slaving depending on whether the direct or linear extrapolation method is used. Wild [18]

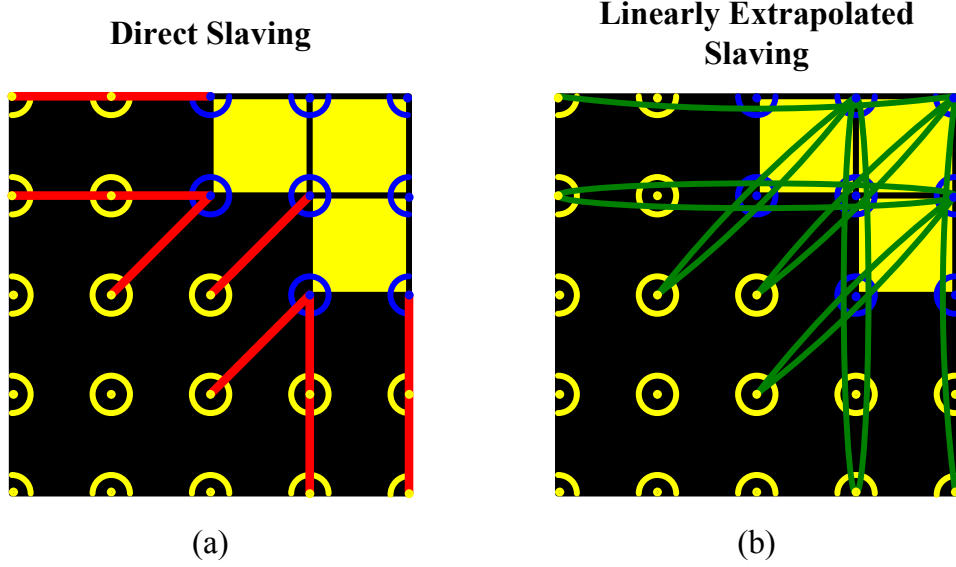


Figure 2.15: Direct and linearly extrapolated slaving. (a) Direct slaving of actuators on a corner area of subapertures. (b) Linearly extrapolated slaving of actuators on a corner area of subapertures.

examined how the error propagator equation  $g_n$  given in Section 2.7.1 changed as a function of loop gain  $b$  and the type of slaving used. The error propagator analyses found that the linear extrapolation method increased faster than direct slaving or optimal linear extrapolation slaving based on the statistics of the atmosphere.

*2.7.3 Waffle Mode.* Waffling has been found to be a prevalent unsensed mode which can lead to instabilities over a DM. WFSs with square subapertures aligned to the corner-positions of a DM coupled with a Fried geometry reconstruction method is particularly susceptible to this mode, as shown in Figure 2.16. The Fried geometry has no cross-coupling in the discrete-point reconstruction of the phases on the actuators. This allows piston differences between two independent actuator spaces to be unsensed in the reconstruction of the phase. The waffle pattern actually occurs when the phase between two actuators are sensed to be zero when in actuality they have piston differences. For example, using Eqs. (2.20) and (2.21), if  $\varphi_{n+1,m}$  and  $\varphi_{n,m+1}$  each have  $+2\mu\text{rad}$  of phase, and  $\varphi_{n+1,m+1}$  and  $\varphi_{n,m}$  each have  $-2\mu\text{rad}$  of phase, then  $(s_x)_{n,m}$  and  $(s_y)_{n,m}$  are equal to zero. Therefore, in this example no

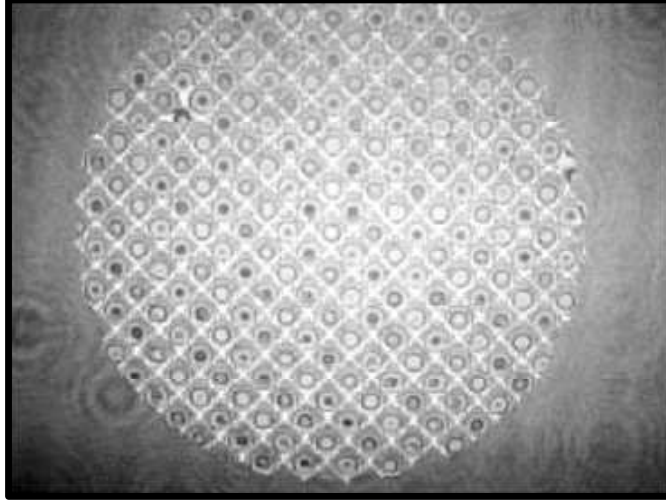


Figure 2.16: Waffle mode over a DM. An interferogram over a DM is shown with the actuators commanded to the waffle pattern.

slope is measured by the SH WFS, though there is an actual nonzero slope between the phases at the actuator locations. Consequently, during the reconstruction of the phase some of the phase points are over the mean rms level and accumulates into waffle. This can also occur when subapertures with low SNR have noisy measured gradients that produce large spikes in the reconstructed phase and are reconstructed to produce a waffle. [19] The waffle pattern can then accumulate over the sensor in a closed-loop feedback system because the sensor cannot sense the mode for compensation.

Wild [20] investigated different types of wavefront estimators in order to compensate for the waffle mode. The Wavefront Control Experiment (WCE) geometry is similar to the Fried geometry mathematically, and was also found to be susceptible to the waffle mode. Yet Wild found with experiments at the SOR, that WCE can be used with optimal estimators to reduce waffle to a greater degree than the LS estimator, without reducing the  $SR$ .

A Laue-type diffraction pattern can form in the image plane of the system when the DM is in a waffle mode. This diffraction pattern has been noted to occur when compensating for a star with a regular arrangement of spots over long exposures. [20]

### III. ASALT Laboratory Setup and Experiment Methodology

The experiments for this research were conducted in the ASALT laboratory which is located at the Starfire Optical Range, Kirtland AFB, NM. The initial two experiments, the Slope Measurement Sensitivity Test (SMST) and Analysis of Slaving Effects Experiment (ASEE), were performed to gain an understanding of how the edge subapertures and actuators affect the performance and stability of an AO system. With the concept of variable isolation in mind, the SH WFS's performance in taking local gradient measurements was first examined with respect to the spatial position of the subapertures. This allowed for a direct comparison of fully illuminated, to partially illuminated subaperture slope measurements. Experiments were then conducted with and without the slaving of the actuators over the DM in order to verify the effectiveness of slaving in the AO system. Examining the performance of the initial experiments provided the motivation behind mitigation techniques for edge effects, as examined in the analysis of non-uniform gain over the controller for the DM.

#### 3.1 ASALT Laboratory

The ASALT's primary mission is to provide research in the testing and development of advanced AO technologies since its construction in 2002. In order to fulfill this mission, they have three fully functioning AO systems that can provide controlled environments for experimentation. This research was conducted in the SRI-2 laboratory which houses one of those AO systems.

*3.1.1 Laboratory Overview.* The SRI-2 laboratory contains two optical tables with one active single DM AO setup that is highly reconfigurable. To achieve such flexibility, the optics hardware is integrated with a custom application programming interface (API). The primary components and design specifications on the table were already setup and verified for closed-loop operations. The optical table

- is configured as a zonal AO system,

- is configured with the Fried geometry,
- uses a continuous faceplate DM with 577 channels, 27 actuators across the aperture, ITEK,
- uses a SH-WFS with a InGaAs camera,  $320 \times 200$  pixels,  $30\mu\text{m}$  pixel size,
- and operates with a 1550 nm diode laser source with 1 meter pigtail and a FC/PC connector Avanex.

The entire laboratory is temperature-regulated to mitigate for any warping of the optics.

A layout of the bench and its optics is given in Figure 3.1. The ASALT laboratory system follows a similar process as the AO system described in Section 2.2. The beam path on the optical table begins with a 1550 nm laser as the source. The beam is propagated through the atmospheric turbulence simulator (ATS) consisting of two phase wheels that are used to simulate the atmospheric conditions, which can be user-defined. The aberrated beam is then reflected off a SM in order to compensate for the tilt/tip in the beam. The DM then applies a high-order correction to the beam and is controlled by the DM controller. After reflecting off the DM, the beam is then projected through a set of beamsplitters to the SH WFS and self-referencing interferometer (SRI). The SRI is a WFS that can directly measure the phase, but in this research the SH WFS will be used to close the loop. The beam is focused and readjusted with the optics within this process to simulate a 1.5 meter AO system.

The DM that is used in the ASALT laboratory shown in Figure 3.2 has 729 actuators with 27 across the width of the aperture of the DM but only 481 actuators are actively controlled over a  $25 \times 25$  region. The controls to the DM are sent in a  $25 \times 25$  matrix of commands where each element is representative of an actuator position.

### *3.1.2 Unique Components.*

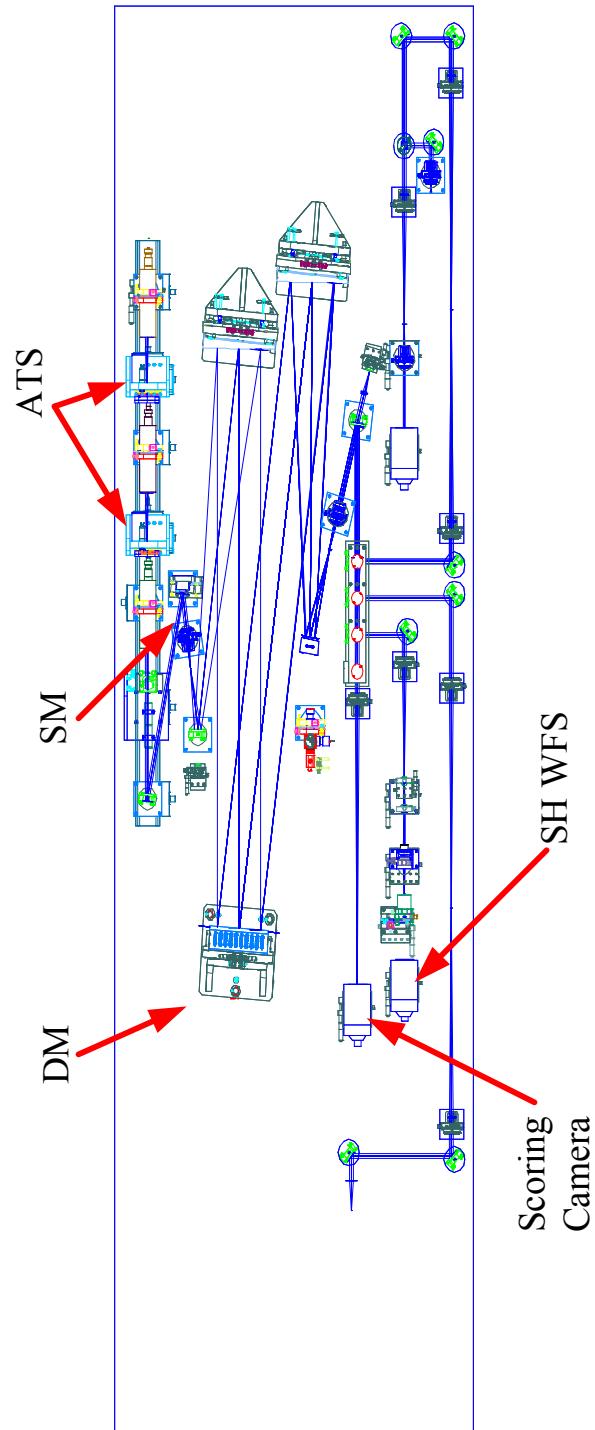


Figure 3.1: ASALT laboratory's optical table layout in SRI-2. [8]

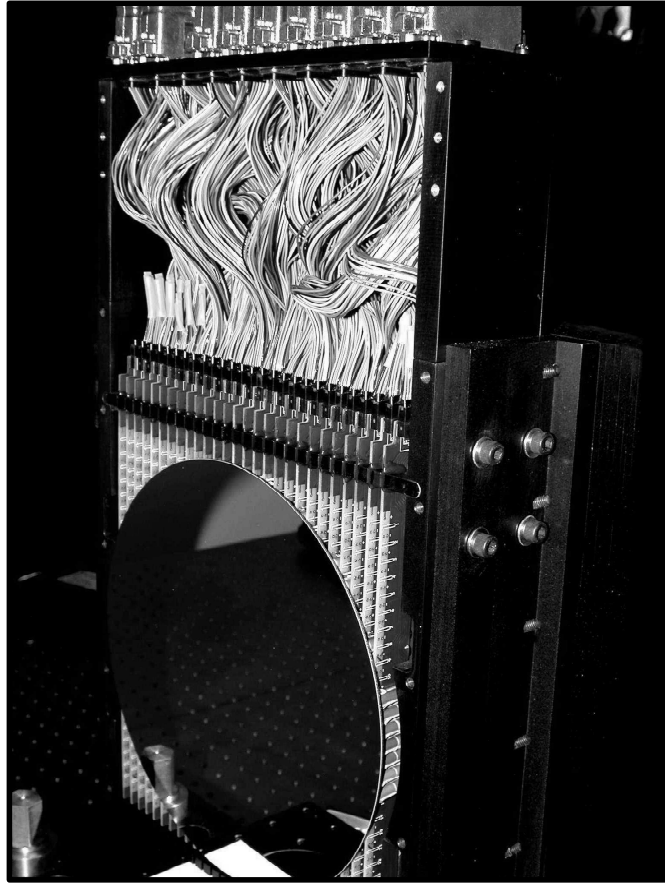


Figure 3.2: ASALT laboratory DM.



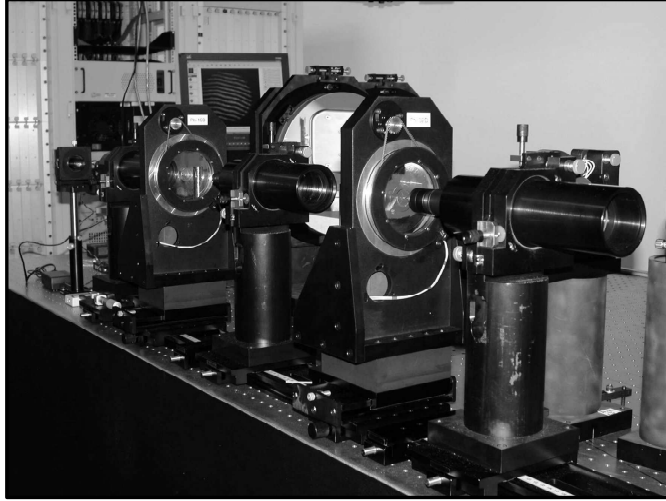


Figure 3.3: ATS phase wheels.

*3.1.2.1 Atmospheric Turbulence Simulator.* The ATS can be used to produce turbulent conditions by simulating an atmosphere with two phase wheels, as in Figure 3.3. Each static phase wheel is milled with a phase screen that is consistent with Kolmogorov statistics which can be rotated and repositioned to cover a variety of atmospheric conditions, as specified by Fried's parameter  $r_0$ , Greenwood frequency  $f_g$ , and the Rytov number. In areas where the beams are converging, the phase plates can be positioned for a particular magnitude of  $r_0$ . The Rytov number which is a measure of scintillation can also be configured to a particular condition by changing out the focal lens set that is used in the focal plane of each afocal system. Each lens set is representative of a different altitude of effective turbulence. The Greenwood frequency can be defined by adjusting the speed at which the phase wheels rotate. Stepper motors are used for mechanically rotating the phase wheels at a particular velocity and position which allows for a repetition of a given turbulence. [4]

*3.1.2.2 Reflective Memory.* The flexibility of the ASALT laboratory is due to the simplicity of the design and modular architecture of the hardware and software. Flexibility and simplicity were given higher priority than the given speed of the system. Each primary piece of hardware such as the DM and WFSs is given a separate computer for computation and control. Each computer has 128 MB of

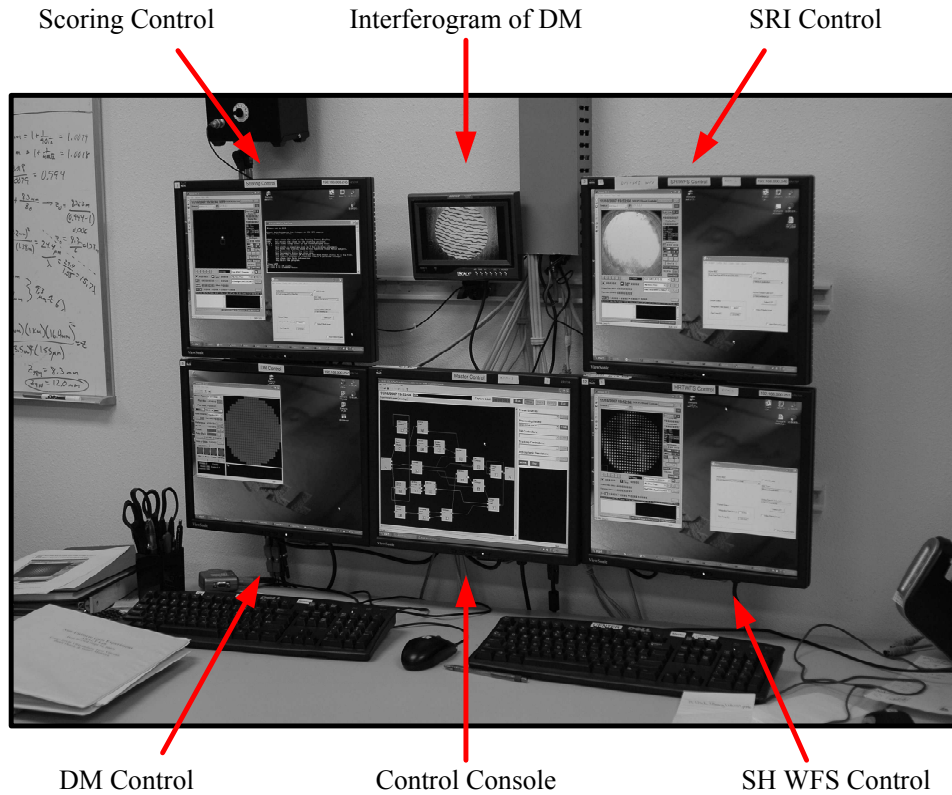


Figure 3.4: ASALT laboratory control computers.

reflective memory to pass information to one another. Reflective memory replicates the information on a given computer to the others in the system which adds to the integration. The API operates the reading and writing of this memory through library functions. [4]

*3.1.2.3 Control Computers.* The ASALT laboratory AO system uses five control computers to run and evaluate experiments on the bench as shown in Figure 3.4. The DM, scoring camera, SH WFS, and SRI are all assigned a computer for all of the primary tasks designated for each component. The center control console computer integrates the data from the other computers and executes the experiments on the bench in a layout form. The small screen above the control console displays an interferogram of the DM which can be used to diagnose its performance in real time.

*3.1.3 ASALT Initialization and Calibration.* Before carrying out experiments, the components are powered up and initialized. The light is blocked so that the sensor can record dark frames. Dark frames are subtracted from the camera images to remove the ambient light and dark current in the system. The DM is carefully turned on and loaded with a flatmap. The flatmap is a set of commands that flatten the DM's surface. The SH WFS is aligned by sending commands to the DM in particular configurations in order to find any misalignments to adjust for and be recorded. The ASALT laboratory also has the SRI which can be aligned at this point in the initialization of the bench. The beam is centered into the scoring camera by adjusting the steering mirror with a module. A track align layout is run to determine the  $x$ - $y$  offsets of the beam and are recorded. A reference layout is used to produce a WFS references file which is input into the Hartmann real-time reconstructor (RTR). The system is now ready for an experiment layout to be initialized and ran for data collection.

*3.1.4 Control Console Layout.* The control console used at the ASALT laboratory uses object-oriented programming to integrate the hardware into visual component blocks which can be seen in a graphical user interface (GUI), as shown in Figure 3.5(a). The entire layout of the experiment can be displayed in the control console with individual components displayed as blocks. The type of components are subdivided into five main types: Frame Sources, Processing Nodes, DM Controllers, Tracking Controllers, and Atmospheric Simulators. Some of these components such as the Frame Sources and DM controller have direct synchronization to the hardware on the bench such as the WFS cameras and DM, respectively. The reflective memory can retain the input and output of each of these blocks and can be recorded for later analysis.

Each experiment layout represents one entire process of a frame for the AO system, beginning with a Start node component and finishing with an End node component. The ASALT laboratory simulates the process of a real-time AO system

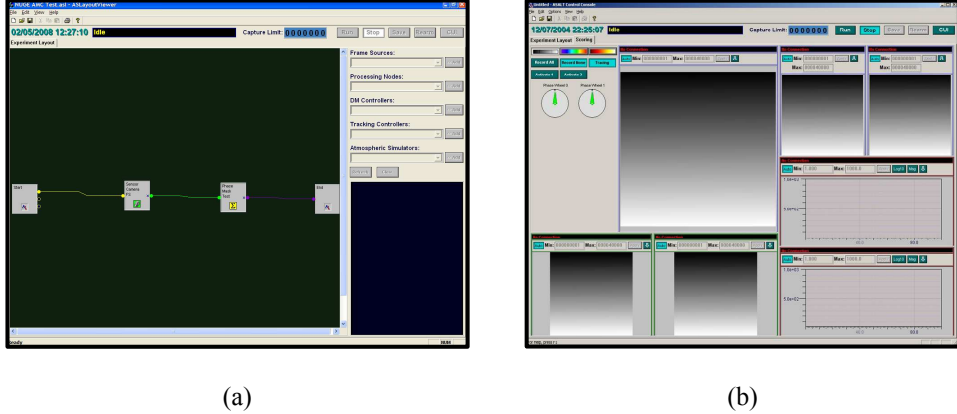


Figure 3.5: ASALT layout and control system data display. (a) Basic ASALT layout. (b) Control system data display.

by completing all of the processes between the Start and End node before it moves the turbulence with the ATS. This gives the capability of simulating different AO system speeds by scaling the data with different sampling frequencies. The activate control node turns on/off components at designated times such as the steering mirror and DM. The components can be connected to each other with graphical wires, though each has specific requirements that need be met for the types and number of inputs and outputs that are connected to it. Most of the components that integrate directly to the hardware are written in C++ programming language for speed considerations, yet can also be represented in Matlab<sup>®</sup>. Each of the component's code is accessible and can be altered making the entire system transparent and highly configurable. Processing Nodes can be developed in Matlab<sup>®</sup> and integrated as a component with your experimental layout. The input and output data are recorded in hierarchical data format (HDF). Though the data of the inputs/outputs of the components can also be examined during the operation of the AO system through the control system data display, as shown in Figure 3.5(b). The data display allows the user to examine user-defined data analyses and camera images in real-time.

*3.1.5 Primary AO Experimental Layout.* Each experiment on the AO system begins with the layout of the components comprising of the requirements of what

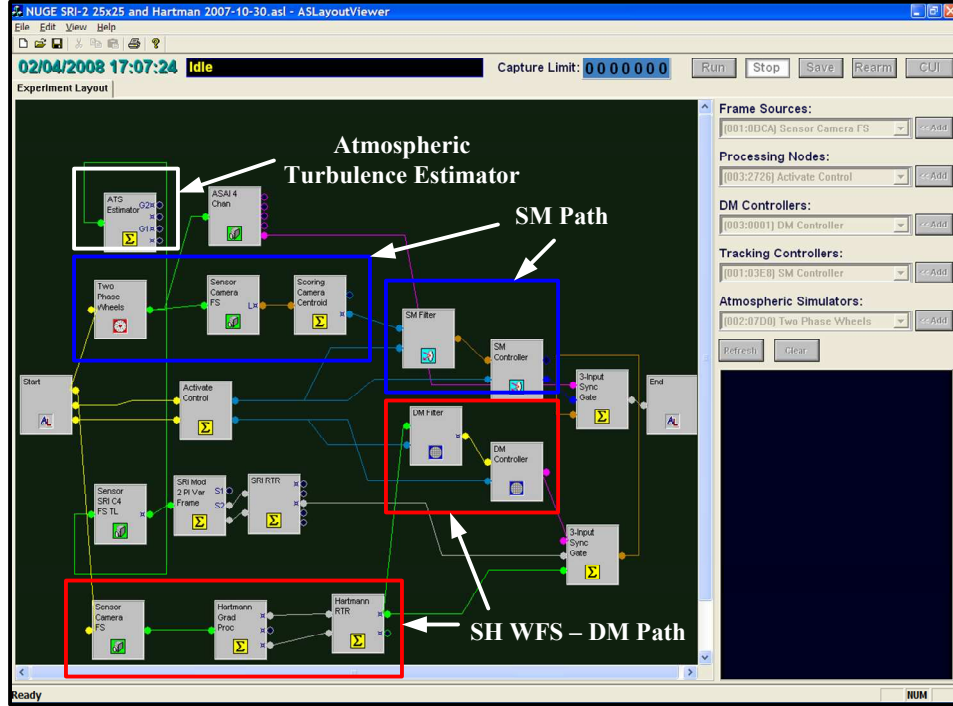


Figure 3.6: Primary layout. The blue boxed components is representative of the SM path, the red boxed components are representative of the SH WFS and DM path, and the white boxed component is the ATS estimator node.

is being tested. Figure 3.6 displays the layout that was developed for the majority of the experiments conducted.

*3.1.5.1 Steering Mirror Path.* This path, boxed in blue in Figure 3.6, is used to sense the tilt of the beam and control the SM. The path begins with the Start Node which initiates the two phase wheels. The two phase wheels output their position and status. The Sensor Camera block is then triggered depending upon the status of the phase wheels. The Sensor Camera outputs the frames of the beam after reflection off the DM. Frames are then fed into the Scoring Camera centroid block which uses a centroid algorithm to determine the centroid of the beam's focal spot. This offset of the centroid is input into the SM Filter which temporally filters the signal and produces commands to the SM Controller. The SM Controller outputs the position of the tilt mirror and is synchronized with the other signals using the 3-Input Sync Gate.

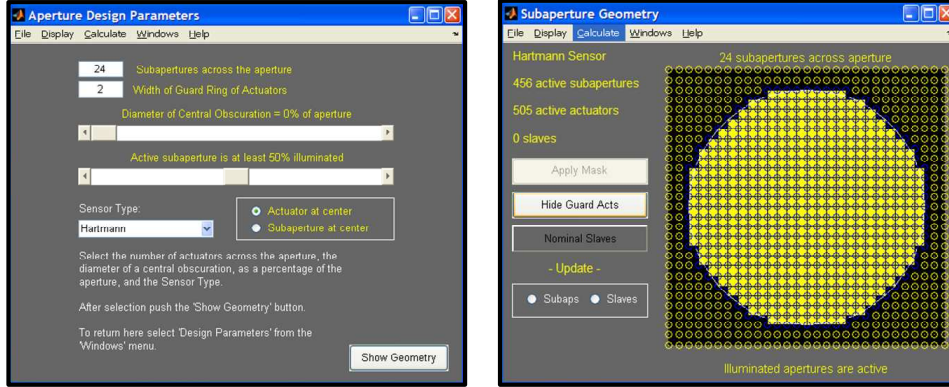
*3.1.5.2 SH WFS and DM Control Path.* This path, boxed in red in Figure 3.6, determines the slopes of the wavefront with the  $24 \times 24$  subaperture SH WFS and apply the commands to the DM. The Start Node is used to initiate a Sensor Camera block which outputs the frames from the Hartmann WFS Camera as a  $96 \times 96$  matrix. The frames are then input into the Hartmann Gradient Processor Node which calculates the gradients of the wavefront determined with the Fried Geometry and outputs two  $24 \times 24$  matrices of the  $x$  and  $y$  slopes, respectively. These gradients are then processed in the Hartmann RTR which applies the reconstruction matrix, estimating the phase as a  $25 \times 25$  matrix corresponding to each active actuator position of the DM. The DM Filter block temporally filters the phase using the lossy integrator gain  $a$  and filter gain  $b$ , in order to produce commands to the DM. The DM controller takes these commands from the DM Filter and actually applies them to the DM.

*3.1.5.3 ATS Estimator Node.* The ATS estimator, boxed in white in Figure 3.6, uses a look-up table to estimate the atmospheric conditions as a function of the phase wheel position, lens set, and speed of the phase wheels. The speed of the phase wheels is input into the ATS node as well as configuration items such as the lens set used and the output is the Fried parameter, Greenwood frequency, and Rytov number.

## **3.2 Lyapunov Stability Bounds**

A Lyapunov stability bounds test was conducted on an estimated geometry matrix and reconstructor for the configuration that was utilized in the ASALT laboratory. This analysis provides filter gain bounds that are determined by the error propagator equations used in Section 2.7.1, as shown again by

$$g_n = \frac{b^2}{N_a} \text{tr}[I - \mathbf{F}^T \mathbf{F}]^{-1} \mathbf{M} \mathbf{M}^T, \quad (3.1)$$



(a)

(b)

Figure 3.7: AOTools subaperture dialog.

where  $b$  is the servo-loop gain,  $\mathbf{M}$  is the reconstructor,  $\mathbf{F} = a\mathbf{I} - b\mathbf{M}\mathbf{A}$ ,  $a$  is the lossy integrator gain,  $\mathbf{I}$  is the identity matrix, and  $N_a$  is the number of controlled actuators in the pupil.

*3.2.1 Production of Reconstructor and Geometry Matrix.* The actual reconstructor  $\mathbf{M}$  and geometry matrix  $\mathbf{A}$  in the ASALT laboratory were not readily available, therefore were developed using an AOTools dialog box in Matlab<sup>®</sup> called `subapdlg`, as shown in Figure 3.7.

The ASALT laboratory hardware characteristics were used as the parameters input into the dialog. The reconstructor matrix  $\mathbf{M}$  was produced in `subapdlg` with no slaving, to produce the most conservative bounds to  $b$ . The ASALT laboratory's DM has 27 actuators across its diameter but only 25 are actively used. The outer unused actuators can be used for slaving to the outer active actuators. The active actuators are configured to form 24 subapertures across the aperture in the Fried geometry. Therefore, `subapdlg` was set for 24 subapertures across the aperture with a 1 actuator guard ring. The SH WFS was initialized to the Hartmann sensor type in order to correspond with the ASALT laboratory setup. The `subapdlg` is then used to calculate the reconstructor matrix  $\mathbf{M}$  and the geometry matrix  $\mathbf{A}$  with a pull down menu. The matrices are then saved into the workspace in Matlab<sup>®</sup>.

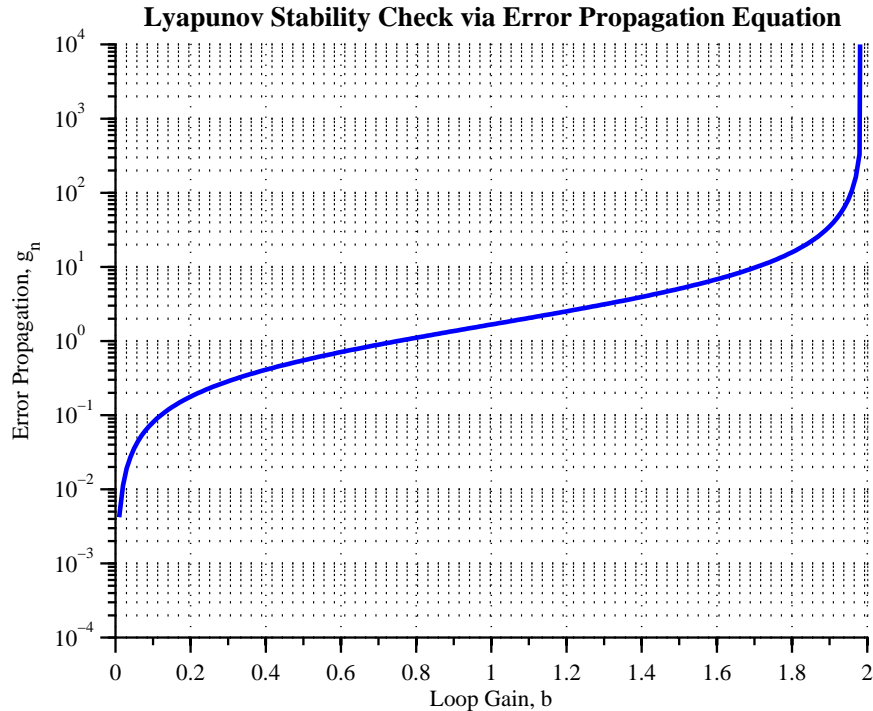


Figure 3.8: Error propagator.

*3.2.2 Filter Gain Bounds.* Therefore using `subapdlg` to produce  $\mathbf{M}$  and  $\mathbf{A}$ , the error propagator  $g_n$  was evaluated in a Matlab<sup>®</sup> script to produce Figure 3.8. Error propagator  $g_n$  diverges at the servo-loop gain  $b$  values of 0 and 2. At these given gain values, Lyapunov stability no longer holds because the solution of  $\mathbf{P}$  from Eq. (2.37) no longer remains positive definite. Using the Lyapunov stability analysis gives a bounds as to what values of  $b$  would be reasonable for use in the following experiments. Thus the extreme bounds of the servo-loop gain  $b$  should be within  $0 < b < 2$ .

### 3.3 Slope Measurement Sensitivity Experiment

*3.3.1 Motivation.* The SMSE explores the errors of the SH WFS discussed in Section 2.4.2, particularly the non-uniform focal spot errors and low SNR effects over the edge subapertures. Noisy slope measurements can cascade to errors in the control of the corresponding actuators of the DM. Therefore, these particular effects



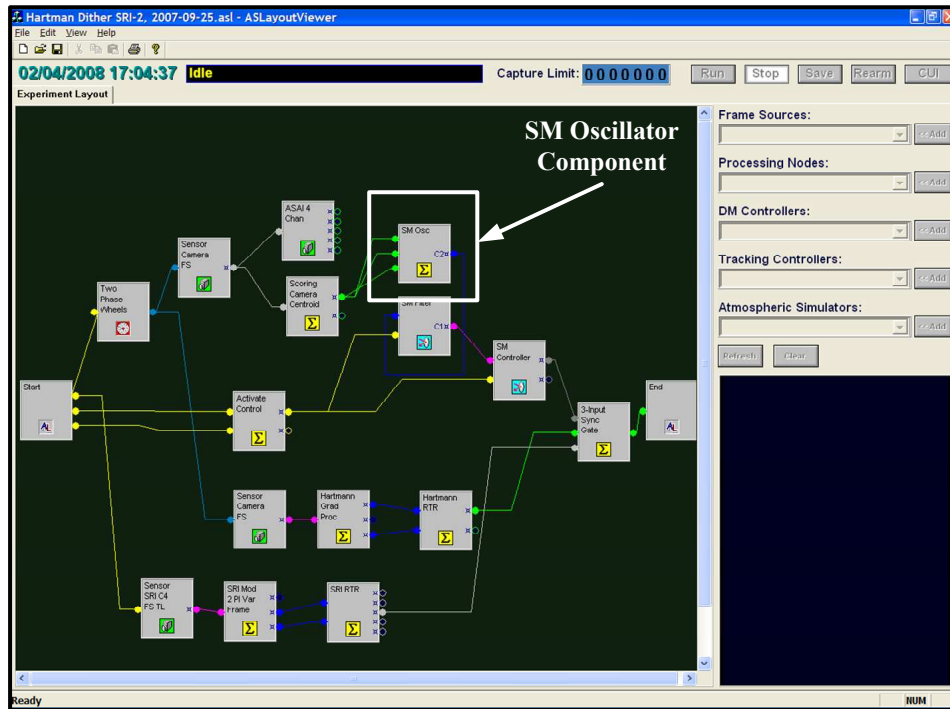


Figure 3.9: SH WFS measurement layout.

on the edge subaperture slope measurements are important to characterize in order to identify the need to compensate for them with the control of the actuators.

*3.3.2 Slope Measurement Experiment Design.* In this experiment the SM is commanded to oscillate, applying tilt to the beam which is measured by the SH WFS. A comparison of the recorded slope measurements versus the commands is taken of each subaperture. The beam is slewed across the scoring camera using a pre-made SM Oscillator Processing component which is specifically used to command the SM in an oscillatory pattern. The SM is commanded to provide enough tilt to fully evaluate the dynamic range of tilt measurement capabilities of the SH WFS.

*3.3.2.1 Layout Design for SMSE.* The layout for the SMSE is primarily the same structure as the layout in Section 3.1.5. Though, with this experiment there is no need for the control of the DM, because the SM is the only mirror that needs to be commanded. Therefore the DM is initially commanded to be flat and is

no longer manipulated during the experiment. A new node called the SM Oscillator component is connected between the Scoring Camera Centroid and the SM Filter, given in Figure 3.9. The SM Oscillator can command the shift in the focal-plane position of the centroid  $(\Delta x_i, \Delta y_i)$  given the following relationship

$$\Delta x_i = A_{xs} \sin\left(\frac{2\pi k}{dx}\right) + A_{xc} \cos\left(\frac{2\pi k}{dx}\right) + x, \quad (3.2)$$

$$\Delta y_i = A_{ys} \sin\left(\frac{2\pi k}{dy}\right) + A_{yc} \cos\left(\frac{2\pi k}{dy}\right) + y, \quad (3.3)$$

where  $A_{xs}$ ,  $A_{ys}$ ,  $A_{xc}$ ,  $A_{yc}$  are the oscillation amplitudes,  $dx$  and  $dy$ , determine the speed of the oscillations,  $x$  and  $y$  are the offsets, and  $k$  is the angular wavenumber.

*3.3.2.2 SMSE Condition Parameters.* The parameters given in Table 3.1 are configured over the AO system for this particular experiment. No turbulence is used over this experiment in order to isolate the performance of the SH WFS tilt measurements. Therefore, the AO system operates in open-loop because there are no corrections needed during the experiment. Table 3.2 gives the configuration of the SM Oscillator Component in order to command the SM to provide tilt for the SH WFS to measure. The sinusoidal amplitudes  $A_{xs}$  and  $A_{ys}$  are at a large enough magnitude to tilt the beam across the scoring camera pupil. The period of the sinusoidal commands, defined by  $dx$  and  $dy$ , are set at a long enough time step in order to gain enough samples in the measurements over the dynamic range of tilt. The other parameters not given in Table 3.2 are set to zero in order to implement a purely sinusoidal tilt command over the SM.

Table 3.1: SMSE system parameters.

Parameter	Value
Laser Power ( $\mu\text{W}$ )	2
Laser Wavelength ( $\mu\text{m}$ )	1.55
Number of Frames	2000
SM Loop	Open
DM Loop	Open

Table 3.2: SM oscillator component parameters.

Parameter	$x$ -dither value	$y$ -dither value
$A_{xs}$	6	0
$A_{ys}$	0	6
$dx$	90	0
$dy$	0	90

*3.3.2.3 SMSE Experimental Process.* Once the AO system is turned on and calibrated, the layout is initialized in the control console. The parameters given in Table 3.1 are input into the SM oscillation component and the number of frames to be taken are set in the control console. Two data runs are taken over the AO system, one for the SH WFS measurements of the  $x$ -tilt, and the other for the  $y$ -tilt.

### 3.4 Analysis of Slaving Effects Experiment

*3.4.1 Motivation.* The ASEE explores the effects of slaving the actuators as compared to non-slaved actuator configurations. Section 2.7.2 discusses how slaving of the actuators has a direct correspondence to the stability of the system. Slaving prevents ridging between controlled and uncontrolled actuators over the edges. Therefore, this analysis is important for understanding how slaving affects the edge actuator responses corresponding to the overall stability/performance of the AO system.

*3.4.2 Slaving Experiment Design.* The AO system was closed with the SH WFS under a moderate turbulence condition set by positioning the phase wheels and setting parameters into the ATS. The experiment was conducted with the actuators slaved and non-slaved. Under each scenario, the filter gain  $b$  was varied to investigate how the DM filter affected the performance of the AO system under the different slaving conditions.

*3.4.2.1 Layout Design for ASEE.* The layout for this experiment has the same structure as the layout shown in Section 3.1.5. The Hartmann RTR

Table 3.3: ASEE system parameters.

Parameter	Value
Laser Power ( $\mu\text{W}$ )	2
Laser Wavelength ( $\mu\text{m}$ )	1.55
Number of Frames	500
SM Loop	Closed
DM Loop	Closed

component can be configured for the activation of slaving the edge actuators. The DM Controller component evaluates the flag sent from the Hartmann RTR component and implements the actual commands sent to the DM for slaving.

The ATS is configured in the layout to simulate a moderate turbulence. The speed of the high and low turbulence phase wheels are set with step sizes of 5 and 7, respectively. The configuration block of the ATS is set to 17092 steps per revolution for each phase wheel.

*3.4.2.2 ASEE Condition Parameters.* The parameters given in Table 3.3 are configured over the AO system for this particular experiment. The experiment was run with lens set 23 under moderate turbulence conditions given in Table 3.4. The AO system’s DM and SM loops are closed in order for the AO system to mitigate for the turbulence.

*3.4.2.3 ASEE Experimental Process.* The AO setup is turned on and calibrated in order to open the experiment layout for the analysis of slaving conditions. Moderate turbulence conditions shown in Table 3.4 were setup by moving the phase wheels and setting the given speeds in the Phase Wheel component. The slaving experiment runs were taken in two main batches corresponding to varying the  $b$  gain in the cases of slaved actuators and non-slaved actuators, given by Table 3.5. The  $b$  gains are varied from 0.05 to 0.85 in steps of 0.1, which covers the general operating range of usable filter gains.

Table 3.4: ASEE turbulence condition.

Turbulence Condition					
Turbulence Level	Phase Wheel Positions		Phase Wheel	$r_0$	$f_g/f_s$
	High (cm)	Low (cm)	Step Size (low/high)	(cm)	
Moderate	51	104	5/7	11.836	0.08259

Table 3.5: Table of slaving experiments.

Batch	Turbulence	DM Filter		Slaving
		$a$ gain	$b$ gain	
1	Moderate	0.99	0.05-0.85 $\Delta$ 0.1	No
2	Moderate	0.99	0.05-0.85 $\Delta$ 0.1	Yes

### 3.5 Non-Uniform Gain Experiment

*3.5.1 Motivation.* The Non-Uniform Gain Experiment (NUGE) takes into account the prior two experiments that revealed how the edge actuators affect the overall performance of the AO system. As mentioned in Section 2.2.1.2, the SOR uses the same uniform filter gain  $b$  on all of the actuators across the DM which does not take into account these edge effects. But in this experiment, spatially varying gain maps in the DM filter are used to adjust the bandwidths over the edge actuators by having different filter gains  $b$  over these specific regions.

*3.5.2 Gain Map Design and Turbulence Conditions.* The prior two experiments of the SH WFS and the slaving effects of the DM are used to analyze the different responses of the AO system over the aperture. Errors and instabilities caused by edge effects over the SH WFS and DM give reason to explore mitigation techniques to address them. Non-uniform gain maps are constructed for experimentation in this research in order to compare their performance with respect to traditional uniform gain methods.

*3.5.2.1 DM Filter Analysis.* The DM Filter component is composed of code that operates the command law mentioned in Section 2.6.1 and is shown again

below in the  $z$ -domain

$$c(z)z = ac(z) + be(z)z \implies F(z) = \frac{e(z)}{c(z)} = \frac{bz}{z - a}. \quad (3.4)$$

where  $c(z)$  is a command to the DM,  $a$  is the lossy integrator gain,  $b$  is the filter gain,  $e(z)$  is the residual phase, and  $F(z)$  is the transfer function of the digital filter. The lossy integrator gain  $a$  is normally set to  $a \approx 1$ , but not exactly one in order to take into account unsensed modes. An example plot of the magnitude of the DM filter's transfer function  $|F(z)|$  is shown in Figure 3.10. The frequency shows that the digital filter acts as a high pass filter and is in the form of a PID controller. In the low frequencies,  $|F(z)|$  has a low magnitude signifying that the DM commands have a low gain applied to them. Whereas in high frequencies,  $|F(z)|$  has a larger magnitude signifying that the DM commands have a higher gain in this regime. Therefore given fast moving turbulence the DM filter would produce commands with a high gain in order for the actuators to be quick enough to move with the disturbance, while in low frequencies the commands have low gain for slower moving disturbances.

Lowering the filter gain  $b$  would decrease the overall gain of the plot in Figure 3.10. Specifically, if the filter gain  $b$  is lowered the actuator commands in the high frequency regime could be dampened. If the SH WFS has noise prone regions which have a great deal of high frequency content, this would produce corrupted DM commands. By lowering the filter gains  $b$  in these specific regions the response in these areas will be dampened.

*3.5.2.2 SNR of Detector Array.* The SH WFS does not have uniform illumination over all of the subapertures of its detector array. Particularly, the subapertures located on the edge of the sensor are prone to less light, as mentioned in Section 2.4.2.4. Therefore the SNR differs spatially over the detector array of the SH WFS, as given in Figure 3.11. Figure 3.11 shows the average SNR using 500 frames of the SH WFS camera illuminated with a  $2.0\mu\text{W}$  laser. The average SNR over the edge subapertures is 48.81, while the center fully illuminated subapertures have an

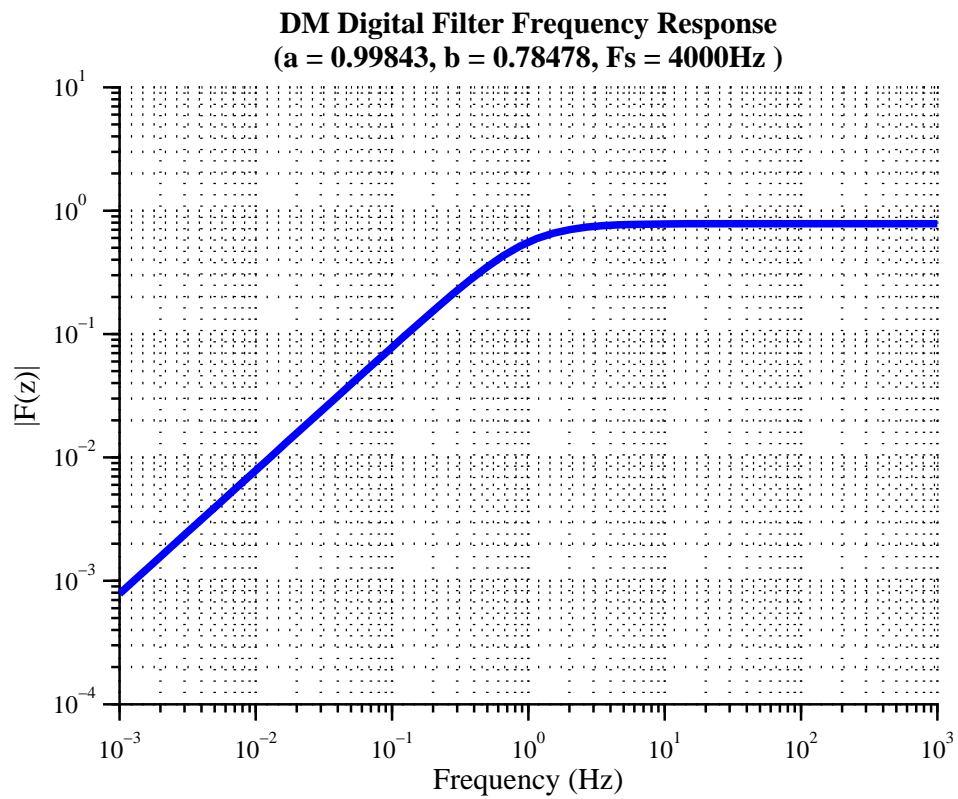


Figure 3.10: Example of frequency response of  $F(z)$ .

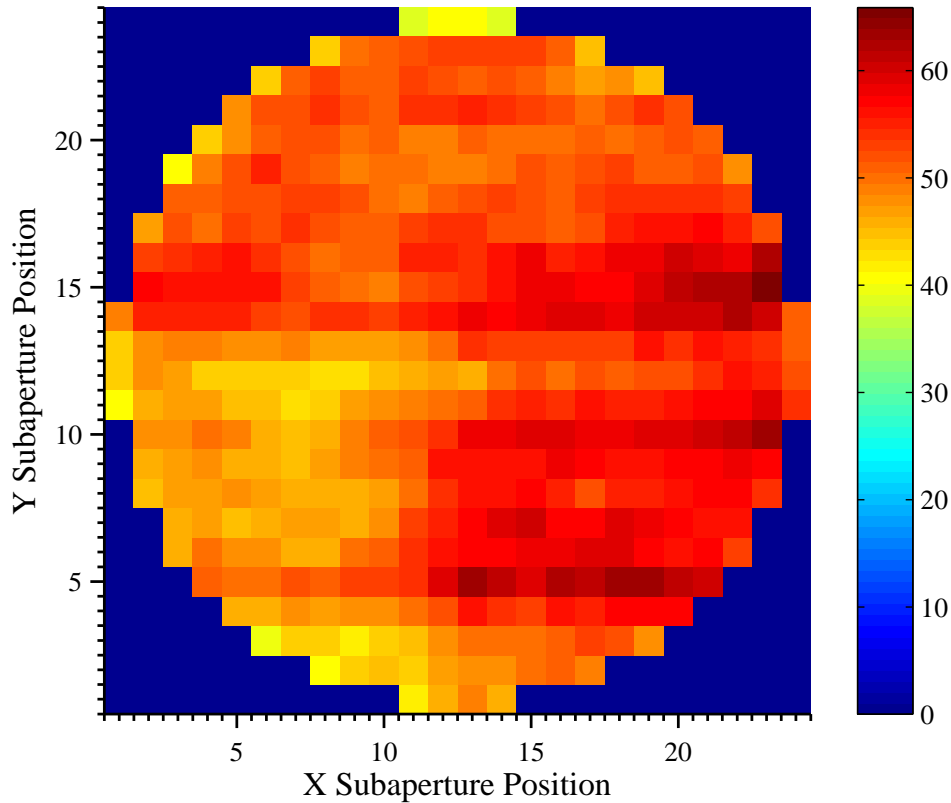


Figure 3.11: SNR over a SH WFS detector array.

average SNR of 52.60, using Eq. (2.17). Therefore, the edge subapertures are more prone to measurement errors given Eqs. (2.18) and (2.19), than the fully illuminated center subapertures of the detector array.

*3.5.2.3 Gain Map Design.* Three different gain maps shown in Figure 3.12 are constructed in this research and are specifically designed to address the areas of the edge effects over the SH WFS and DM. All of the gain maps were designed to have lower gains on the edge subapertures than the inner subapertures. The prior two experiments evaluating the SH WFS measurements and DM showed that the edge subapertures had more errors in their slope measurements. This causes instabilities to begin on the edges. Therefore the edge gains were given lower values than the center subapertures in order to place less emphasis on their measurements.

The DM filter can be considered a  $25 \times 25$  array of SISO filters corresponding



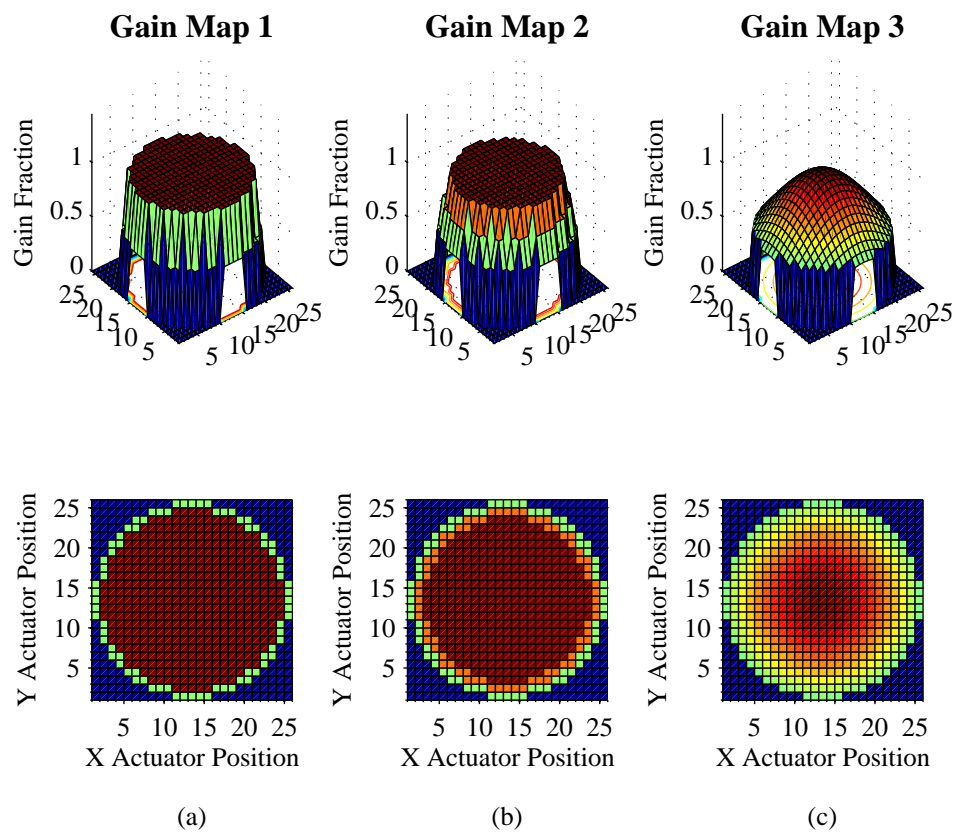


Figure 3.12: Non-uniform gain maps.

to each active actuator position. With uniform filter gains, each of these SISO filters have all of the same parameters. Though by replacing the uniform gain  $b$  in Eq. (2.29) with a  $25 \times 25$  matrix  $\mathbf{b}$ , each actuator location can be defined with different gain parameters.

Gain map 1 was designed to address the subapertures that were found to have low SNR over the edges. Therefore a ringed design was developed, covering the outer edge of circular aperture only. The inner subapertures still maintained a uniform filter gain  $b$ . The edge gains were experimented over different fractions of the inner gains. For example, if the inner gain  $b = 0.5$  and the edge gain was designated to have 0.8 of that value, then the outer edge filter gains would be  $b = 0.4$  for this map.

Gain map 2 was designed in a similar fashion as gain map 1, yet also addressed the next inner ring of actuators. Though the second outer ring of actuators are weighted as a fraction of the inner and outer edge gains. The next inner ring of actuators is an average of the fraction of the edge and the center gains. For example, if the inner gain  $b = 0.5$  and the outer edge gain was designated as 0.8 of that value, then the outer edge gain would  $b = 0.4$ . The next inner ring would be the average between a uniform gain fraction of 1.0 and the outer ring fraction of 0.8 and thus be a fraction of 0.9. Therefore the next inner ring of gains would have a value of  $b = 0.45$ .

Gain map 3 was designed with a Gaussian profile for a smoother transition in filter gain  $b$  from the center to edge subapertures. The Gaussian form of the gain map is designed to address the illumination of a beam with a Gaussian profile. A 2-D Gaussian relationship for the map is given by

$$f(x, y; \sigma, c) = e^{\frac{-(x-c)^2 - (y-c)^2}{2\sigma^2}}, \quad (3.5)$$

where  $(x, y)$  is the element position in the gain map,  $c$  is mean value at the center position of the Gaussian distribution, and  $\sigma$  is the standard deviation for the curve. The values to develop the Gaussian map were the center  $b$  gain and the desired edge fraction of that gain. A  $\sigma$  value for the curve is found using those two parameters as

Table 3.6: NUGE turbulence conditions.

Turbulence Conditions						
Turbulence Level	Phase Wheel Positions		Phase Wheel	$r_0$ (cm)	$f_g/f_s$	
	High (cm)	Low (cm)	Step Size (low/high)			
Low	54	107	1/3	22.08	0.0240	
Moderate	51	104	5/7	11.84	0.0826	
High	49	102	7/9	9.03	0.1125	

constraints given by

$$\sigma = \sqrt{\frac{-(x_{edge} - c)^2 - (y_{edge} - c)^2}{2\ln(frac_{edge})}}, \quad (3.6)$$

where  $(x_{edge}, y_{edge})$  is the element position of an edge actuator in the gain map, and  $frac_{edge}$  is the fraction of the center  $b$  gain that is used for the edge gains.

#### 3.5.2.4 NUGE Turbulence Conditions.

The turbulence conditions were chosen to cover a wide variety of scenarios. Each subsequent turbulence condition starting from the Low condition to the High condition is an increase in the turbulence strength. The phase wheel locations on the bench are moved to change  $r_0$  and the phase wheel speeds are adjusted to change  $f_G$ . The phase wheel speeds are a function of the step size set in the configuration of the ATS component. The number of steps per revolution in these experiments was 17092 for each phase wheel. The turbulence conditions used in these experiments are given in Table 3.6.

*3.5.3 NUGE Experiment Design.* The application of spatially varying gain maps is examined in two specifically different cases. The first examination is to explore any increase in the performance of the AO system with the application of the spatially varying gain maps in comparison to the standard uniform gains that are used in the DM Filter. The second examination looks into mitigating instabilities on the edges in regimes where they occur within the AO system.

The layout used for the NUGE experiment has the same structure as the primary layout shown in Section 3.1.5 except that the DM filter component is replaced with a newly designed NUGE DM Filter. The same structure as the DM Filter was

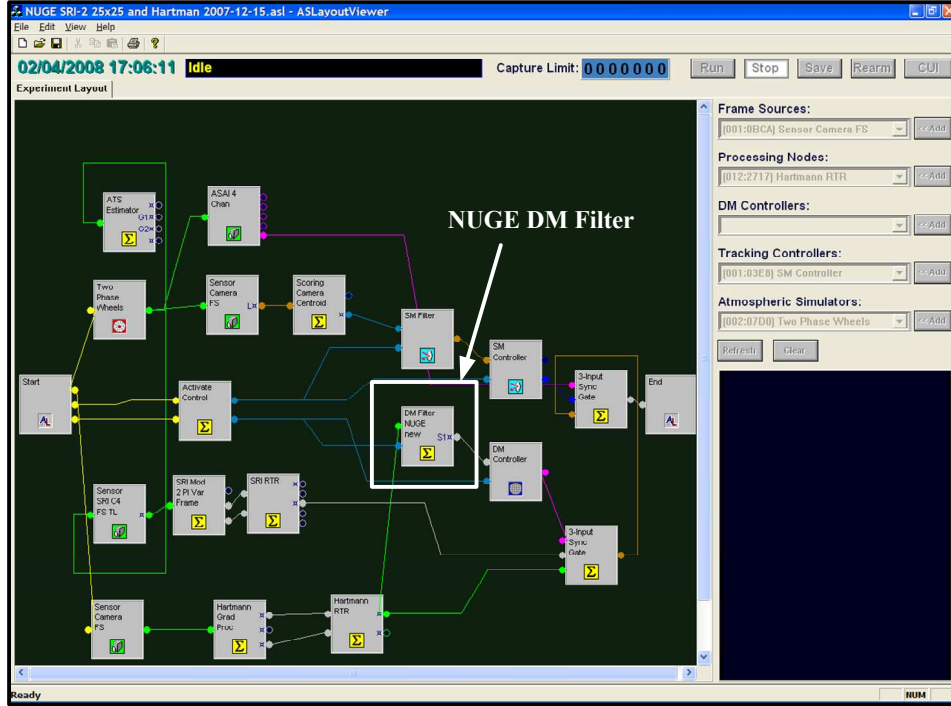


Figure 3.13: NUGE control software layout.

used for the NUGE DM Filter except the code was written in Matlab<sup>®</sup> rather than C++. The NUGE DM filter was redesigned to accept  $25 \times 25$  gain maps that can be adjusted in the configuration box in the control console, as shown in Figure 3.13.

A baseline is set for the NUGE experiments by testing each of the turbulent conditions using the standard uniform gain coefficients, given in Table 3.7. The optimal uniform  $b$  gain for each turbulence case is found by examining the data from the AO system in the baseline cases and then compared with the performance of those same conditions using spatially varying gain maps.

The NUGE experiment evaluated the response of the system in the cases when

Table 3.7: Table of baseline uniform gain experiments.

Batch	Turbulence	DM Filter	
		$a$ gain	$b$ gain
1	Low	0.99	0.05-0.85, 0.90 $\Delta 0.1$
2	Moderate	0.99	0.05-0.85, 0.90 $\Delta 0.1$
3	High	0.99	0.05-0.85, 0.90 $\Delta 0.1$

Table 3.8: NUGE system parameters.

Parameter	Value
Laser Power ( $\mu\text{W}$ )	2
Laser Wavelength ( $\mu\text{m}$ )	1.55
Number of Frames	500
SM Loop	Closed
DM Loop	Closed

Table 3.9: Table of NUGE experiments.

Batch	Turbulence	NUGE DM Filter			
		$a$ gain	$b$ gain	$b$ gain edge fraction	Gain Map
1	Low	0.99	0.55-0.85, 0.90 $\Delta$ 0.1	0.50-1.00 $\Delta$ 0.1	1
2	Low	0.99	0.55-0.85, 0.90 $\Delta$ 0.1	0.50-1.00 $\Delta$ 0.1	2
3	Low	0.99	0.55-0.85, 0.90 $\Delta$ 0.1	0.50-1.00 $\Delta$ 0.1	3
4	Moderate	0.99	0.55-0.85, 0.90 $\Delta$ 0.1	0.50-1.00 $\Delta$ 0.1	1
5	Moderate	0.99	0.55-0.85, 0.90 $\Delta$ 0.1	0.50-1.00 $\Delta$ 0.1	2
6	Moderate	0.99	0.55-0.85, 0.90 $\Delta$ 0.1	0.50-1.00 $\Delta$ 0.1	3
7	High	0.99	0.55-0.85, 0.90 $\Delta$ 0.1	0.50-1.00 $\Delta$ 0.1	1
8	High	0.99	0.55-0.85, 0.90 $\Delta$ 0.1	0.50-1.00 $\Delta$ 0.1	2
9	High	0.99	0.55-0.85, 0.90 $\Delta$ 0.1	0.50-1.00 $\Delta$ 0.1	3

instabilities were experimentally found to occur along the edges of the DM. Therefore the center filter gain values  $b$  that were set for these experiments were above  $b = 0.55$ . Examining the AO system in high gain  $b$  regimes allows for the analysis of mitigation techniques to compensate for the high residual phase variance over the edges. The experiments given in Table 3.9 are combinations of different  $b$  gains, gain maps, and turbulence levels. The parameters given in Table 3.8 are configured over the AO system for these particular experiments.

*3.5.4 Low SNR Experiment Design.* This experiment tests the use of gain maps in a lower SNR regime over the entire AO system. This analysis explores conditions in which the reference such as a LGS might have less than ideal irradiance. These conditions are more susceptible to noise as mentioned in Section 2.4.2.4. The laser power used for the source was lowered from  $2.0\mu\text{W}$  to  $0.2\mu\text{W}$  using a single-mode attenuator shown in Figure 3.14. The system parameters of the the low SNR

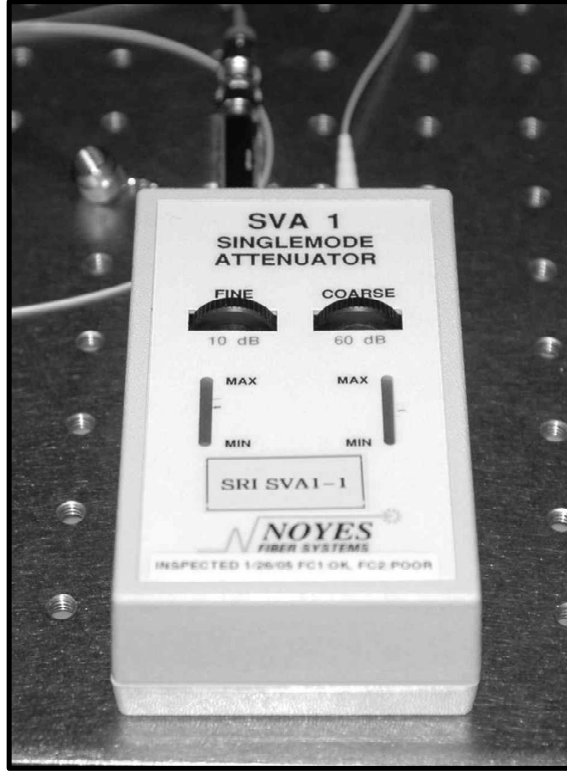


Figure 3.14: Laser attenuator.

experiment are given in Table 3.10. The experiment was run using the same layout as the NUGE experiment under the moderate turbulence condition. Each of the gain maps were tested with varying  $b$  gains shown in Table 3.11.

These experiments are used for comparison between the performance of the AO system in high SNR versus low SNR regimes. The evaluation in the low SNR regimes allows for analysis of how spatially varying gain maps perform within these cases. Because the SNR is low within these regimes, noise is much more of a factor in the calculation for the commands to the DM. Therefore, in this environment the AO system will be much more conducive for establishing instabilities on the edge actuators. Spatially varying gain maps are used to specifically address these edge areas so the maps have a larger opportunity to improve the performance of the AO system because the noise is more influential.

Table 3.10: Low SNR system parameters.

Parameter	Value
Laser Power ( $\mu\text{W}$ )	0.2
Laser Wavelength ( $\mu\text{m}$ )	1.55
Number of Frames	500
SM Loop	Closed
DM Loop	Closed

Table 3.11: Table of low SNR experiments.

Batch	Turbulence	NUGE DM Filter			Gain Map
		$a$ gain	$b$ gain	$b$ gain edge fraction	
1	Moderate	0.99	0.55-0.85, 0.90 $\Delta$ 0.1	0.50-1.00 $\Delta$ 0.1	1
2	Moderate	0.99	0.55-0.85, 0.90 $\Delta$ 0.1	0.50-1.00 $\Delta$ 0.1	2
3	Moderate	0.99	0.55-0.85, 0.90 $\Delta$ 0.1	0.50-1.00 $\Delta$ 0.1	3

## IV. Results and Data Analysis

This chapter provides the data results and analysis of the experiments taken in Chapter III. SMSE investigates the edge effects over the SH WFS when measuring the gradients of a wavefront. Low SNR and elongated focal spots can induce errors in the gradient measurements along the edge of the sensor array. The effects of slaving the actuators is also investigated by comparing the AO system's performance with and without slaving. These two experiments are conducted in order to gain insight into the importance of the edge effects relative to the AO system's performance.

Spatially varying gain maps are then used on the AO system in order to compensate for the edge effects and compare their performance to the standard usage of uniform filter gains  $b$  in closed-loop operation. The AO system is then tested with a decreased power in the laser source in order to investigate the system in the low SNR regime with spatially varying gain maps. Lastly, the AO system is driven to instabilities that simulate the waffling mode seen at the SOR's 3.5 meter telescope to seek a mitigation technique using the non-uniform gain maps.

### *4.1 SH WFS Slope Measurement Sensitivity Results and Analysis*

The SH WFS measures the local gradients of a wavefront which are reconstructed into phases at actuator positions. This experiment placed a known tilt over the SH WFS by commanding the SM over an open-loop system to test only the measurement capability of the sensor. The gradient data is taken from the Hartmann Gradient Processing Component in the layout of the experiment. Therefore the data is received in two  $24 \times 24$  matrices of  $x$  and  $y$  gradients, where each element corresponds to a subaperture of the SH WFS. As mentioned in Section 3.3.2, the SM is dithered so that the reference beam is slewed across the scoring camera in the  $x$  and  $y$  direction to analyze the SH WFS measurements of tilt. The SM is assumed to place the same amount of tilt over the entire array of the SH WFS. Therefore if the sensor was ideal, the same amount of tilt would be recorded over each subaperture.

The SM is sent commands of -0.07 volts to +0.07 volts using the SM Oscillator



component, which oscillates the mirror in the  $x$  and  $y$  direction providing tilt over the wavefront which is then measured by the SH WFS. Figure 4.1 is a plot of the measured  $x$ -tilt from the SH WFS versus the tilt commands sent to it, where a center and middle subaperture are compared with one another. The center subaperture is located in the (12,12) element of the  $24 \times 24$  matrices, while the middle subaperture tested was in the (6,6) element. These particular elements within the SH WFS are given as examples to show a given response of an individual subaperture located at different locations over the sensor array. The center and middle locations are fitted with a first order polynomial within their linear regions showing similar slope measurements versus tilt commands of  $204.49 \mu\text{rad}/\text{V}$  for the center subaperture and  $206.41 \mu\text{rad}/\text{V}$  for the middle subaperture given in Table 4.1. Both curves saturate at roughly  $\pm 8 \mu\text{rad}$  of measurable tilt. The reason the measurements saturate is that the focal spot corresponding to each subaperture lies fully within one-half of the quadcell due to the tilt. Therefore using the energy imbalance equations given in Eqs. (2.15) and (2.16), the slope measurements would remain the same if the centroid is fully within a cell. There is a small dip in magnitude of the tilt measurement at  $\pm 8 \mu\text{rad}$  after continuing to command the SM with more tilt because the centroid is beginning to exit the quadcell all together providing erroneous values of tilt. Though in most applications the measurable tilt never reaches the saturation points and stays within the linear region of each gradient response.

Figure 4.2 shows similar slope measurements when the centroid was slewed to measure the  $y$ -gradient responses of the same center and middle subapertures used in analyzing the  $x$ -gradient response. The  $y$ -gradient slopes are found to be very similar to the  $x$ -gradient slopes, where the center subaperture within the linear region has a measurable tilt versus command slope of  $203.30 \mu\text{rad}/\text{V}$  and the middle subaperture has a slope of  $203.27 \mu\text{rad}/\text{V}$ . Both the  $x$ -gradient and  $y$ -gradient responses have similar curve fits with slopes of approximately  $200 \mu\text{rad}/\text{V}$  within their respective linear regions. This result indicates that the centroids of the given center and middle subapertures are symmetrical in the  $x$  and  $y$  direction due to similar responses.

The center subaperture (12,12) gradient measurement response is compared with an edge subaperture located at the element (11,24) given in Figures 4.3 and 4.4. The  $x$ -gradient linear fit slope is found to be  $166.89 \mu\text{rad}/\text{V}$  at the edge subaperture as compared to the center subaperture slope of  $204.49 \mu\text{rad}/\text{V}$ . While the  $y$ -gradient linear fit slope has a value of  $212.79 \mu\text{rad}/\text{V}$  for the edge subaperture and a center subaperture slope of  $203.30 \mu\text{rad}/\text{V}$ . The  $x$ -gradient linear fit slope shows a large difference between the center and edge subaperture slope measurements. This indicates that the centroid is non-uniform as mentioned in Section 2.4.2.3, which explains the difference between the  $x$ -gradient and  $y$ -gradient measurements within the edge subaperture. The SNR over the edge subaperture is measured to be 39.04 using Eq. (2.17) as compared to the SNR of 47.29 over the center subaperture. Eqs. (2.18) and (2.19) show that lower SNR values induce more error in the measurements.

4.1.1 *Summary of the SH WFS measurement experiment.* The low illumination and non-uniform centroid spots of edge subapertures contribute errors to the measurements of the gradients, which in turn provide error-prone commands to the

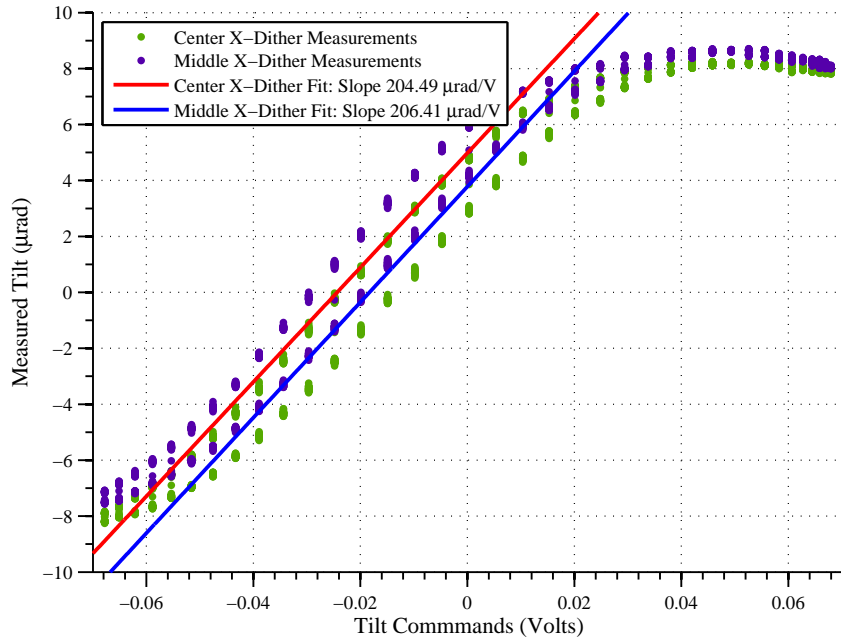


Figure 4.1: Center vs. middle  $x$ -gradient response.

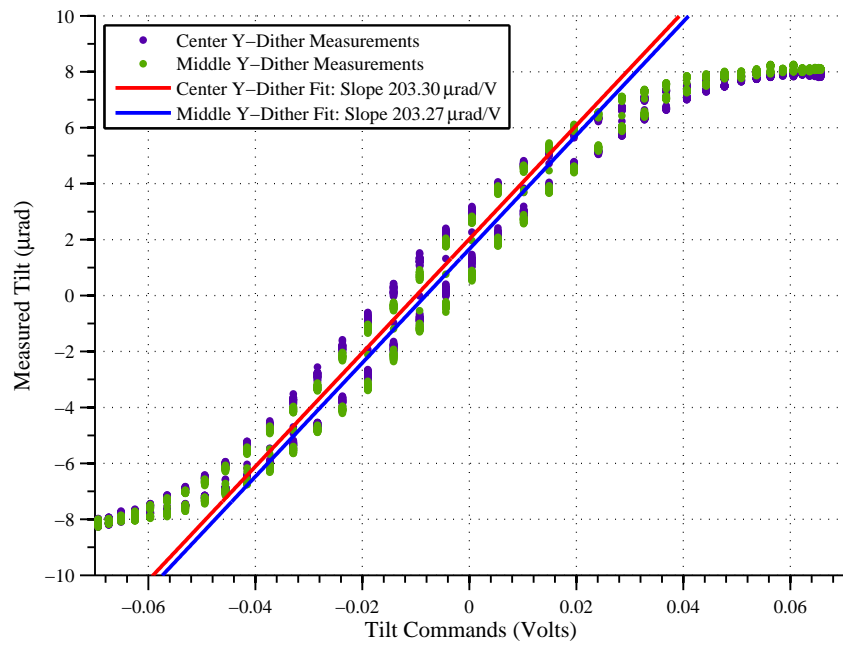


Figure 4.2: Center vs. middle  $y$ -gradient response.

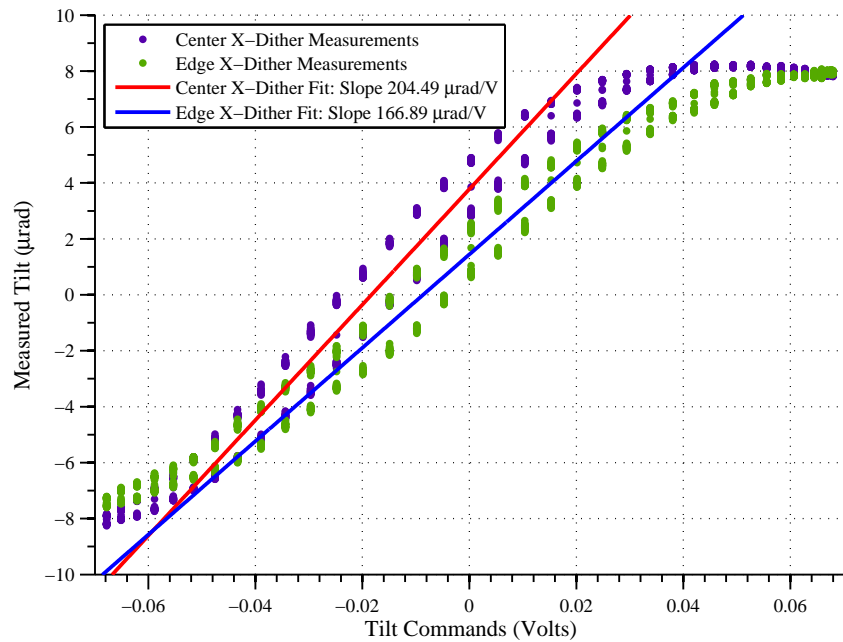


Figure 4.3: Center vs. edge  $x$ -gradient response.

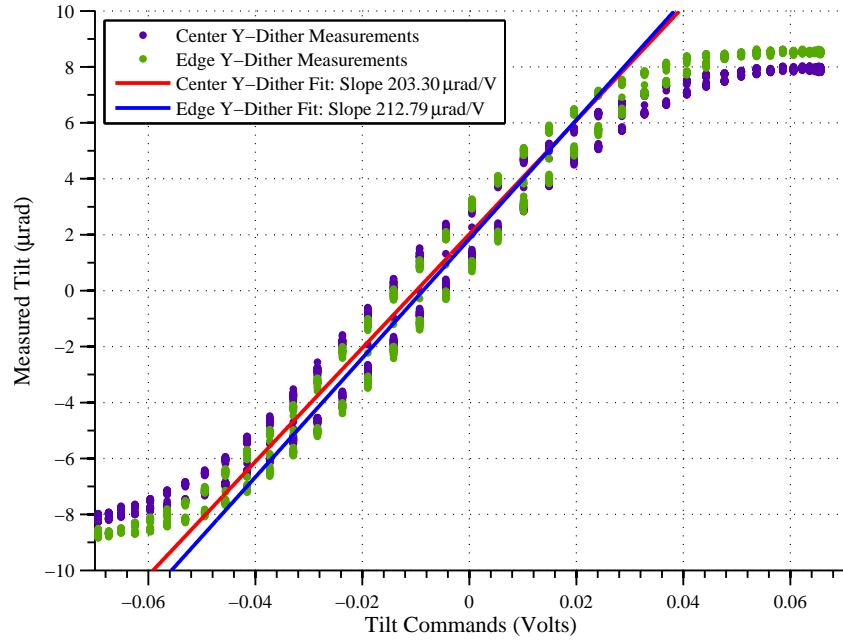


Figure 4.4: Center vs. edge  $y$ -gradient response.

Table 4.1: SH WFS slope measurement results.

Subaperture Location	Linear Region	
	$x$ -dither slope ( $\mu\text{rad}/\text{V}$ )	$y$ -dither slope ( $\mu\text{rad}/\text{V}$ )
Center	204.49	203.30
Middle	206.41	203.27
Edge	166.89	212.79

DM. This difference between edge partially illuminated subapertures and center fully illuminated subapertures indicates the need for spatially varying gain maps to provide different weighting to the residual phase measurements taken from the SH WFS. These residual phases are used for constructing the commands to the DM given in Eq. (2.29), therefore less confidence should be given to the measurements taken from the edge subapertures indicating a decrease over the filter gains  $b$  in these areas.

#### 4.2 Slaving vs Non-Slaving Results and Analysis

This experiment identified the performance difference of an AO system with and without slaving the actuators on the edge of the DM. As mentioned in Section 2.7.2, slaving is used to mitigate the ridging effect of the commanded and non-commanded actuators along the edges of the DM.

The data were collected using a moderate turbulence condition given in Table 3.4, and the AO system was tested using filter gain  $b$  fractions from 0.05 to 0.9 in

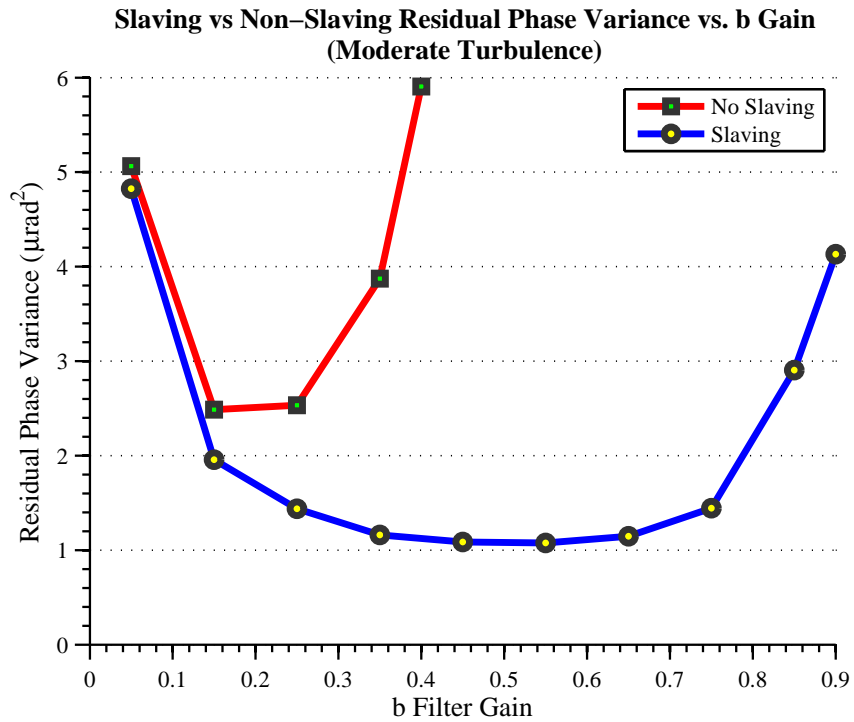


Figure 4.5: Slaving vs. non-slaving AO system performance comparison.

Table 4.2: Slaving vs. non-slaving filter gains with the least residual phase variance.

Batch	DM Filter		Residual Phase Variance ( $\mu\text{rad}^2$ )	Slaving
	$a$ gain	$b$ gain		
1	0.99	0.15	2.487	No
2	0.99	0.55	1.075	Yes

the servo-loop controller. These  $b$  gains are uniform over all actuators' servo-loops. The aperture-averaged residual phase variance was measured over the 500 frames of data with each  $b$  gain value. The residual phase variance is strongly correlated to the Strehl ratio of the AO system. The lower the residual phase variance, the higher the Strehl ratio of the system. Figure 4.5 directly shows the performance of slaving and not slaving the edge actuators. At low gain values of  $b = 0.05$ , the performance of each slaving/non-slaving scenario is relatively the same with approximately  $5 \mu\text{rad}^2$  of residual phase variance over the AO system. Though by increasing the filter gain  $b$  over each test, the slaved actuator AO system shows more dynamic range of performance. The non-slaved actuator AO system becomes unstable at a filter gain value of  $b = 0.4$  while the slaved actuator AO system only begins to lose performance at  $b = 0.85$ . The best overall performance of the AO system in terms of residual phase variance was found at a filter gain  $b = 0.55$  with a residual phase variance of  $1.075 \mu\text{rad}^2$ , given in Table 4.2. By slaving the actuators on the edges of the DM, the performance of the system in terms of residual phase variance was found to be smaller than not slaving the actuators under all  $b$  gain values. The slaved actuator AO system also has a wider range of stable  $b$  gain values in terms of minimal residual phase variance.

*4.2.1 Summary of the Slaving vs. Non-slaving experiment.* This experiment shows how significant the edge effects of the DM affect the overall AO system performance. Slaving is an important tool for smoothing out the ridging effects of controlled actuators to non-controlled actuators. As mentioned in Section 2.7.2, the slaving of actuators is not designed based on statistical characteristics of the turbulence and is prone to inducing its own instabilities into the system. Though this experiment

shows that the overall AO system's performance is improved significantly with slaving, a trade-off must be considered when taking into account that the slaving could induce an instability of its own.

### ***4.3 NUGE Results and Analysis***

Spatially varying gain maps given in Table 3.12 are used in a variety of experiments under various turbulent conditions and filter gains  $b$  given in Table 3.9 in order to mitigate for the edge effects that have been found to occur over the SH WFS and DM. Comparisons in the performance of the AO system using uniform and non-uniform gain maps were conducted. A baseline of uniform gains which provided the best overall Strehl ratio and least residual phase for each turbulence condition is used for the comparisons to the performance of using non-uniform gain maps. The AO system is then induced with instabilities that have been visually seen at the SOR's 3.5 meter telescope to explore the use of spatially varying gain to mitigate them.

The baseline of performance for the AO system is found by running the experiments given in Table 3.7 from Section 3.5.3. The results taken from those baseline experiments is shown in Figure 4.6, where the residual phase variance is plotted versus the uniform filter gains  $b$ . The low turbulence case 1 has the lowest overall residual phase variance because the turbulence is moving slowly and the AO system can better compensate for its variations. Subsequently, the moderate turbulence case 2 has slightly higher residual phase variance. The high level of turbulence case 3 has the fastest moving turbulence and smallest Fried parameter, and correspondingly has the largest residual phase variance over each filter gain  $b$  case.

Each plot in Figure 4.6 has a minimum residual phase variance given a particular filter gain  $b$  value, shown in Table 4.3. For each turbulence case, these filter gains  $b$  deliver the lowest residual phase variance indicating the best overall performance in the AO system and are used as the baseline performances utilizing uniform gain.

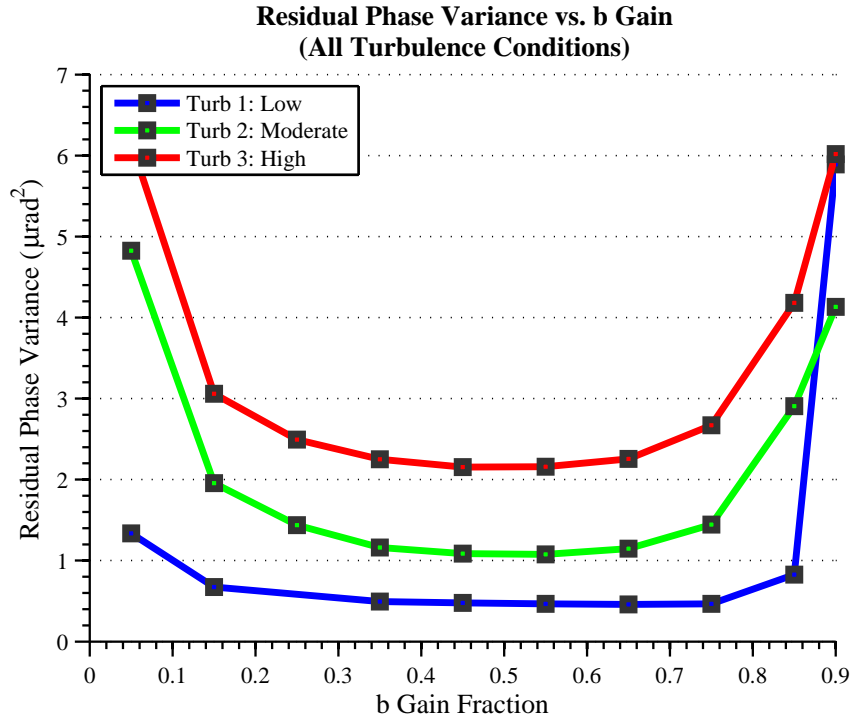


Figure 4.6: All turbulence conditions AO system performance comparison.

Table 4.3: Baseline uniform gain results.

Batch	Turbulence	DM Filter		Residual Phase Variance ( $\mu\text{rad}^2$ )
		$a$ gain	$b$ gain	
1	Low	0.99	0.65	0.460
2	Moderate	0.99	0.55	1.075
3	High	0.99	0.55	2.157



*4.3.1 Spatially Varying Gain Maps.* The NUGE experiments given in Table 3.9 examined three different gain maps each with three different turbulent conditions. The gain maps given in Figure 3.12 from Section 3.5.2 are used in these experiments to address the edge effects of the WFS and DM rather than the uniform gains.

The results of analyzing the data from all of the variations of gain maps and  $b$  gain edge fractions shows that gain map 1 provided increased performance in the AO system with respect to the baseline uniform gains in each resulting turbulence condition. Measuring the residual phase variances for each condition is used as an indicator of how the AO system is performing, but the Strehl ratio is the primary performance metric for determining how well the AO system is mitigating the turbulence.

Figure 4.7 is a plot of the temporally averaged Strehl ratio versus the  $b$  gain edge fraction for gain map 1 in the low turbulence condition. The Strehl ratio is shown to increase from 0.8728 using a uniform  $b$  gain to 0.8784 using gain map 1 with an edge fraction of 0.8. Figure 4.8 and Figure 4.9 are the subsequent plots of temporally averaged Strehl ratio versus the  $b$  gain edge fraction for gain map 1 in the moderate and high turbulence conditions, respectively. The resulting Strehl ratios and performance percentage increase over the uniform gains for each turbulence condition is given in Table 4.4.

Gain map 1 provided the largest improvement for the AO system in terms of the Strehl ratio compared to the other gain maps. As mentioned in Section 3.5.2, gain map 1 retains a uniform gain over the entire aperture except for the edge actuators. The SNR over the SH WFS array only has a significant decrease on the very edge actuators corresponding to gain map 1. Gain map 1 provides the largest increase in the performance of the AO system which can be correlated to its geometry and correspondence to the SNR distributed over the SH WFS array. The other gain maps use a graded  $b$  gain edge fraction from the edge to the center of the aperture. Deviations from the baseline  $b$  gains on actuator positions that are not on the edge of the aperture do not provide the greatest rejection of the turbulence. Therefore having

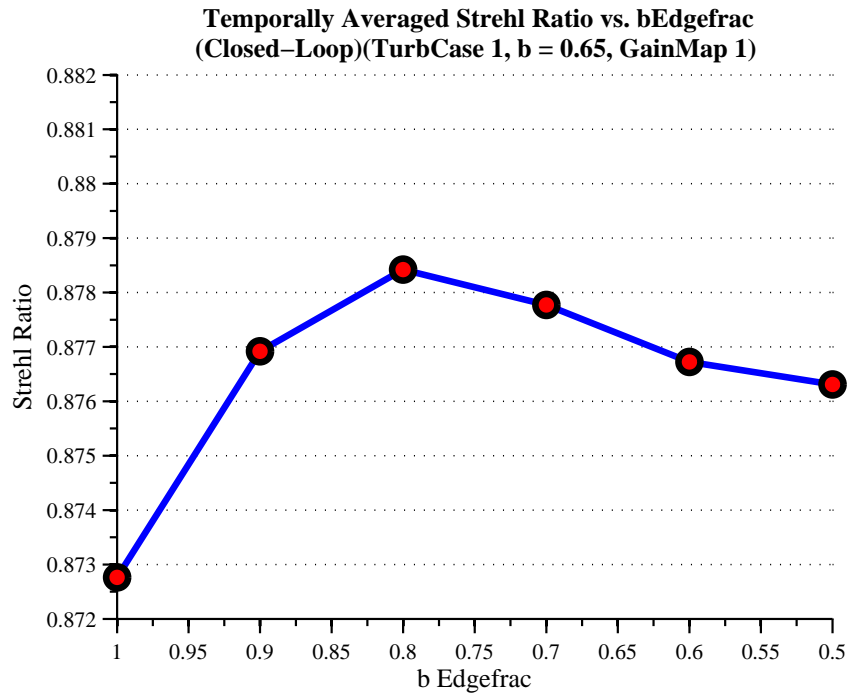


Figure 4.7: Gain Map 1 Strehl ratio improvement, Turb 1.

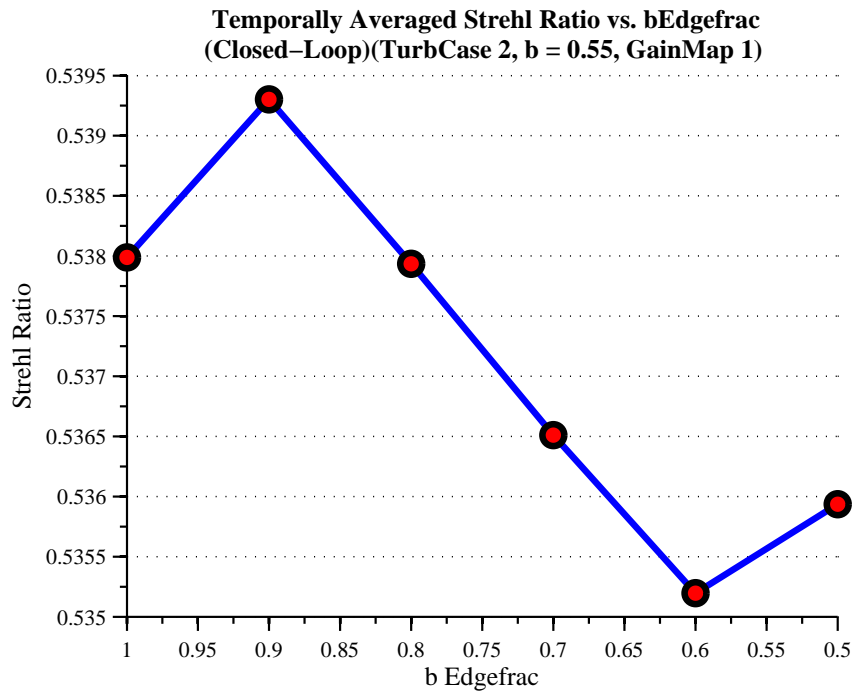


Figure 4.8: Gain Map 1 Strehl ratio improvement, Turb 2.

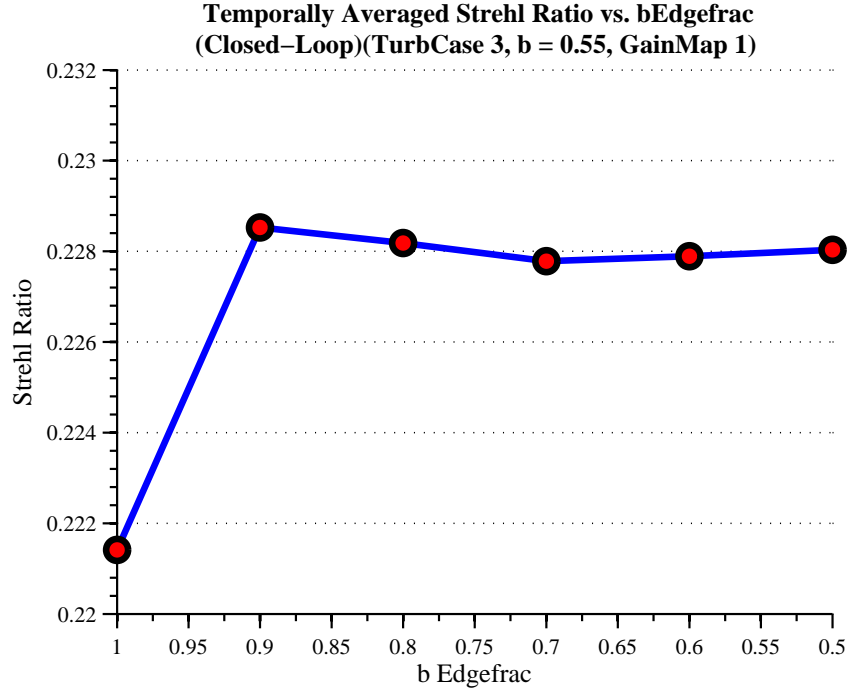


Figure 4.9: Gain Map 1 Strehl ratio improvement, Turb 3.

Table 4.4: Baseline uniform gain versus NUGE Strehl results.

Batch	Turbulence	NUGE DM Filter		Baseline Strehl	NUGE Strehl	Percent Increase (100%)
		$b$ gain	$b$ gain edge fraction			
1	Low	0.65	0.8	0.8728	0.8784	0.64
2	Moderate	0.55	0.9	0.5380	0.5393	0.24
3	High	0.55	0.9	0.2214	0.2285	3.20

lower  $b$  gains than the baseline values using gain maps 2 or 3 decreases the rejection of the turbulence because their geometries have decreased  $b$  gains on positions other than the areas that need to be compensated for such as the edges.

The largest percent increase in performance for the AO system using gain map 1 is under the high turbulence condition. The high turbulence condition produces the most residual phase variance over the edge subapertures, therefore increasing the importance of lowering the  $b$  gains over the edges in order to mitigate these high frequency noise and error components. The other turbulences in the low and moderate cases have a smaller residual phase variance over the edges. Thus decreasing the  $b$  gains on the edges provides less effect to the performance of the system because there

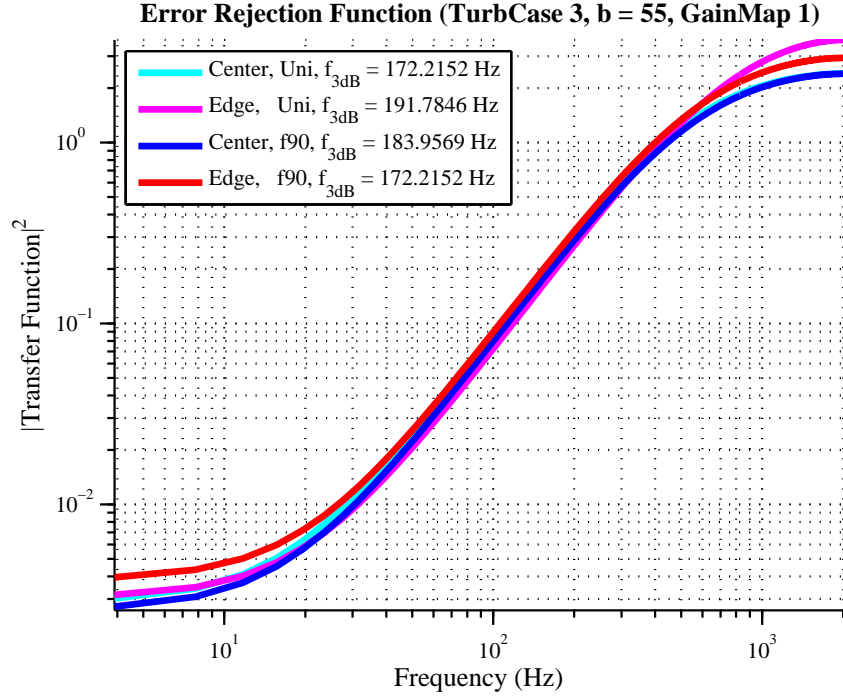


Figure 4.10: ERF comparison of uniform gain and gain map 1, Turb 3.

are less noise and error components to reject.

Decreasing the filter gain  $b$  over the edge actuators reduces the effective bandwidth of the system over those actuators. As mentioned in Section 3.1.4 the ASALT laboratory can be scaled with different system speeds. The ERF's in this experiment is scaled with a sampling frequency of 4000 Hz. Figure 4.10 is the ERF over center and edge actuators using the uniform gain  $b$  and the spatially varying gain map 1 with an edge fraction of 0.9 of the center gain  $b = 0.55$ . Using the baseline uniform gain of  $b = 0.55$  gives an ERF with a bandwidth over the center actuator positions of 172.21 Hz, while the edge bandwidth is 191.78 Hz. Therefore using the uniform gains, the edge actuator positions have larger bandwidths in the edge region which is counter productive because that is the region where there is the most noise and measurement errors. Using a center gain of  $b = 0.55$  with gain map 1 and a  $b$  gain edge fraction of 0.9 decreases the gain over the edge actuators to  $b = 0.495$  which reduces the effective bandwidth over this region to 172.21 Hz. Now the center gain has a bandwidth of 183.96 Hz using the gain map 1, but in this region there is less

noise to compensate for, so it is allowable to have a larger bandwidth. Thus using gain map 1 decreases the bandwidth on the edge actuators which are more susceptible to noise while increasing the bandwidth over the region with less measurement errors, effectively increasing the performance of the AO system representable by the increase in Strehl ratio.

*4.3.2 Low SNR.* The AO system is tested under a low SNR regime with the parameters in Table 3.10 from Section 3.5.4 in order to compare performances with the high SNR regime used in the other experiments. A baseline of performance is found using uniform gains over the moderate turbulence in the low SNR regime for comparisons to the spatially varying gain maps. Figure 4.11 is a plot of residual phase variance versus different filter gains  $b$  for the low SNR condition and high SNR condition. Figure 4.12(a) is the SNR over the subapertures in the high SNR regime, while Figure 4.12(b) is in the low SNR regime. The SNR averaged over the entire aperture in the low SNR regime is 19.99 while the high SNR is 52.04, both calculated

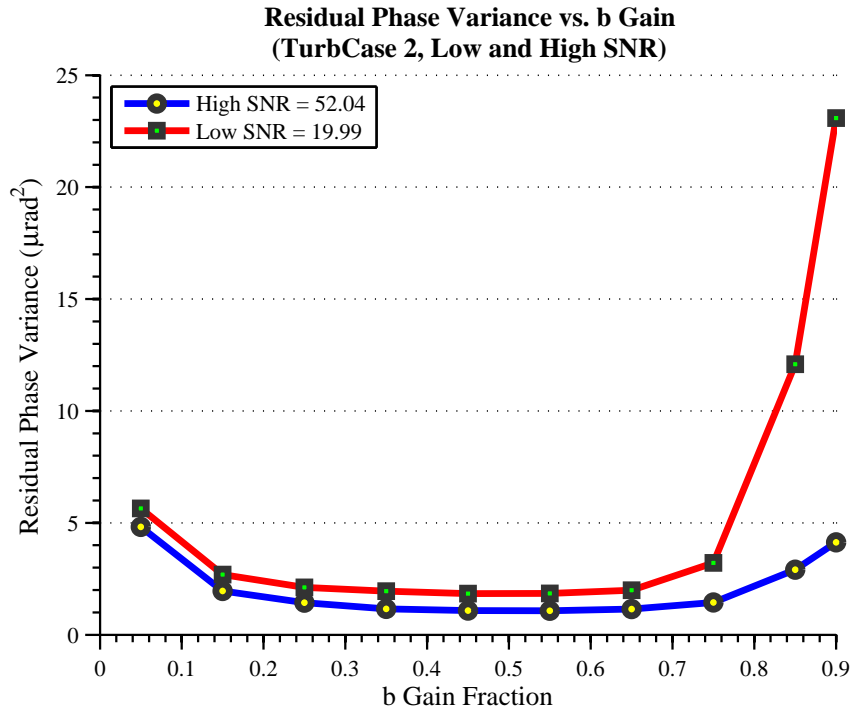


Figure 4.11: Low SNR and high SNR AO performance comparison, Turb 2.

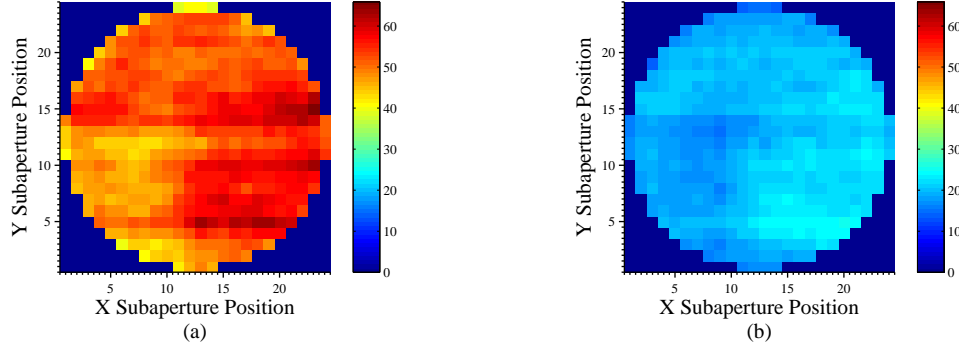


Figure 4.12: Low SNR and high SNR plot over subapertures. (a) The SNR over each subaperture in the high SNR regime. The aperture averaged SNR is 52.04. (b) The SNR over each subaperture in the low SNR regime. The aperture averaged SNR is 19.99.

from Eq. (2.17). Noise contributes a larger factor in the low SNR regime with an AO system and causes more errors in the measurements from the SH WFS. The residual phase variance over the entire spectrum of filter gains  $b$  is of higher magnitude in the low SNR regime than the high SNR regime, which indicates more measurement error in the low SNR case. The system operates with the lowest residual phase variance using a uniform filter gain  $b = 0.55$ . The Strehl ratio of the low SNR regime at this baseline uniform gain value  $b = 0.55$  with these parameters is 0.3778. Just as in the high SNR case, the greatest magnitude of residual phase variance is located on the edge actuators.

The AO system under the low SNR regime were tested using spatially varying gain maps from Table 3.11. The analysis of the results show that using the baseline filter gain  $b = 0.55$  with gain map 1 and an  $b$  edge fraction of 0.9 gives a larger Strehl ratio than using the standard uniform gain, shown in Figure 4.13. The Strehl ratio using the spatially varying gain map 1 is 0.3908 which is a 3.42% increase in Strehl ratio over the baseline uniform gain for the AO system. The AO system in low SNR regimes has greater residual phase variance along the edges of the aperture because they have lower SNR and are more sensitive to noise. Therefore decreasing the filter gains  $b$  over this region with gain map 1 reduces the bandwidth on the edges so more of the noise is rejected.

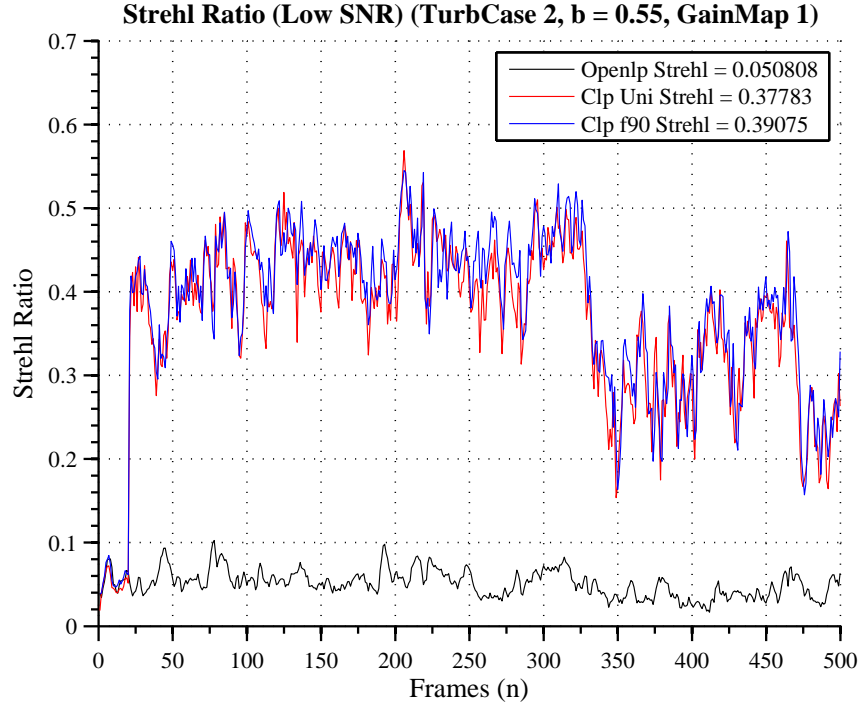


Figure 4.13: Low SNR Strehl ratio, Turb 1.

4.3.3 *Mitigation of Instabilities.* The NUGE experiments from Table 3.9 in Section 3.5.3 explored regimes where instabilities along the edges of the DM begin to form in order to find techniques to mitigate them. Research at the SOR found that the first instability that forms over the DM is the waffle mode mentioned in Section 2.7.3. In order to induce the instabilities into the AO system in the ASALT lab the filter gains  $b$  were experimented in regimes where  $b > 0.55$ .

Figure 4.14 is the averaged residual phase variance of turbulence condition 3 over 500 frames measured from the SH WFS. Visually the edges of the aperture show larger magnitudes of residual phase variance which indicate that the edge effects are decreasing the effectiveness of the measurements. Figure 4.15 is the same plot with the AO loop closed using a filter gain  $b = 0.85$ . In the filter gain regime  $b = 0.85$  the waffle mode begins to appear along the edges of the interferogram over the DM. Though closing the AO loop mitigates a large portion of the residual phase variance due to the turbulence, the edges still show effects which are indicators of beginning

instabilities over the DM.

All of the gain maps with different  $b$  gain edge fractions are tested in this regime in order to find a gain map that mitigates the instabilities. The results showed that the Gaussian gain map 3 mitigated for the instabilities and visually decreased the amount of waffling occurring over the interferogram of the DM. Figure 4.16 is the averaged residual phase variance of turbulence condition 3 with  $b = 0.85$  and gain map 3 using a  $b$  edge fraction of 0.5. The magnitude of the residual phase variance over the edges of the DM were decreased from using gain map 3 because the gain over the region of instability along the edges was decreased while still maintaining the  $b$  gain over the center of the DM.

Figure 4.17 shows the interferograms of the DM with and without the Gaussian gain map 3 applied to the servo-controller. Because the ATS can be used to repeat the same turbulence conditions, a direct comparison shows that the waffle mode in Figure 4.17(a) is mitigated by applying Gaussian gain map 3 as shown in

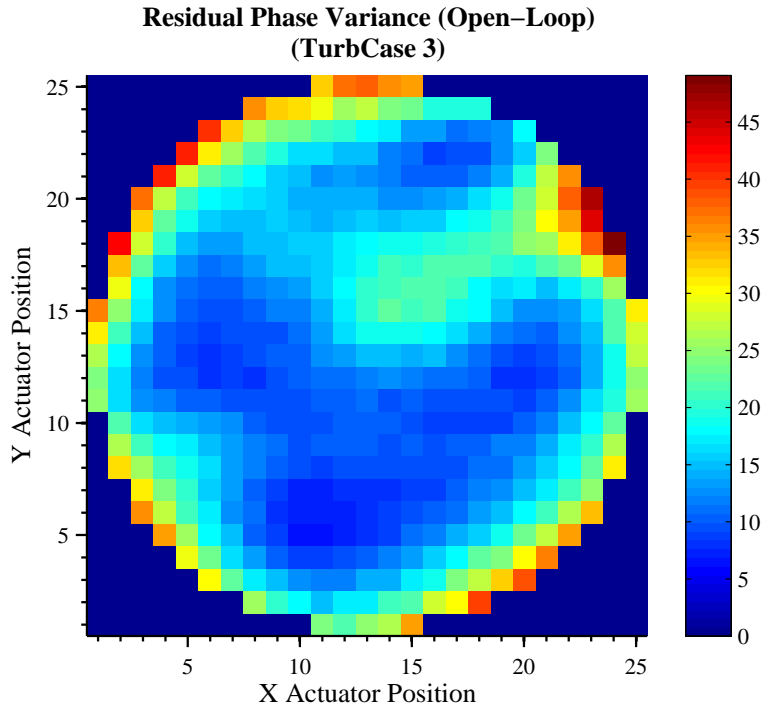


Figure 4.14: Residual phase variance taken in open loop, Turb 3.



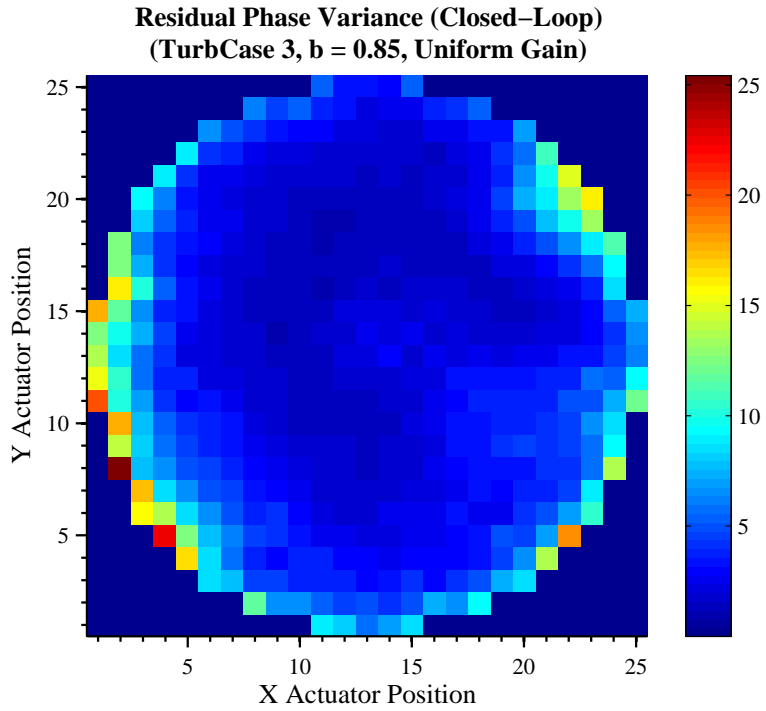


Figure 4.15: Residual phase variance taken in closed loop with uniform gain, Turb 3.

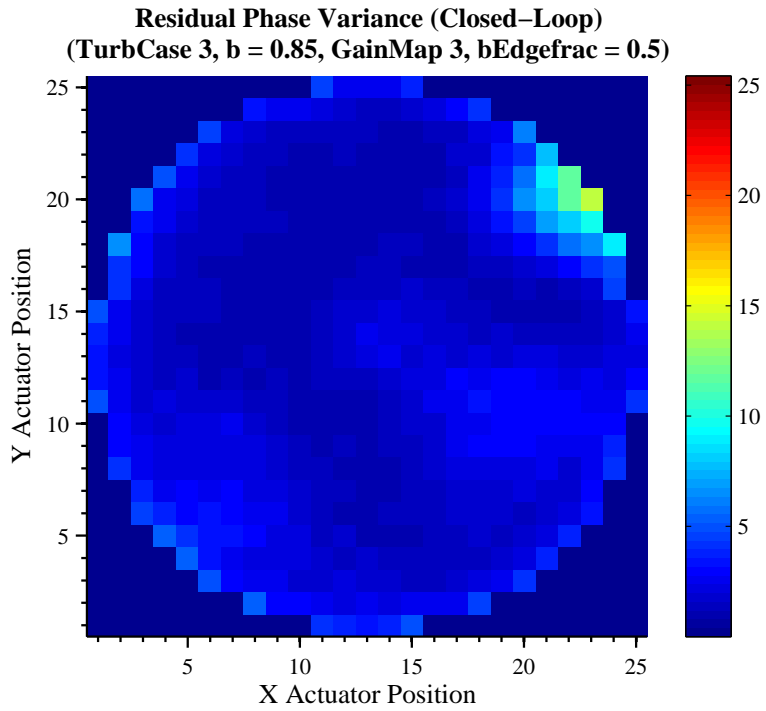


Figure 4.16: Residual phase variance taken in closed loop with gain map 1, Turb 3.

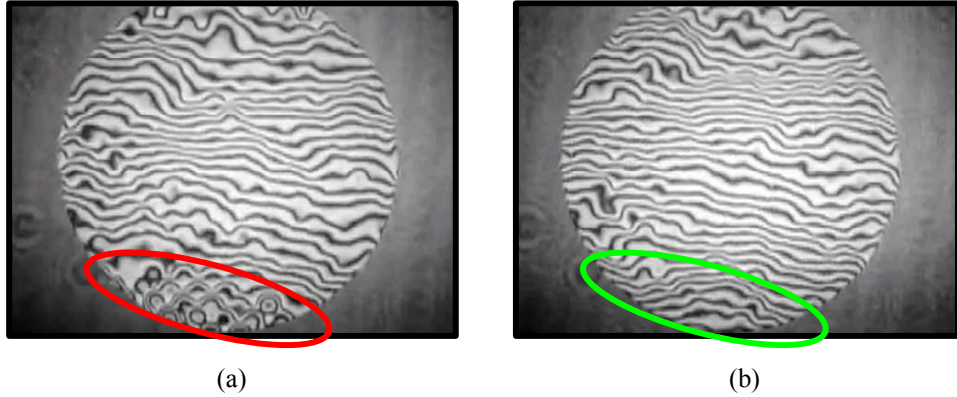


Figure 4.17: Interferograms of DM waffle mode mitigation. (a) Interferogram with the waffle mode instability beginning to form on the edge actuator region. (b) Interferogram of the DM for the same turbulence and frame except with the Gaussian gain map applied to mitigate for the waffle mode.

Figure 4.17(b). The waffle mode is identified visually over the interferogram and is shown to be reduced over the same turbulence conditions and repeated frame.

Figure 4.18 shows the aperture averaged residual phase variance versus the  $b$  gain edge fractions used with Gaussian gain map 3. The residual phase variance is

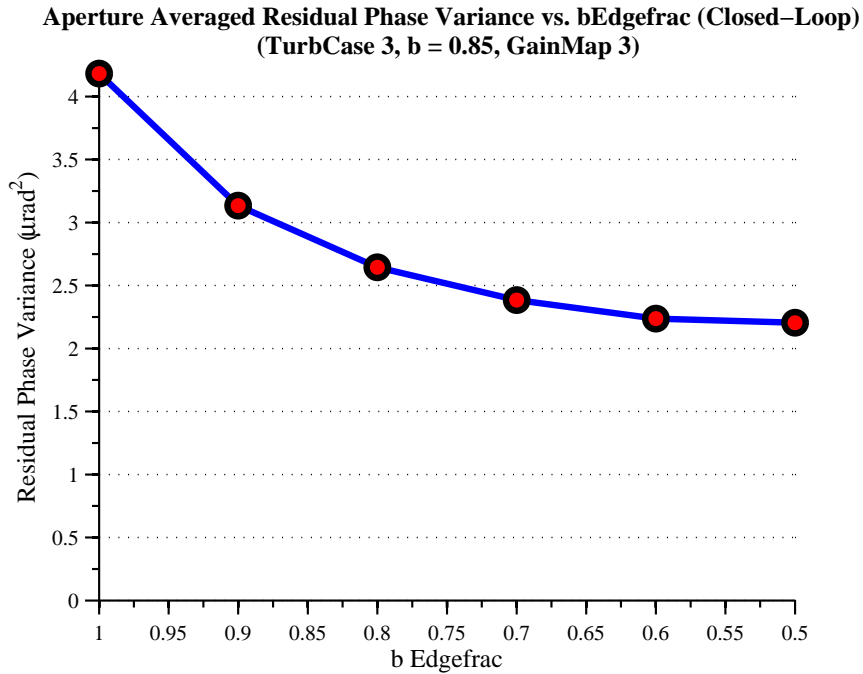


Figure 4.18: Aperture averaged residual phase variance taken in closed loop, Turb 3

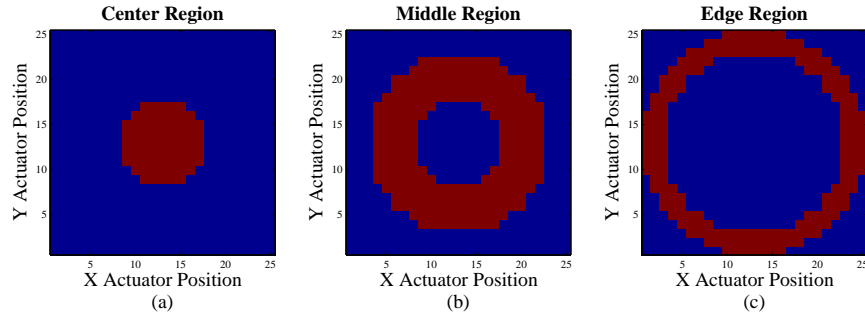


Figure 4.19: Spatial regions. These three regions are where the residual phase is averaged over to compare the compensation of the turbulence by the AO system spatially.

decreased as the  $b$  gain edge fraction is lowered along the edges of the gain map. A decrease in the waffle mode instability is correlated to a decrease in the residual phase variance.

In order to show the spatial influence of the gain maps over the response of the DM, the residual phase variance is averaged over three regions, shown in Figure 4.19.

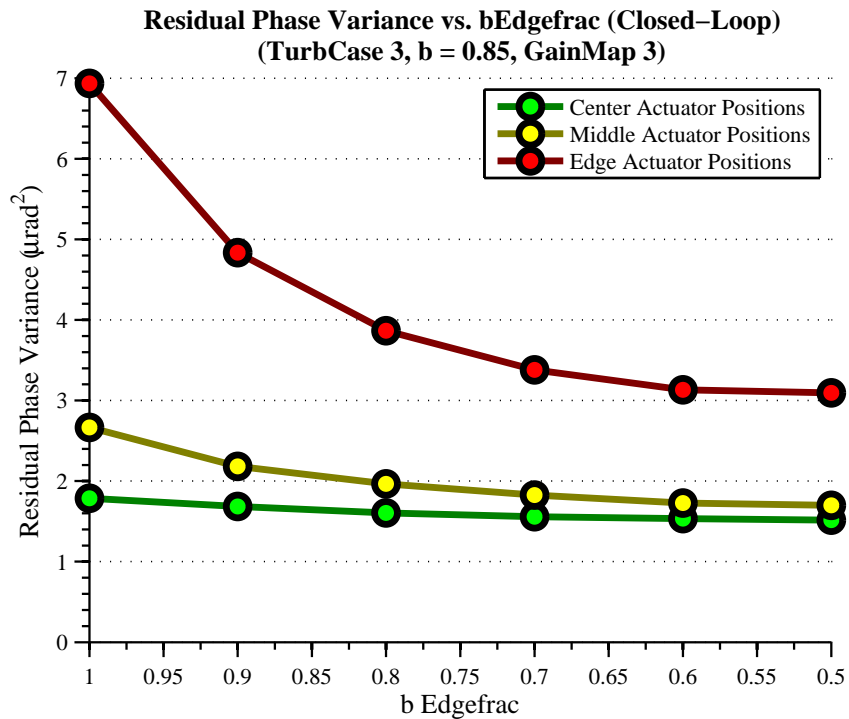


Figure 4.20: Spatial regions AO system performance comparison, Turb 3.

Rather than effectively lowering the entire response of the DM using a uniform gain  $b$  over the servo-loop, a spatially varying gain can concentrate on mitigating over the specific regions that correspond to the gain map used. Figure 4.20 is a plot of the three spatial regions' residual phase variances versus the  $b$  gain edge fraction used with gain map 3 in the high turbulence condition. As the Gaussian gain map 3's edge fraction is lowered, the edge region's residual phase variance is decreased by a larger magnitude than the center and middle regions. Therefore showing the concentration in the spatial region's response corresponding to the geometry of the spatial gain map.

*4.3.4 Summary of Spatial Varying Gain Maps.* The experiments show the performance of an AO system using spatially varying gain maps can outperform the baseline uniform gains with respect to Strehl ratio in all three turbulence conditions. In the low SNR regimes, an AO system is susceptible to more noise effects subsequently increasing the residual phase variance. The spatially varying gain maps were found to be the most beneficial in low SNR and high turbulence regimes because that is when there is the most noise and measurement error effects over the edge region of the SH WFS and DM. Therefore decreasing the bandwidth over the edge using spatially varying gain can mitigate some of these effects which can improve the AO system's performance. The experiments also show that a Gaussian gain map can be used to reduce the beginning of instabilities in regimes where the system is going unstable and the waffle mode begins to appear along the edges of the DM.

## V. Conclusions

This chapter presents a summary of the research and key results from Chapter IV. Recommendations of further work that were beyond the scope of this research are also discussed.

### 5.1 Summary

The objective of this research was to develop and experimentally verify the use of spatially varying gain maps on the servo-loop controller for improvements in the performance of an AO system and the mitigation of instabilities that can occur over the edge actuators of a DM. The SH WFS gradient measurement capability was experimentally investigated by applying a commanded tilt with the SM and measuring the resultant sensor measurements. The edge subapertures were shown to have lower SNR and non-uniformly shaped focal spots which contributed to noisy gradient measurements and differences between the measured  $x$  and  $y$  gradients, respectively. The DM was then tested with and without slaving the outer edge actuators. Slaving was found to stabilize the system and provide a larger dynamic range of operation with respect to the filter gains  $b$ . Therefore, slaving was shown to be an important tool for better performance of the AO system, yet it also must be considered as a contributor to some instabilities that are inherently related to slaving, mentioned in Section 2.7.2. The analysis of the experiments conducted over the SH WFS and DM provided insight into the importance that the edge effects have on the system. The non-uniform gain maps were then developed to compensate for edge effects by having lower filter gains  $b$  designated for the edge subapertures. This lowered the bandwidth over the edge actuators which are the most susceptible to the edge effects. Gain map 1 had a ring of lower  $b$  gains over the outer actuators, and was experimentally shown to increase the overall Strehl ratio of the AO system in all of the tested turbulence conditions. Specifically, the non-uniform gain maps provide the largest increase of Strehl ratio over the AO system in low SNR and high turbulent scenarios. Experiments were also conducted in regimes where instabilities formed over the edge actuators of the DM.

Gaussian gain map 3 was shown to significantly reduce the overall residual phase variance over the edge actuators thereby reducing the formation of the instabilities.

This thesis directly supports NGAS's study of spatially varying gain, showing that as a proof-of-concept, non-uniform dynamic control of the DM can provide performance and stability improvements to an AO system. Applications such as the Air Force's Airborne Laser system that uses adaptive optics in low SNR regimes under highly turbulent conditions can benefit the most from spatially varying gain because that is when the edge effects have more of an influence over the performance of the system. Also, Gaussian gain maps have been shown through this research, to have the capability of reducing instabilities that are formed over the edge actuators of a DM. During live testing, an AO operator at the SOR has the option of adjusting the uniform filter gain  $b$  over the system in real-time. This research suggests that the operator could utilize a Gaussian gain map over on the AO system to mitigate instabilities when they begin to form over the DM.

## 5.2 *Key Results*

This section includes the significant conclusions taken from the experiments and results from Chapter IV.

- The edge subapertures of the SH WFS were verified to measure  $x$  and  $y$  gradients differently due to non-uniformly shaped focal spots and having lower SNR. The center subapertures were verified to measure gradients linearly over a range of  $\pm 4\mu\text{rad}$  of tilt.
- Slaving the actuators increased the operational range of usable filter gains  $b$  and reduced the residual phase variance over all cases. In contrast, closing the AO loop without slaving increases the residual phase variance of the edge actuators and decreases the operational range of usable filter gains  $b$ .
- Non-uniform gain maps were developed that address the edge effects of the WFS and DM. Experimentally, they were shown to have the capability of influencing

the bandwidth of the actuators in specific spatial regions governed by the design of the gain map.

- Using non-uniform gain map 1 was shown to outperform standard uniform gain with respect to increases in the Strehl ratio of the AO system under all three tested turbulence conditions. Spatially varying gain maps provide the largest increase in Strehl ratio for low SNR and high turbulence cases.
- Instabilities that occur along the edge actuators of a DM were reduced through the use of Gaussian gain maps. These gain maps locally reduced the edge region's residual phase variance while maintaining the same central filter gain in the center region of the DM.
- This research verified, as a proof of concept, that spatially varying gain can be used to enhance the performance of an AO system and be used for mitigation of instabilities, warranting more research in this area.

### 5.3 Recommendations

This section provides recommendations for future work related to this research.

*Continuation of Spatially Varying Gain Maps.* More test cases and gain map geometries could be tested to enhance the robustness of how and when gain maps could be used for the system. A controller using fuzzy control logic could be designed with a look-up table of optimum filter gains  $b$  given a particular SNR and residual phase variance.

*Minimum Variance Controller based on Spatial Regions.* Standard minimum variance controllers are designed to minimize the aperture averaged residual mean square phase. Yet this research shows that the residual phase variance between center and edge regions of the aperture are starkly different. Therefore a controller can be designed to minimize the residual mean square phase over particular regions of the aperture in order to take into account the spatial differences of phase measurements

over the aperture.

*Statistical Characterization and Identification of the Waffle Mode Instability.*

The waffle mode instability was shown to be one of the first instabilities seen over the DM in high residual phase variance cases. The SH WFS cannot measure this instability, but it can be statistically characterized from the DM commands. Characterizing when the waffle mode occurs would allow for better identification of the instability so that it can be locally mitigated using spatially varying gain. Therefore rather than reducing the overall performance of the system by generally lowering the gain over a broader region, the instability could be specifically targeted and mitigated.



## Appendix A. Matlab Code

The following code are some of the more unique scripts developed for the analysis of this thesis.

### A.1 Hdf5 reader code

Listing A.1: Hdf5 Data Extraction code.

```
% *****...

% This code converts hdf5 data taken from the ASALT lab and ...
%   converts it to
%   .mat files
%
5 % Saves variables to mat files for particular investigations.
%   .mat file sections
%   Error Rejection Functions
%   ol and cl phase, b gain, a gain, gain map, edge_frac
%   Residual Phase Variance
10 %   cl phase, b gain, a gain, gain map, edge_frac
%   Signal-to-Noise Ratio
%   camera counts, dark counts, b gain, a gain, gain map, ...
%   edge_frac
%   Correlation to Waffle Mode
%   dm cmds, b gain, a gain, gain map, edge_frac
15 % Strehl Ratio
%   PSF camera counts, open loop camera counts, camera counts, b ...
%   gain,
%   a gain, gain map, edge_frac
%   ATS
%   ro, fG, rytov
20 %
% Author: Kevin Vitayaudom
% Date: 1/4/2008
% *****...

25 close all
clear all
clc;

load ActMask.mat
30
% Declare files to investigate
Turb = '2';
Gmap = '1';
b = '90';
35 drive = 'F';

% path where data is located
```

```

filepath_test = [drive,':\NUGE Thesis\07 - NUGE\data\2007-12-21\...
    New Data for Turbulence 2\T2\g1'];

40 % set the filepath where the data is kept
filepath_ref = [drive,':\NUGE Thesis\07 - NUGE\data\2007-12-21\New...
    Data for Turbulence 2'];

% filename designators
Edgefrac = ['Uni','f90','f80','f70','f60','f50'];
45 Date = '2007-12-17';
DateOp = '2007-12-17';
Time = ['1501','1507','1503','1625','1650','1731'];

% savename designators
50 DataERF = 'ERF';
DataPhV = 'PhV';
DataSNR = 'SNR';
DataWaf = 'Waf';
DataStl = 'Stl';
55 DataATS = 'ATS';

% savenames
SaveERF = ['T',Turb,'g',Gmap,DataERF,'b',b,'_20071218'];
filepath_sav_ERF = [drive,':\NUGE Thesis\07 - NUGE\current ...
    mscripts at SOR\Data Analysis\Data matfiles\NonUniform Gain\NEW...
    Data\',SaveERF];
60 SavePhV = ['T',Turb,'g',Gmap,DataPhV,'b',b,'_20071218'];
filepath_sav_PhV = [drive,':\NUGE Thesis\07 - NUGE\current ...
    mscripts at SOR\Data Analysis\Data matfiles\NonUniform Gain\NEW...
    Data\',SavePhV];
SaveSNR = ['T',Turb,'g',Gmap,DataSNR,'b',b,'_20071218'];
filepath_sav_SNR = [drive,':\NUGE Thesis\07 - NUGE\current ...
    mscripts at SOR\Data Analysis\Data matfiles\NonUniform Gain\NEW...
    Data\',SaveSNR];
SaveWaf = ['T',Turb,'g',Gmap,DataWaf,'b',b,'_20071218'];
65 filepath_sav_Waf = [drive,':\NUGE Thesis\07 - NUGE\current ...
    mscripts at SOR\Data Analysis\Data matfiles\NonUniform Gain\NEW...
    Data\',SaveWaf];
SaveStl = ['T',Turb,'g',Gmap,DataStl,'b',b,'_20071218'];
filepath_sav_Stl = [drive,':\NUGE Thesis\07 - NUGE\current ...
    mscripts at SOR\Data Analysis\Data matfiles\NonUniform Gain\NEW...
    Data\',SaveStl];
SaveATS = ['T',Turb,'g',Gmap,DataATS,'b',b,'_20071218'];
filepath_sav_ATS = [drive,':\NUGE Thesis\07 - NUGE\current ...
    mscripts at SOR\Data Analysis\Data matfiles\NonUniform Gain\NEW...
    Data\',SaveATS];

70 % hdf5 selection
file_hdf5_1 = ['\T',Turb,'b',b,'__',Edgefrac(1,:),'_',DateOp,'_',...
    Time(1,:),'.hd5'];
file_hdf5_2 = ['\T',Turb,'b',b,'g',Gmap,Edgefrac(2,:),'_',Date,'_'...
    ,Time(2,:),'.hd5'];

```

```

file_hdf5_3 = ['\T',Turb,'b',b,'g',Gmap,Edgefrac(3,:), '_ ',Date,'_'...
,Time(3,:), '.hd5'];
75 file_hdf5_4 = ['\T',Turb,'b',b,'g',Gmap,Edgefrac(4,:), '_ ',Date,'_'...
,Time(4,:), '.hd5'];
file_hdf5_5 = ['\T',Turb,'b',b,'g',Gmap,Edgefrac(5,:), '_ ',Date,'_'...
,Time(5,:), '.hd5'];
file_hdf5_6 = ['\T',Turb,'b',b,'g',Gmap,Edgefrac(6,:), '_ ',Date,'_'...
,Time(6,:), '.hd5'];
file_hdf5_7 = ['\T',Turb,'_open_lp_2007-12-17_1728.hd5'];

80 file_hdf5 = [file_hdf5_1;file_hdf5_2;file_hdf5_3;file_hdf5_4;...
file_hdf5_5;file_hdf5_6;file_hdf5_7];

% declare dummy variables for memory
HRT_resPhase_all = zeros(25,25,500,7);
SC_cameraCount_all = zeros(128,128,500,7);
85 HRT24_all = zeros(24,24,500,7);
DM_cmds_all = zeros(25,25,500,7);
bGain_all = zeros(1,7);
aGain_all = zeros(1,7);
bGain_edgefrac_all = zeros(1,7);
90 phase_mean_all = zeros(25,25,7);
phase_var_all = zeros(25,25,7);
phase_std_all = zeros(25,25,7);

% strehl Info
95 scoringHD5string = 'Frame Sources/Sensor Camera FS (001:0BCA)/...
Video Frame/Data';
scoringHD5stringCC = 'Frame Sources/Sensor Camera FS (012:0BCA)/...
Video Frame/Data';

% set the path for how the HD5 data was stored
DateStamp = '2007-12-22';
100 darks = double(hdf5read([filepath_ref, '\Darks_' DateStamp '_0136....
hd5'], [scoringHD5string]));
darksCC = double(hdf5read([filepath_ref, '\Darks_' DateStamp '...
_0136.hd5'], [scoringHD5stringCC]));

frames = 500; % number of frames calculated
Darks24 = zeros(24,24,500);
105

% extracts quadcell data
for nd = 1:frames;

Md = zeros(4,4);
110 Md(2:3,2:3) = 1;
Md = repmat(Md,[24,24]);
D = Md.*darksCC(:, :, nd);
D = D(any(Md,1),:);
D = D(:,any(Md,2)); % now a 48 x 48
115

Ld = zeros(24,48);

```

```

        for md = 1:24
            cold = 2*md;
120         rowd = md;
            Ld(rowd,cold-1) = 1;
            Ld(rowd,cold) = 1;
        end
        Rd = Ld';
125
        D = (Ld * D * Rd) / 4; % now averaging over 2 x 2 over...
            each subaperture

        Darks24(:, :, nd) = D;
    end
130
    PSFRef = double(hdf5read([filepath_ref, '\PSF_Ref_' DateStamp '...
        _0132.hdf5'], [scoringHD5string]));

    avgDark = mean( darks , 3 ); % calculates the average frame of ...
        background darks
    clear darks; % clear the variable to save memory
135 clear darksCC;

    avgPSF = mean( PSFRef , 3 ) - avgDark; %Calculates the average psf...
        minus the background darks (the denominator of the Strehl)
    clear PSFRef; % clear the variable to save memory

140 ol = double(hdf5read([filepath_test,file_hdf5_7], [...
        scoringHD5string])); % Extract your data

    % waffle mode tester
    % temporal correlation
    wafProc = zeros(1,500);
145 for zdx = 1:2:500
        wafProc(zdx) = 32767;
        wafProc(zdx+1) = -32767;
    end

150 % spatial correlation
    Waffle25 = zeros(25);
    % create waffle pattern
    for kdx = 1:25
        for jdx = 1:25
155         flag = rem((kdx + jdx),2);
            if flag == 1
                Waffle25(kdx,jdx) = -32767;
            else
                Waffle25(kdx,jdx) = 32767;
160         end
        end
    end
    end
    Waffle25 = Waffle25.*HRT_Msk25act_inr;

```

```

165 % extract data from hdf5 files
    for idx = 1:7

        % Reading data from HRT
        SC_cameraCount = double(hdf5read([filepath_test, file_hdf5(idx...
            ,:)],...
170         '/Frame Sources/Sensor Camera FS (001:0BCA)/Video Frame/...
            Data'));

        HRT_resPhase = double(hdf5read([filepath_test, file_hdf5(idx...
            ,:)],...
            '/Processing Nodes/Hartmann RTR (012:2717)/Phase/Data'));
        HRT_resPhase = HRT_resPhase(:,:(1:500))*(2*pi)/4096;
175     HRT_resPhase_all(:,:(1:500),idx) = HRT_resPhase;
        phase_mean_all(:,:(1:500),idx) = mean(HRT_resPhase,3);
        phase_var_all(:,:(1:500),idx) = var(HRT_resPhase,0,3);
        phase_std_all(:,:(1:500),idx) = std(HRT_resPhase,0,3);
        clear HRT_resPhase;

180     HRT_cameraCount = double(hdf5read([filepath_test, file_hdf5(...
        idx,:)],...
            '/Frame Sources/Sensor Camera FS (012:0BCA)/Video Frame/...
            Data'));

        HRT24 = zeros(24,24,frames);
185     for n = 1:frames;

            M = zeros(4,4);
            M(2:3,2:3) = 1;
            M = repmat(M,[24,24]);
190         H = M.*HRT_cameraCount(:,:(1:500),n);
            H = H(any(M,1),:);
            H = H(:,any(M,2)); % now a 48 x 48

            L = zeros(24,48);
195         for m = 1:24
            col = 2*m;
            row = m;
            L(row,col-1) = 1;
200         L(row,col) = 1;
            end
            R = L';

            H = (L * H * R) / 4; % now averaging over 2 x 2 over ...
                each subaperture
205         HRT24(:,:(1:500),n) = H;
        end

        clear HRT_cameraCount

```

```

210 DM_NUGE_cmds = double(hdf5read([filepath_test, file_hdf5(idx...
    ,:)],...
    '/Processing Nodes/DM Filter NUGE new (012:2771)/dm_cmd/...
    Data')));

DM_NUGE_aGain = double(hdf5read([filepath_test, file_hdf5(idx...
    ,:)],...
215 '/Processing Nodes/DM Filter NUGE new (012:2771)/...
    ConfigItems/aGain/Data')));

DM_NUGE_bGain = double(hdf5read([filepath_test, file_hdf5(idx...
    ,:)],...
    '/Processing Nodes/DM Filter NUGE new (012:2771)/...
    ConfigItems/bGain/Data')));

220 DM_NUGE_bGain_edgefrac = double(hdf5read([filepath_test, ...
    file_hdf5(idx,:)],...
    '/Processing Nodes/DM Filter NUGE new (012:2771)/...
    ConfigItems/bGain_edgefrac/Data')));

ATS_r0 = double(hdf5read([filepath_test, file_hdf5(idx,:)],...
    '/Processing Nodes/ATS Estimator (003:2744)/r0/Data')));
225

ATS_fG = double(hdf5read([filepath_test, file_hdf5(idx,:)],...
    '/Processing Nodes/ATS Estimator (003:2744)/fG/Data')));

ATS_rytov = double(hdf5read([filepath_test, file_hdf5(idx,:)...
    ],...
230 '/Processing Nodes/ATS Estimator (003:2744)/Rytov/Data')));

SC_cameraCount_all(:, :, :, idx) = SC_cameraCount(:, :, (1:500));
HRT24_all(:, :, :, idx) = HRT24(:, :, (1:500));
DM_cmds_all(:, :, :, idx) = DM_NUGE_cmds(:, :, (1:500));
235

aGain_all(:, idx) = DM_NUGE_aGain;
bGain_edgefrac_all(:, idx) = DM_NUGE_bGain_edgefrac;
bGain_all(:, idx) = DM_NUGE_bGain;

240 % clear for memory
clear DM_NUGE_aGain DM_NUGE_bGain DM_NUGE_bGain_edgefrac
clear DM_NUGE_cmds SC_cameraCount

end
245 % conversion from SOR data
% r0(cm) = r0_DM(mm)*(size of tele)*100/(act spacing * # of ...
    act across
% DM)

250 ATS_r0_all = ATS_r0(100)*(1e-3)*1.5*100/((7.7e-3)*25);
ATS_fG_all = ATS_fG(100); % fG/fs
ATS_Rytov_all = ATS_rytov(100);

```

```

% save data
save(filepath_sav_ERF, 'aGain_all','bGain_all','bGain_edgefrac_all...
',...
255 'HRT_resPhase_all')
save(filepath_sav_PhV, 'aGain_all','bGain_all','bGain_edgefrac_all...
',...
'phase_mean_all','phase_var_all','phase_std_all')
save(filepath_sav_SNR, 'aGain_all','bGain_all','bGain_edgefrac_all...
',...
'HRT24_all','Darks24')
260 save(filepath_sav_Waf, 'aGain_all','bGain_all','bGain_edgefrac_all...
',...
'DM_cmds_all','wafProc','Waffle25')
save(filepath_sav_Stl, 'aGain_all','bGain_all','bGain_edgefrac_all...
',...
'avgDark','avgPSF','SC_cameraCount_all')
save(filepath_sav_ATS, 'ATS_r0_all','ATS_fG_all','ATS_Rytov_all')

```

## A.2 *Strehl ratio code*

Listing A.2: Strehl ratio calculation code.

```

% *****
% This code computes the Strehl ratio given the camera count data
%
% Strehl Ratio
5 % PSF camera counts, open loop camera counts, camera counts, b ...
gain,
% a gain, gain map, edge_frac
%
% The code is provided from the ASALT lab authored by Denis Oesch...
, PhD and
% Darryl Sanchez, PhD
10 %
% Modified by: Kevin Vitayaudom
% Date: 2/11/2008
% *****

15 clear all;
close all;
clc;

% Declare files to investigate
20 Turb = '3';
Gmap = '4';
b = '55';
drive = 'E';
% note: Corrupt Data: T1b90g3f60, T1b55g4f80, T2b85g4f60

```

```

25  addpath([drive,':\NUGE Thesis\07 - NUGE\Thesis M-Scripts\Extra ...
      Tools'])
      load([drive,':\NUGE Thesis\07 - NUGE\Thesis M-Scripts\Non-Uniform ...
            Gain Experiment\NUGE\NUGE Data\T',Turb,'g',Gmap,'Stlb',b,'...
            _20071218.mat'])
      % addpath([drive,':\K drive\NUGE Thesis\07 - NUGE\Thesis M-Scripts...
            \Non-Uniform Gain Experiment\NUGE\NUGE Data'])
      % load(['T',Turb,'g',Gmap,'Stlb',b,'_20071218.mat'])
30  load ActMask.mat % Has a 25 x 25 ActMask
      %%

      bsize = 1; %Choose how many pixels large you want your bucket to ...
            be
35  % Ex. bsize = 0 is bucket of one pixel, bsize = 1 is a 3x3 pixel ...
            bucket

            [xc yc] = find( avgPSF(:, :) == max(max( avgPSF(:, :))) ); %Find...
            the indices of the pixel with the greatest value
            bucket_x = [ xc-bsize : xc+bsize ];
            bucket_y = [ yc-bsize : yc+bsize ]; %Create a bucket with the...
            hottest pixel at the center
40  PSFpeakPower = mean(mean( avgPSF(bucket_x, bucket_y) ));
            % Now you've found a single number (in camera counts) to ...
            quantify the PSF

            % Now you've taken open loop data with turbulence and you want to ...
            determine
            % the Strehl for all 'n' number of frames
45  for n = 1:500 %same as above, but need a 'for' loop to calculate...
            for all frames
            [xc yc] = find( SC_cameraCount_all(:, :, n, 7) == max(max( ...
            SC_cameraCount_all(:, :, n, 7))) );
            bucket_x = [ xc-bsize : xc+bsize ];
            bucket_y = [ yc-bsize : yc+bsize ];
            OLpeakPower(n) = mean(mean( SC_cameraCount_all(bucket_x, ...
            bucket_y, n, 7) )) / PSFpeakPower; %Strehl equation, Strehl...
            = [Intensity(turbulence)]/[Intensity(diffraction limited)]
50  end

            %%

            % Same thing, but now you want to look at your closed loop data ...
            with turbulence
55  % Uni Gain
            for n = 1:500
            [xc yc] = find( SC_cameraCount_all(:, :, n, 1) == max(max( ...
            SC_cameraCount_all(:, :, n, 1))) );
            bucket_x = [ xc-bsize : xc+bsize ];
            bucket_y = [ yc-bsize : yc+bsize ];

```



```

60     ClasspeakPowerUni(n) = mean(mean( SC_cameraCount_all(bucket_x...
        , bucket_y, n,1) )) / PSFpeakPower;
    end

    % Same thing, but now you want to look at your closed loop data ...
    % with turbulence
    % bGain_edgfrac 0.9
65 for n = 1:500
    [xc yc] = find( SC_cameraCount_all(:, :, n, 2) == max(max( ...
        SC_cameraCount_all(:, :, n, 2))) );
    bucket_x = [ xc-bsize : xc+bsize ];
    bucket_y = [ yc-bsize : yc+bsize ];
    ClasspeakPowerf90(n) = mean(mean( SC_cameraCount_all(bucket_x...
        , bucket_y, n, 2) )) / PSFpeakPower;
70 end

    % Same thing, but now you want to look at your closed loop data ...
    % with turbulence
    % bGain_edgfrac 0.8
    for n = 1:500
75     [xc yc] = find( SC_cameraCount_all(:, :, n, 3) == max(max( ...
        SC_cameraCount_all(:, :, n, 3))) );
    bucket_x = [ xc-bsize : xc+bsize ];
    bucket_y = [ yc-bsize : yc+bsize ];
    ClasspeakPowerf80(n) = mean(mean( SC_cameraCount_all(bucket_x...
        , bucket_y, n, 3) )) / PSFpeakPower;
    end
80

    % Same thing, but now you want to look at your closed loop data ...
    % with turbulence
    % bGain_edgfrac 0.7
    for n = 1:500
    [xc yc] = find( SC_cameraCount_all(:, :, n, 4) == max(max( ...
        SC_cameraCount_all(:, :, n, 4))) );
85     bucket_x = [ xc-bsize : xc+bsize ];
    bucket_y = [ yc-bsize : yc+bsize ];
    ClasspeakPowerf70(n) = mean(mean( SC_cameraCount_all(bucket_x...
        , bucket_y, n, 4) )) / PSFpeakPower;
    end

90 % Same thing, but now you want to look at your closed loop data ...
    % with turbulence
    % bGain_edgfrac 0.6
    for n = 1:500
    [xc yc] = find( SC_cameraCount_all(:, :, n, 5) == max(max( ...
        SC_cameraCount_all(:, :, n, 5))) );
    bucket_x = [ xc-bsize : xc+bsize ];
95     bucket_y = [ yc-bsize : yc+bsize ];
    ClasspeakPowerf60(n) = mean(mean( SC_cameraCount_all(bucket_x...
        , bucket_y, n, 5) )) / PSFpeakPower;
    end

```

```

    % Same thing, but now you want to look at your closed loop data ...
    with turbulence
100 % bGain_edgfrac 0.5
    for n = 1:500
        [xc yc] = find( SC_cameraCount_all(:,:,n,6) == max(max( ...
            SC_cameraCount_all(:,:,n,6))) );
        bucket_x = [ xc-bsize : xc+bsize ];
        bucket_y = [ yc-bsize : yc+bsize ];
105     ClasspeakPowerf50(n) = mean(mean( SC_cameraCount_all(bucket_x...
        , bucket_y, n,6) )) / PSFpeakPower;
    end

    %%

110 Cl_lp_frames = 25:500;

    avgOL = mean(OLpeakPower(Cl_lp_frames))    % Average Strehl value ...
           over 'n' frames
    stdOL = std(OLpeakPower(Cl_lp_frames))    % Standard Deviation in...
           Strehl
    avgStrhlUni = mean(ClasspeakPowerUni(Cl_lp_frames))
115 stdStrhlUni = std(ClasspeakPowerUni(Cl_lp_frames))
    avgStrhlf90 = mean(ClasspeakPowerf90(Cl_lp_frames))
    stdStrhlf90 = std(ClasspeakPowerf90(Cl_lp_frames))
    avgStrhlf80 = mean(ClasspeakPowerf80(Cl_lp_frames))
    stdStrhlf80 = std(ClasspeakPowerf80(Cl_lp_frames))
120 avgStrhlf70 = mean(ClasspeakPowerf70(Cl_lp_frames))
    stdStrhlf70 = std(ClasspeakPowerf70(Cl_lp_frames))
    avgStrhlf60 = mean(ClasspeakPowerf60(Cl_lp_frames))
    stdStrhlf60 = std(ClasspeakPowerf60(Cl_lp_frames))
    avgStrhlf50 = mean(ClasspeakPowerf50(Cl_lp_frames))
125 stdStrhlf50 = std(ClasspeakPowerf50(Cl_lp_frames))

    figure(1)
    xaxis = 1:500;
    Stl_plotX = plot(xaxis, OLpeakPower, 'g', xaxis, ClasspeakPowerUni...
        , 'r', xaxis, ClasspeakPowerf90, 'c', xaxis, ClasspeakPowerf80...
        , 'k', xaxis, ClasspeakPowerf70, 'm', xaxis, ClasspeakPowerf60, ...
        'b', xaxis, ClasspeakPowerf50, 'y');
130
    Stl_legend = legend(['Openlp Strehl = ', num2str(avgOL)], ['Clp Uni...
        Strehl = ', num2str(avgStrhlUni)], ...
        ['Clp f90 Strehl = ', num2str(avgStrhlf90)], ['Clp f80 Strehl...
        = ', num2str(avgStrhlf80)], ...
        ['Clp f70 Strehl = ', num2str(avgStrhlf70)], ['Clp f60 Strehl = ...
        ', num2str(avgStrhlf60)], ...
        ['Clp f50 Strehl = ', num2str(avgStrhlf50)]);
135 Stl_title = title(['Strehl Ratio ', ' (TurbCase ', Turb, ', b = 0.', ...
        b, ', GainMap ', Gmap, ')']);
    Stl_xlabel = xlabel('Frames (n)');
    Stl_ylabel = ylabel('Strehl Ratio');
    grid on

```

```

140 % Adjust Font and Axes Properties
    set( gca
        'FontName'      , 'Times New Roman' );
    set([Stl_title, Stl_xlabel, Stl_ylabel], ...
        'FontName'      , 'Times New Roman');
145 set([Stl_xlabel, Stl_ylabel] , ...
        'FontSize'      , 12
        );
    set( Stl_title
        'FontSize'      , 12
        'FontWeight'    , 'bold'
        );
150 set([Stl_legend, gca]
        'FontSize'      , 10
        );

    set(gca, ...
155 'Box'                , 'off'
        'TickDir'        , 'out'
        'TickLength'     , [.02 .02]
        'XMinorTick'     , 'on'
        'YMinorTick'     , 'on'
        'YGrid'          , 'on'
160 'XGrid'              , 'on'
        'LineWidth'      , 1
        );

    avgStl = [avgStrhlUni avgStrhlf90 avgStrhlf80 avgStrhlf70 ...
              avgStrhlf60 avgStrhlf50];

165 figure(2)
    phVavgap = plot(bGain_edgfrac_all(1:6),avgStl);
    % -----
    % Adjust Line Properties
    set(phVavgap, ...
170 'Color'              , [0 0 1]
        'LineWidth'       , 3
        'Marker'          , 'o'
        'MarkerSize'      , 10
        'MarkerEdgeColor' , [0 0 0]
175 'MarkerFaceColor'   , [1 0 0]
        );
    % -----
    % Add Legend and Labels
    phVavgap_title = title({'Temporally Averaged Strehl Ratio vs. ...
        bEdgefrac';['(Closed-Loop)' ,(TurbCase ',Turb, ', b = 0.',b,'...
        , GainMap ',Gmap,')' ]});
    phVavgap_xlabel = xlabel('b Edgefrac');
180 phVavgap_ylabel = ylabel('Strehl Ratio');
    % -----
    % Adjust Font and Axes Properties
    set( gca
        'FontName'      , 'Times New Roman' );
185 set([phVavgap_title, phVavgap_xlabel, phVavgap_ylabel], ...
        'FontName'      , 'Times New Roman');
    set([phVavgap_xlabel, phVavgap_ylabel] , ...

```

```

        'FontSize'      , 12          );
set( phVavgap_title    , ...
190   'FontSize'      , 12          , ...
        'FontWeight'   , 'bold'     );

set(gca, ...
195   'XDir'          , 'reverse' , ...
        'Box'         , 'off'     , ...
        'TickDir'     , 'out'    , ...
        'TickLength'  , [.02 .02] , ...
        'XMinorTick'  , 'on'     , ...
        'YMinorTick'  , 'on'     , ...
200   'YGrid'        , 'on'     , ...
        'LineWidth'   , 1        );

% -----
set(gcf, 'PaperPositionMode', 'auto');
205 print -depsc2 T3b55g1best.eps

stdStl = [stdStrh1Uni stdStrh1f90 stdStrh1f80 stdStrh1f70 ...
          stdStrh1f60 stdStrh1f50];

figure(3)
210 Stlstdavgap = plot(bGain_edgefrac_all(1:6),stdStl);
% -----
% Adjust Line Properties

set(Stlstdavgap, ...
215   'Color'         , [0 0 1]    , ...
        'LineWidth'   , 3        , ...
        'Marker'      , 'o'       , ...
        'MarkerSize'  , 10       , ...
        'MarkerEdgeColor', [0 0 0]  , ...
220   'MarkerFaceColor', [1 0 0]  );
% -----
% Add Legend and Labels
Stlstdavgap_title = title({'Temporal Std of Strehl Ratio vs. ...
        bEdgefrac';['(Closed-Loop)' ,(TurbCase ' ,Turb, ', b = 0.',b,'...
        , GainMap ',Gmap,')' ]});
Stlstdavgap_xlabel = xlabel('b Edgefrac');
225 Stlstdavgap_ylabel = ylabel('Strehl Ratio');
% -----
% Adjust Font and Axes Properties
set( gca
        'FontName'    , 'Times New Roman' );
230 set([Stlstdavgap_title, Stlstdavgap_xlabel, Stlstdavgap_ylabel...
        ], ...
        'FontName'    , 'Times New Roman');
set([Stlstdavgap_xlabel, Stlstdavgap_ylabel] , ...
        'FontSize'    , 12          );
set( Stlstdavgap_title
235   'FontSize'      , 12          , ...

```

```

        'FontWeight' , 'bold'      );

set(gca, ...
    'XDir'          , 'reverse' , ...
240 'Box'           , 'off'      , ...
    'TickDir'       , 'out'      , ...
    'TickLength'    , [.02 .02] , ...
    'XMinorTick'    , 'on'       , ...
    'YMinorTick'    , 'on'       , ...
245 'YGrid'         , 'on'       , ...
    'LineWidth'     , 1          );

```

### A.3 Error rejection function code

Listing A.3: Error rejection function calculation code.

```

% *****

% This code produces error rejection functions from the measured ...
% residual
% phase
%
5 % Error Rejection Function data necessary
% ol and cl phase, b gain, a gain, gain map, edge_frac
%
% Note: |E/D|^2 = PSD(E)/PSD(D) |
%       E/D + N/D = 1
10 % ERF = E/D, NRF = N/D
%
% Author: Kevin Vitayaudom
% Date: 1/5/2008
% *****

15 close all
clear all
clc;

% Flag for all graphs of ERF if true, Two ERFs if false
20 ALL_ERF = false;

% Declare files to investigate
Turb = '3';
Gmap = '1';
25 b = '55';
drive = 'E';
% note: Corrupt Data: T1b90g3f60, T1b55g4f80, T2b85g4f60

addpath([drive, '\NUGE Thesis\07 - NUGE\Thesis M-Scripts\Extra ...
Tools'])

```

```

30 load([drive,':\NUGE Thesis\07 - NUGE\Thesis M-Scripts\Non-Uniform ...
    Gain Experiment\NUGE\NUGE Data\T',Turb,'g',Gmap,'ERFb',b,'...
    _20071218.mat'])

% addpath([drive,':\K drive\NUGE Thesis\07 - NUGE\Thesis M-Scripts...
    \Non-Uniform Gain Experiment\NUGE\NUGE Data'])
% load(['T',Turb,'g',Gmap,'ERFb',b,'_20071218.mat'])
load ActMask.mat % Has a 25 x 25 ActMask

35 subap_x = 12;
    subap_y = 12;
    %%
    Fs = 4000; % f/fs
40 nfft = 1023;

    p=1;
    %%
    Edgefrac = ['Uni';'f90';'f80';'f70';'f60';'f50'];

45 % Computing PSD of response using cov method
    [P_Yc12Uni fc_YUni] = pcov(HRT_resPhase_all(subap_x,subap_y, :,1),p...
        ,nfft,Fs);
    [P_Yc12f90 fc_Yf90] = pcov(HRT_resPhase_all(subap_x,subap_y, :,2),p...
        ,nfft,Fs);
    [P_Yc12f80 fc_Yf80] = pcov(HRT_resPhase_all(subap_x,subap_y, :,3),p...
        ,nfft,Fs);
50 [P_Yc12f70 fc_Yf70] = pcov(HRT_resPhase_all(subap_x,subap_y, :,4),p...
        ,nfft,Fs);
    [P_Yc12f60 fc_Yf60] = pcov(HRT_resPhase_all(subap_x,subap_y, :,5),p...
        ,nfft,Fs);
    [P_Yc12f50 fc_Yf50] = pcov(HRT_resPhase_all(subap_x,subap_y, :,6),p...
        ,nfft,Fs);

% Computing PSD of disturbance using cov method
55 [P_Dc12 fc12_D] = pcov(HRT_resPhase_all(subap_x,subap_y, :,7),p,...
    nfft,Fs);

% Computing PSD of response using cov method
    [P_Yc25Uni fc_Y25Uni] = pcov(HRT_resPhase_all(subap_x,25, :,1),p,...
        nfft,Fs);
    [P_Yc25f90 fc_Y25f90] = pcov(HRT_resPhase_all(subap_x,25, :,2),p,...
        nfft,Fs);
60 [P_Yc25f80 fc_Y25f80] = pcov(HRT_resPhase_all(subap_x,25, :,3),p,...
        nfft,Fs);
    [P_Yc25f70 fc_Y25f70] = pcov(HRT_resPhase_all(subap_x,25, :,4),p,...
        nfft,Fs);
    [P_Yc25f60 fc_Y25f60] = pcov(HRT_resPhase_all(subap_x,25, :,5),p,...
        nfft,Fs);
    [P_Yc25f50 fc_Y25f50] = pcov(HRT_resPhase_all(subap_x,25, :,6),p,...
        nfft,Fs);

65 % Computing PSD of disturbance using cov method

```

```

[P_Dc25 fc25_D] = pcov(HRT_resPhase_all(subap_x,25,:,7),p,nfft,Fs)...
    ;

% where ERF is actually |ERF|^2
ERF_12_12Uni = ((P_Yc12Uni./P_Dc12));
70 ERF_12_12f90 = ((P_Yc12f90./P_Dc12));
ERF_12_12f80 = ((P_Yc12f80./P_Dc12));
ERF_12_12f70 = ((P_Yc12f70./P_Dc12));
ERF_12_12f60 = ((P_Yc12f60./P_Dc12));
ERF_12_12f50 = ((P_Yc12f50./P_Dc12));
75
ERF_12_25Uni = ((P_Yc25Uni./P_Dc25));
ERF_12_25f90 = ((P_Yc25f90./P_Dc25));
ERF_12_25f80 = ((P_Yc25f80./P_Dc25));
ERF_12_25f70 = ((P_Yc25f70./P_Dc25));
80 ERF_12_25f60 = ((P_Yc25f60./P_Dc25));
ERF_12_25f50 = ((P_Yc25f50./P_Dc25));
%%
% Determine control bandwidth
% The bandwidth code is authored by Jeffrey Barchers, PhD
85 nf = 1023;
% looking at actuator position 12 12 Uni
ind0 = max(min(find(abs(sqrt(ERF_12_12Uni))>0.5)),2);
if isempty(ind0),
    ind0 = 2;
90 end;
f2 = linspace(fc_Y25Uni(ind0-1),fc_Y25Uni(ind0),nf);

ind2 = min(find(abs(sqrt(ERF_12_12Uni))>0.5));
if isempty(ind2)
95     erfcbw12 = 0;
else
    erfcbw12 = f2(ind2);
end;
ERF_BW_UniC = erfcbw12
100 % looking at 12_25
ind0 = max(min(find(abs(sqrt(ERF_12_25Uni))>0.5)),2);
if isempty(ind0),
    ind0 = 2;
end;
105 f2 = linspace(fc_Y25Uni(ind0-1),fc_Y25Uni(ind0),nf);

ind2 = min(find(abs(sqrt(ERF_12_25Uni))>0.5));
if isempty(ind2)
    erfcbw25 = 0;
110 else
    erfcbw25 = f2(ind2);
end;
ERF_BW_UniE = erfcbw25

115 % Determine control bandwidth f90
nf = 1023;

```

```

% looking at 12 12
ind0 = max(min(find(abs(sqrt(ERF_12_12f90))>0.5)),2);
if isempty(ind0),
120     ind0 = 2;
end;
f2 = linspace(fc_Y25f90(ind0-1),fc_Y25f90(ind0),nf);

ind2 = min(find(abs(sqrt(ERF_12_12f90))>0.5));
125 if isempty(ind2)
    erfcbw12 = 0;
else
    erfcbw12 = f2(ind2);
end;
130 ERF_BW_f90C = erfcbw12
% looking at 12_25
ind0 = max(min(find(abs(sqrt(ERF_12_25f90))>0.5)),2);
if isempty(ind0),
    ind0 = 2;
135 end;
f2 = linspace(fc_Y25f90(ind0-1),fc_Y25f90(ind0),nf);

ind2 = min(find(abs(sqrt(ERF_12_25f90))>0.5));
if isempty(ind2)
140     erfcbw25 = 0;
else
    erfcbw25 = f2(ind2);
end;
ERF_BW_f90E = erfcbw25
145 %%
figure(1)

ERFUniC = loglog(fc_YUni,ERF_12_12Uni,'r');hold on
150 ERFUniE = loglog(fc_Y25Uni,ERF_12_25Uni,'g');hold on
ERFf90C = loglog(fc_Yf80,ERF_12_12f90);hold on
ERFf90E = loglog(fc_Y25f80,ERF_12_25f90);

ERF_legend = legend(...
155     ['Center, Uni, f_3_d_B = ',num2str(ERF_BW_UniC),' Hz'],['...
        Edge, Uni, f_3_d_B = ',num2str(ERF_BW_UniE),' Hz'...
        ],...
     ['Center, f90, f_3_d_B = ',num2str(ERF_BW_f90C),' Hz'],['...
        Edge, f90, f_3_d_B = ',num2str(ERF_BW_f90E),' Hz'...
        ],...
     'Location','NorthWest');

% Adjust Line Properties
160 set(ERFUniC, ...
    'Color'          , [0 1 1]          , ...
    'LineWidth'     , 3                  );
set(ERFUniE, ...
    'Color'          , [1 0 1]          , ...

```



```

165     'LineWidth'      , 3          );
    set(ERFf90C, ...
        'Color'        , [0 0 1]    , ...
        'LineWidth'    , 3          );
170     set(ERFf90E, ...
        'Color'        , [1 0 0]    , ...
        'LineWidth'    , 3          );

    ERF_title = title(['Error Rejection Function', ' (TurbCase ', Turb, ...
        ', b = ', b, ', GainMap ', Gmap, ')']);
    ERF_xlabel = xlabel('Frequency (Hz)');
175 ERF_ylabel = ylabel('|Transfer Function|^2');

    % Adjust Font and Axes Properties
    set( gca
        'FontName'     , 'Times New Roman' );
180 set([ERF_title, ERF_xlabel, ERF_ylabel], ...
        'FontName'     , 'Times New Roman');
    set([ERF_xlabel, ERF_ylabel] , ...
        'FontSize'     , 12          );
185 set( ERF_title
        'FontSize'     , 12          , ...
        'FontWeight'   , 'bold'     );
    set([ERF_legend, gca]
        'FontSize'     , 10          );

190 set(gca, ...
        'Box'          , 'off'       , ...
        'TickDir'      , 'out'       , ...
        'TickLength'   , [.02 .02]   , ...
        'XMinorTick'   , 'on'        , ...
195 'YMinorTick'     , 'on'        , ...
        'YGrid'        , 'on'        , ...
        'XGrid'        , 'on'        , ...
        'LineWidth'    , 1          );

200 axis tight
    % -----
    set(gcf, 'PaperPositionMode', 'auto');
    print -depsc2 t3g1erf.eps

```

#### A.4 Lyapunov stability code

Listing A.4: Lyapunov stability code.

```

% *****
% This code produces the error propagator which is used to ...
% determine
% Lyapunov stability
%

```

```

5 % A0 Tools subapdlg is used to produce the reconstructor and ...
    geometry
% matrices
%
% Author: Kevin Vitayaudom
% Date: 1/5/2008
10 % *****

% using subapdlg to get M = H; and A = Gam;
% and load in M and A
load Lyapunov.mat;
15
% Considering a 25 x 25 design with no slaving
MA = M*A;
MAsize = size(MA);
I = eye(MAsize(2));
20 % Number of controlled actuators in the pupil
Na = MAsize(2);
% leaky integrator gain ~1
a0 = 0.99;
% loop gain or 'b' gain
25 k = 0.01:0.01:2.5;
ksize = size(k);
gn = zeros(1,ksize(2));
for idx = 1:ksize(2)
    F = a0*I - k(idx)*M*A;
30 % error propagation equation (or noise gain)
    gn(idx) = (k(idx)^2/Na)*trace(inv(I-F'*F)*M*M');
end
figure(1)
semilogy(k,gn)
35 xlabel('Loop Gain,k')
ylabel('Error Propagation, gn')
title('Using Noise Gain to investigate Stability')
axis([0 2 1e-4 1e4])
save('saveLyap2.mat','k','gn','M','A')

```

## A.5 NUGE DM Filter

Listing A.5: NUGE DM Filter component code.

```

% *****

% This code is used to setup a MATLAB ASALT Component - NUGE DM ...
% Filter
%
% MATLAB ASALT Component -- DM Controller with Non-Uniform Gain
5 % Produces DM Commands from last dm command and error. Uses ...
% a non-uniform gain for the
% 'gain' coefficient.

```

```

%
%   ala dynamo and dnip
%
10 % Author: Kevin Vitayaudom
% Date: 12/15/2007
% *****

function [dm_cmd]=DM_Filter_NUGE(phaseErr,phaseScale,DM_Limit,...
    dm_cmd,aGain,bGain,bGain_edgfrac,bMapType,frameCounter,...
    DM_inhibit)
% This function calculates DM commands ala Dynam0 and Dnip
15 %
% Must be 25x25 input, does not take into regard delay
%
% Inputs:
%     phaseErr      = phase calculated from WFS data
20 %     flag_DM_inhibit = Flag.  =1 don't calculate DM commands. ...
%     =0 calculate DM commands
%
% Configuration Items:
%     aGain          = A gain in  $y(t) = ay(t-1) + bx(t)$ 
%     bGain          = B gain in  $y(t) = ay(t-1) + bx(t)$ 
25 %     bGain_edgfrac is the fraction of the bGain on the edge ...
%     actuators
%     frameCounter   = frame counter
%
% Outputs:
%     dm_cmd         = DM commands
30 %
% Assumptions:
%     dm_cmd         is initialized in the AMC file, i.e. dm_cmd...
%     = int16(zeros(27));k=0;
%     frameCounter  is initialized in the AMC file, i.e. ...
%     frameCounter=0;
35 % ActMask.mat is loaded to get HRT_Msk25act_otr and ...
%     HRT_Msk25act_inr (25 x 25 double)

% initialize
load ActMask.mat;
load Edge_bGain.mat
40
phaseErr = double(phaseErr);
dm_cmd = dm_cmd'; % AMC file conversion transposes after each ...
    frame (unless you do sorread)
nsub    = size(phaseErr,1); %%% determine resolution from ...
    phaseErr frame
SLAVELIMIT = -32768;
45
% Apply Gain Map
if bMapType == 1
    GainMap = Edge_Bmap1.*bGain_edgfrac + Bmap1_inv;

```

```

50 elseif bMapType == 2
    GainMap = Edge_Bmap2.*bGain_edgefrac + Bmap2_inv;

    elseif bMapType == 3
        GainMap = Gauss_Bmap(1,13,bGain_edgefrac);
55 elseif bMapType == 4
        bGain_partial = (1 - bGain_edgefrac)/2 + bGain_edgefrac;
        GainMap = Edge_Bmap1.*bGain_edgefrac + Edge_Bmap4.*...
            bGain_partial + Bmap14_inv;
    else
        GainMap = ones(25);
60 end

% Declare DM limits
DM_Min = DM_Limit(1);
DM_Max = DM_Limit(2);
65

% exit if DM operation is inhibited
% if flag_DM_inhibit = 1, no dm cmds , if flag_DM_inhibit = 0 dm ...
    cmds
if (DM_inhibit)
    dm_cmd = int16(zeros(nsub)); % load zeros
70 return; % return
end

%%% slave the actuators, done in DM Controller

75 if (frameCounter > 1)
    % slaves designated actuators
    slaveIndex = find(phaseErr<=SLAVELIMIT);
    %slaveIndex = find(int16(HRT_Msk25act_otr).*phaseErr<=...
        SLAVELIMIT);

80 % command law
    dm_cmd = (aGain.*dm_cmd) + int16(GainMap.*bGain.*phaseErr.*...
        phaseScale);

    % apply stroke limits in inner and outer sections (just a check...
        )
    dm_cmd_inr = int16(HRT_Msk25act_inr).*min(DM_Max,max(DM_Min,...
        dm_cmd));
85 dm_cmd_otr = int16(HRT_Msk25act_otr).*min(DM_Max,max(SLAVELIMIT...
        ,dm_cmd));

    % recombine
    dm_cmd = dm_cmd_inr + dm_cmd_otr;

90 dm_cmd(slaveIndex) = SLAVELIMIT;
    else
        dm_cmd = int16(zeros(nsub));
    end
end

```

```

    % ensure output is int16, for the DM Controller block
95   dm_cmd = int16(dm_cmd);
    return

```

## A.6 NUGE DM Filter AMC code

Listing A.6: NUGE DM Filter AMC code.

```

% *****
% This code is used to setup a MATLAB ASALT Component
%
% AMC code that defines the processing block in the layout for the...
    NUGE DM
5 % Filter.
%
%   ala dynamo and dnip
%
% Author: Kevin Vitayaudom
10 % Date: 12/15/2007
% *****

%%% Startup definition
Startup: pack; frameCounter=0; frameCounter=int16(frameCounter); ...
    dm_cmd=int16(zeros(25));
15

%%% Callback definition
Callback: frameCounter = frameCounter+1; [dm_cmd] = ...
    DM_Filter_NUGEnew(phaseErr,phaseScale,DM_Limit,dm_cmd,aGain,...
    bGain,bGain_edgfrac,bMapType,frameCounter,DM_inhibit);

%%% Component definition
20 Component
    Name: DM Filter NUGE new
    ID: 10097
    Version: 65536
    Description: Calculates DM Commands using non-uniform gain
25    Program: DMFilterNUGE_Run.m
    Author: Kevin Vitayaudom
End Component

%%% Input definitions
30 Input
    Name:          phaseErr
    Description:   Reconstructed Phase up to 64 by 64
    Type:          real64
    Width:         -1
35    Height:       -1
    Frames:        1
End Input

```

```

Input
40   Name:          DM_inhibit
      Description:  Flag. = 1 don't calculate DM commands. ...
                = 0 calculate DM commands
      Type:         int32
      Width:        -1
      Height:       -1
45   Frames:       1
      End Input

      % Configuration definitions

50   Config
      Name:         phaseScale
      Description:  Scale factor used to convert input units ...
                to output units
      Type:         real64
      Min:          -1.8e308
55   Max:          1.8e308
      Width:        1
      Height:       1
      Frames:       1
      Default:      1
60   End Config

      Config
      Name:         aGain
      Description:  = A parameter in  $y(t) = A y(t-1) + B x(t)$ 
65   type:         real64
      Min:          0
      Max:          1
      Width:        1
      Height:       1
70   Frames:       1
      Default:      0.99
      End Config

      Config
75   Name:         bGain
      Description:  = B parameter in  $y(t) = A y(t-1) + B x(t)$ 
      type:         real64
      Min:          -1
      Max:          1
80   Width:        1
      Height:       1
      Frames:       1
      Default:      0.4
      End Config
85   Config
      Name:         bMapType

```

```

Description:      = 1 Edge Map, = 2 Wider Edge Map, = 3 ...
                  Gaussian Map
type:             real64
90  Min:          0
    Max:          4
    Width:        1
    Height:       1
    Frames:       1
95  Default:     0
    End Config

Config
Name:             bGain_edgefrac
100 Description:   Fraction of bGain on edges
type:             real64
    Min:          0
    Max:          2
105 Width:        1
    Height:       1
    Frames:       1
    Default:     1
    End Config

110 Config
Name:             DM_Limit
Description:      Minimum and maximum stroke limits for the ...
                  DM in DM units.
Type:             int16
    Min:          -32800
115 Max:          32800
    Width:        2
    Height:       1
    Frames:       1
    Default:     0
120 End Config

% Output definitions
Output
Name:             dm_cmd
125 Description:   DM commands
Type:             int16
    Width:        25
    Height:       25
    Frames:       1
130 VarWidth:     1
    VarHeight:    1
    VarFrames:    0
    End Output

```

## Bibliography

1. Andrews, Larry C. and Ronald L. Phillips. *Laser Beam Propagation through Random Media*. SPIE Press, 2nd edition, 2005.
2. Barchers, Jeffrey D. *Higher order control laws for adaptive optical systems*. In-House AR-09, Science Applications International Corporation, Longmont, CO, October 2002.
3. Beckers, J. M. “Removing perspective elongation effects in laser guide stars and their use in the ESO Very Large Telescope”. *Progress in telescope and Instrumentation Technologies*, 1992.
4. Beckner, Charles, Patrick Kelly, and Keith Wojciechowski Troy Rhoadarmer. “JTO Multi-Conjugate Adaptive Optics (MCAO) Project”, Decemeber 2007. Draft.
5. Paris, Neil D. *LQG/LTR Tilt and Tip Control for the Starfire Optical Range 3.5-meter Telescopes’s Adaptive Optics System*. Master’s thesis, Air Force Institute of Technology, 2006.
6. Pennington, Timothy L., David W. Swindle, Michael D. Olikier, Brent L. Ellerbroek, and James M. Spinhirne. “Performance measurements of Generation III wavefront sensors at the Starfire Optical Range”. volume 2534, 327–337. SPIE, Kirtland Air Force Base, NM 87117, 1995.
7. Plett, M. L., P. R. Barbier, D. W. Rush, P. Polak-Dingels, and B. M. Levine. “Measurement error for a Shack-Hartmann wavefront sensor in strong scintillation conditions”. volume 3433, 211–220. SPIE, University of Maryland, MD 20740, 1998.
8. Rhoadarmer, Troy. “Wave Front Sensors and Basic Reconstruction”, March 2002. Briefing at AFRL.
9. Rhoadarmer, Troy, Tony Vincent, Denis Oesch, and Darryl Sanchez. “Effects of Phase Shifting Error Upon the Self-Referencing Interferometer”, June 2007. Figure from briefing at SPIE Optics and Photonics.
10. Roggemann, Michael C. and Byron M. Welsh. *Imaging through Turbulence*. CRC Press, 1996.
11. Schmidt, Jason D. *Free-Space Optical Communications Performance Enhancement by Use of a Single Adaptive Optics Correcting Element*. Ph.D. thesis, University of Dayton, 2006.
12. Spinhirne, J.M., J.G. Allen, G.A. Ameer, J.M. Brown II, J.C. Christou, T.S. Duncan, R.J. Eager, M.A. Ealey, B.L. Ellerbroek, R.Q. Fugate, G.W. Jones, R.M. Kuhns, D.J. Lee, W.H. Lowrey, M.D. Olikier, R.E. Ruane, D.W. Swindle,



- J.K. Voas, W.J. Wild, K.B. Wilson, and J.L. Wynia. “The Starfire Optical Range 3.5m Telescope Adaptive Optical System”. volume 3353, 22–33. SPIE, 1998.
13. Tyson, Robert K. *Principles of Adaptive Optics*. Academic Press, Inc., Harcourt Brace Jovanovich, Publishers, 1991. ISBN 0-12-705900-8.
  14. Tyson, Robert K. and Benjamin W. Frazier. *Field Guide to Adaptive Optics*, volume FG03. SPIE, 2004.
  15. Viard, Elise, Françoise Delplancke, Norbert Hubin, and Nancy Ageorges. “LGS Na-spot elongation and Rayleigh scattering effects on Shack-Hartmann wavefront sensor performances”. volume 3762, 8–19. SPIE, European Southern Observatory, Munchen, Germany, 1999.
  16. Wild, Walter J. “Innovative Wavefront Estimators for Zonal Adaptive Optics Systems”. volume 3126, 278–287. Department of Astronomy and Astrophysics, University of Chicago, SPIE, 5640 S. Ellis Ave, Chicago, Illinois 60637, 1997.
  17. Wild, Walter J. “Innovative Wavefront Estimators for Zonal Adaptive Optics Systems. II”. volume 3353, 1164–1173. Department of Astronomy and Astrophysics, University of Chicago, SPIE, 5640 S. Ellis Ave, Chicago, Illinois 60637, March 1998.
  18. Wild, Walter J. “Lyapunov stability criteria for zonal adaptive-optics systems”. *Optics Letters*, 23(8):570–572, April 1998.
  19. Wild, Walter J., Edward J. Kibblewhite, Fang Shi, Barbara Carter, Gary Kelderhouse, and Rodolphe Vuilleumier. “Field tests of the Wavefront Control Experiment”. volume 2201, 1121–1134. Department of Astronomy and Astrophysics, University of Chicago, SPIE, 5640 S. Ellis Ave, Chicago, Illinois 60637, 1994.
  20. Wild, Walter J., Edward J. Kibblewhite, Rodolphe Vuilleumier, Vijuna Scor, Fang Shi, and Nestor Farmiga. “Investigation of Wavefront Estimators Using the Wavefront Control Experiment at Yerkes Observatory”. volume 2534, 194–205. Department of Astronomy and Astrophysics, University of Chicago, SPIE, 5640 S. Ellis Ave, Chicago, Illinois 60637, May 1995.

## *Vita*

Lieutenant Kevin P. Vitayaudom earned a Bachelor of Science degree in Electrical Engineering from the University of Portland, and was commissioned into the United States Air Force on May 15, 2006 through ROTC. His first assignment was to the Air Force Institute of Technology, Wright Patterson AFB, OH to earn a Master of Science degree in Electrical Engineering. Lt Vitayaudom's follow-on assignment is to the Starfire Optical Range at Kirtland AFB, NM.

Permanent address: 2950 Hobson Way  
Air Force Institute of Technology  
Wright-Patterson AFB, OH 45433

# REPORT DOCUMENTATION PAGE

*Form Approved*  
OMB No. 0704-0188

The public reporting burden for this collection of information is estimated to average 1 hour per response, including the time for reviewing instructions, searching existing data sources, gathering and maintaining the data needed, and completing and reviewing the collection of information. Send comments regarding this burden estimate or any other aspect of this collection of information, including suggestions for reducing this burden to Department of Defense, Washington Headquarters Services, Directorate for Information Operations and Reports (0704-0188), 1215 Jefferson Davis Highway, Suite 1204, Arlington, VA 22202-4302. Respondents should be aware that notwithstanding any other provision of law, no person shall be subject to any penalty for failing to comply with a collection of information if it does not display a currently valid OMB control number. **PLEASE DO NOT RETURN YOUR FORM TO THE ABOVE ADDRESS.**

<b>1. REPORT DATE</b> (DD-MM-YYYY) 27-03-2008		<b>2. REPORT TYPE</b> Master's Thesis		<b>3. DATES COVERED</b> (From — To) Aug 2006 — Mar 2008	
<b>4. TITLE AND SUBTITLE</b>  Analysis of Non-Uniform Gain for Control of a Deformable Mirror in an Adaptive-Optics System				<b>5a. CONTRACT NUMBER</b>	
				<b>5b. GRANT NUMBER</b>	
				<b>5c. PROGRAM ELEMENT NUMBER</b>	
<b>6. AUTHOR(S)</b>  Kevin P. Vitayaudom, 2d Lt, USAF				<b>5d. PROJECT NUMBER</b>  ENG 08-295	
				<b>5e. TASK NUMBER</b>	
				<b>5f. WORK UNIT NUMBER</b>	
<b>7. PERFORMING ORGANIZATION NAME(S) AND ADDRESS(ES)</b> Air Force Institute of Technology Graduate School of Engineering and Management (AFIT/EN) 2950 Hobson Way WPAFB OH 45433-7765				<b>8. PERFORMING ORGANIZATION REPORT NUMBER</b>  AFIT/GE/ENG/08-35	
<b>9. SPONSORING / MONITORING AGENCY NAME(S) AND ADDRESS(ES)</b> Darryl J. Sanchez, PhD AFRL/RDS (AFMC) 3550 Aberdeen Ave SE Kirtland Air Force Base, NM 87117-5776 (505) 846-7209 (DSN: 246-7209), email: darryl.sanchez@kirtland.af.mil				<b>10. SPONSOR/MONITOR'S ACRONYM(S)</b>  <b>11. SPONSOR/MONITOR'S REPORT NUMBER(S)</b>	
<b>12. DISTRIBUTION / AVAILABILITY STATEMENT</b>  Approved for public release; distribution is unlimited.					
<b>13. SUPPLEMENTARY NOTES</b>					
<b>14. ABSTRACT</b> The objective of this research was to develop and experimentally verify the use of spatially varying gain maps on the servo-loop controller of a deformable mirror for improvements in the performance of an adaptive optics system and the mitigation of instabilities that can occur over edge actuators of a deformable mirror. The edge subapertures of a Shack-Hartmann wavefront sensor have lower signal-to-noise ratios and are more susceptible to measurement errors than fully illuminated center subapertures. Spatially varying gain maps were then developed to compensate for edge effects by having lower filter gains <i>b</i> on the edge actuators. This lowered the bandwidth over the edge actuators which are the most susceptible to the edge effects. A gain map of lower filter gains <i>b</i> over just the outer actuators was experimentally shown to increase the overall Strehl ratio of the AO system in all of the tested turbulence conditions. Experiments were also conducted in regimes where instabilities formed over the edge actuators of the DM. Gaussian gain maps significantly reduce the overall residual phase variance over the edge actuators reducing the formation of the instabilities.					
<b>15. SUBJECT TERMS</b>  adaptive optics, servo-loop controller, spatially varying gain, deformable mirror					
<b>16. SECURITY CLASSIFICATION OF:</b>			<b>17. LIMITATION OF ABSTRACT</b>	<b>18. NUMBER OF PAGES</b>	<b>19a. NAME OF RESPONSIBLE PERSON</b>
<b>a. REPORT</b>	<b>b. ABSTRACT</b>	<b>c. THIS PAGE</b>			<b>19b. TELEPHONE NUMBER</b> (include area code)
U	U	U	UU	131	Capt Jason D. Schmidt, PhD (937) 255-3636, x7224 jschmidt@afit.edu